

UNCLASSIFIED

AD 426729

DEFENSE DOCUMENTATION CENTER

FOR

SCIENTIFIC AND TECHNICAL INFORMATION

CAMERON STATION, ALEXANDRIA, VIRGINIA



UNCLASSIFIED

NOTICE: When government or other drawings, specifications or other data are used for any purpose other than in connection with a definitely related government procurement operation, the U. S. Government thereby incurs no responsibility, nor any obligation whatsoever; and the fact that the Government may have formulated, furnished, or in any way supplied the said drawings, specifications, or other data is not to be regarded by implication or otherwise as in any manner licensing the holder or any other person or corporation, or conveying any rights or permission to manufacture, use or sell any patented invention that may in any way be related thereto.

# DISCLAIMER NOTICE

THIS DOCUMENT IS THE BEST  
QUALITY AVAILABLE.

COPY FURNISHED CONTAINED  
A SIGNIFICANT NUMBER OF  
PAGES WHICH DO NOT  
REPRODUCE LEGIBLY.

64-6

RADC-TDR-63-492

November 1963

426729

CATN 63-107-520C  
AS FILED

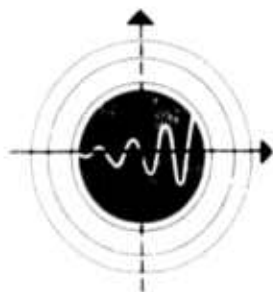
# RESEARCH AND DEVELOPMENT ON L-BAND CROSSED-FIELD AMPLIFIER CHAIN

by  
M. Mongot  
H. L. McDowell

Semi-annual Report  
September 1963 to February 1963

Contract Nr. AF 30(602)-2533  
ARPA Order No. 136.61

Prepared  
for  
Rome Air Development Center  
Research and Technology Division  
Air Force Systems Command  
United States Air Force  
Griffiss Air Force Base  
New York



*S•F•D laboratories, inc.*  
*Union, New Jersey*

426729

## NOTICES

When Government drawings, specifications, or other data are used for any purpose other than in connection with a definitely related Government procurement operation, the United States Government thereby incurs no responsibility nor any obligation whatsoever and the fact that the Government may have formulated, furnished, or in any way supplied the said drawings, specifications or other data is not to be regarded by implication or otherwise as in any manner licensing the holder or any other person or corporation, or conveying any rights or permission to manufacture, use or sell any patented invention that may in any way be related thereto.

Qualified requestors may obtain copies of this report from Defense Documentation Center (DDC), (Formerly ASTIA), Cameron Station, Alexandria, Virginia 22314.

This report has been released to the Office of Technical Services, U. S. Department of Commerce, Washington 25, D. C., for sale to the general public.

RADC-TDR-63-492

November 1963

RESEARCH AND DEVELOPMENT  
ON  
L-BAND CROSSED-FIELD AMPLIFIER CHAIN

by

M. Mangot  
H. L. McDowell

Semi-annual Report  
September 1963 to February 1963

Contract Nr. AF 30(602)-2533  
Project Number 4983  
Task Number 55287

ARPA Order No. 136,61

Prepared  
for

Rome Air Development Center  
Research and Technology Division  
Air Force Systems Command  
United States Air Force  
Griffiss Air Force Base  
New York

## ABSTRACT

New versions of both driver and power tubes were designed and construction of these tubes was started. Studies were made of different magnetic circuit designs to determine how tubes could best be mounted in a phased array. It was concluded that a fixed array of permanent magnets with removable tubes made largely of non-magnetic material is preferable to combined tube and permanent magnet packages. Initial tests were made on the incorporation of a non-reciprocal ferrite attenuator on the slow wave circuit. While these tests show promise, they also indicate that a number of difficult problems must be solved to obtain a satisfactory non-reciprocal attenuator. Procurement of phase measuring equipment and life test equipment was started. A study of the relative costs of one antenna element per tube versus several elements per tube was conducted with the tentative conclusion that several elements per tube would be cheaper if the necessary high power phase shifters could be made available at reasonable cost.

## PUBLICATION REVIEW

This report has been reviewed and is approved. For further technical information on this project, contact Mr. John N. Schneider, RALTE, Ext. 22224.

Approved:

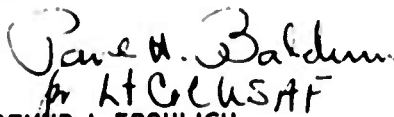


JOHN N. SCHNEIDER

Project Engineer

Directorate of Aerospace Surveillance & Control

Approved:



ARTHUR J. FROHLICH

Chief, Techniques Laboratory

Directorate of Aerospace Surveillance & Control

## TABLE OF CONTENTS

	<u>Page</u>
1.0 Introduction	1
2.0 Evaluation of Existing Tube Designs	2
2.1 The Internal Magnetic Circuit of the SFD-209	2
2.2 Sources of Feedback in the SFD-209	10
2.3 Phase Measurements and Phase Measuring Equipment	24
2.4 Control Electrode Characteristics	33
2.5 Long Pulse Tests	45
2.6 Water Cooled SFD-209	45
2.7 Miscellaneous Experiments on the SFD-209	46
2.8 Experiments on the SFD-216	50
3.0 Study of Magnetic Design and Problems Related to Mounting Tubes in an Array	54
3.1 The Requirements and Different Approaches to Satisfying them	54
3.2 The Magnetically Shielded Package	56
3.3 Magnet inside the Cathode	63
3.4 Magnets external to the Tube and Packaged with the Tube	66
3.5 Magnets in a Fixed Array	67
3.6 Magnets for an Isolated Tube	74
4.0 Revised Tube Designs	76
5.0 Plans for Life Tests	80
6.0 Studies on the Application of Non-reciprocal Loss to the SFD-209 Circuit through the Use of Ferrites	83
6.1 Introduction and General Summary	83
6.1.1 Why non-reciprocal loss is desirable	83
6.1.2 Some of the problems to be considered	83
6.1.3 Short summary of progress	84
6.1.4 Present status	84
6.2 Interaction of RF Fields of the SFD-209 Structure with a Ferrite Ring	84
6.2.1 Qualitative description of the magnetic field pattern	84



6.2.2	Ferrite interaction with the RF fields	89
6.2.3	Quantitative verification	90
6.3	Experimental Results and Their Comparison with Theory	93
6.3.1	Kittel's Equation	93
6.3.2	Discussion of the demagnetizing factors and their applicability in this case	95
6.3.3	Correlation between Experimental results and Kittel's Equation	98
6.3.4	Discussion of experimental results	99
6.3.5	Low field loss	103
6.3.6	Linewidth requirements for 10% bandwidth	108
6.3.7	Effect of temperature on linewidth	112
6.3.8	Experimental results	112
6.4	Determination of the Geometry and Location of New Ferrite Rings of various Compositions from the Results of Experiments conducted with the AN50MW Ferrite Rings	117
6.4.1	Effect of increasing the thickness of the ferrite by attenuation	121
6.5	Non-linear Effects - First and Second Order	121
6.5.1	Calculation of the magnitude of the h <sub>RF</sub> fields present in our tube in the region in which we wish to position the ferrite	124
6.5.2	Threshold of second order effect and ferrite behavior beyond threshold	126
6.5.3	Effect of substitutions on the value of h <sub>(critical)</sub> in Yttrium Garnets	126
6.5.4	Critical field for nickel ferrite aluminate	128
6.5.5	Critical field for Yttrium-Gadolinium garnet	128
6.6	Determining the Proper Ferrite for our Application	128
6.7	The Linear Version of the SFD-209 Circuit	129
6.7.1	Reasons for Linear Circuit	131
6.7.2	Provisions for High Power Test	132
7.0	Study of the Economics Involved in Various Array Configurations	133
8.0	Program for Next Interval	143

## LIST OF ILLUSTRATIONS

Figure		Page
1	Sketch of the Internal Magnetic Parts of the SFD-209	3
2	Distribution of Magnetic Field Along the Axis in the Presence of a Flux Guide Shaped as shown in the Top Figure	4
3	Distribution of Magnetic Field Along the Axis with Magnetic End Hats but without Flux Guide	5
4	Distribution of Magnetic Field Along the Axis in the Absence of a Flux Guide and with Non-Magnetic End Hats	6
5	V-I Curves of the same Driver Tube with Flux Guide and as Later Rebuilt with a Uniform Magnetic Field	8
6	A Somewhat Exaggerated Sketch of the Fanning Out of Magnetic Equipotentials in the Interaction Space in the Presence of a Flux Guide	9
7	Schematic Showing the Three Major Sources of Feedback	11
8	Transmission Loss and Return Loss for the SFD-209 Driver as Functions of Frequency	13
9	Power Output as a Function of Frequency for a Recent SFD-209 Tube	14
10	Power Output as a Function of Frequency for a Recent SFD-209 Tube	15
11	The $\omega$ - $\beta$ Curve for the SFD-209 Tube which gave the Performance shown in Figures 9 and 10 and Figures 12 through 15	18
12	Performance Chart for the SFD-209 Driver Tube with an Input Power of 1 kw Peak at 1160 Mc	19
13	Performance Chart for the SFD-209 Driver Tube with an Input Power of 5 kw Peak at 1160 Mc	20
14	Performance Chart for 1 kw Input for a Frequency for which the Feedback is Degenerative	21

Figure		Page
15	Performance Chart for 5 kw Input at a Frequency for which the Feedback is Degenerative	22
16	Phase Pushing in the SFD-209 Measurements	25
17	Simplified Block Diagram of the Test Set used to Measure Phase Pushing	26
18	The Phase Measuring System proposed by Merrimac	28
19	Block Diagram of Phase Bridge set up requiring a Simultaneous Amplitude and Phase Balance. A Hybrid Junction is used as the Phase Comparator	29
20	Block Diagram of Phase Measuring System in which the Output of the Phase Detector is Insensitive to Amplitude Variations in the Input Arms	30
21	Block Diagram of Phase Measuring Equipment to be used in Testing the L-band Tubes. The Wiltron Phase Measuring System, consisting essentially of a Double Probe Slotted Line and Differential Amplifier and Detector will be used. It will be necessary to employ extreme care in setting up the system to minimize the errors caused by mismatch effects. Special directional Couplers and Attenuators will be required	32
22	Block Diagram of the Pulsing Scheme used with a Control Electrode on the Anode Side of the Drift Space	34
23	Photographs showing Oscillograms of the RF Input Pulse, Control Voltage Pulse and RF Output Pulse for the SFD-209	35
24	Photographs showing Oscillograms of the Control Electrode Current Pulse	36
25	A Bootstrap Pulsing Circuit for the Control Electrode Modulator	38
26	A Thyatron Pulsing Circuit for the Control Electrode which does not require an Output Transformer	39
27	The V-I Characteristics of the Control Electrode	40
28	Schematic Drawing showing the Location of the Anode Side Control Electrode	43

Figure		Page
29	The Control Electrode Current Characteristic of the Anode Side Control Electrode. If a Resistance of greater than 3500 Ohms is connected between the Control Electrode and Ground the Control Segment will bias itself toward Cathode Potential	44
30	$\omega$ - $\beta$ Curves of Tapered SFD-209 Circuit at the Extreme Ends	48
31	Sketch showing a Form of Circuit Tapering which may be preferable to that of Figure 30	49
32	A Frequency Response Curve measured on the SFD-216	51
33	The $\omega$ - $\beta$ Curve for the SFD-216	52
34	Transmission and Return Loss as a Function of Frequency for the SFD-216	53
35	Tentative Magnetic Circuit Design for Shielded Package	57
36	Electrolytic Tank Plot of a Tentative Magnetic Circuit Design of the Required Tube	58
37	Electrolytic Tank Plot of a Trial Solution for the Magnetic Circuit Design of the Required Tube	59
38	Permeance Calculation for Shielded Package Design	62
39	Sketch showing Location of a Magnet inside the Cathode which was Considered	64
40	Magnetic Field Intensity near the side of a Cylindrical Alnico VIII Magnet. Similar Variations of Field Intensity were obtained with an Indox Magnet	65
41	Sketch of an Array of Fixed Permanent Magnets into which Tubes may be Inserted	68
42	Distribution of Magnetic Field from Center to Corner of Pole Faces for a Magnet between Large Soft Iron Pole Faces	71
43	Ratio $H/H_m$ from Figure 42 as a Function of the Ratio $s/h$	72
44	Revised Version of the SFD-209	78
45	Block Diagram of Life Test Set Up. Four Identical Positions will be Provided	81

Figure		Page
46	Field Patterns Associated with the SFD-209 Structure	85
47	Associated with the Description of Field Patterns	85
48	Relating to the Rotation of the $h_{RF}$ Magnetic Fields in the Vicinity of the SFD-209 Structure	87
49	Relating to the State of Polarization of the Magnetic Fields in the Region considered in Figure 48	87
50	$\omega$ - $\beta$ Characteristic of a Slow Wave Structure	87
51	Plot of Attenuation versus Radial Displacement from Outer Edge of Circuit	92
52	Measurement of Transmission Loss of the Circuit with Ferrite Element Present	94
53	Relationship between Ferrite Geometry and Extend of $h_{RF}$ Field Loops	96
54	Description of Demagnetizing Factors in a Slab	96
55	Relating to the Ferrite Geometry under Consideration	96
56	Transmission Loss versus Magnetic Field Applied to Circuit	100
57	Transmission Loss versus Magnetic Field Applied to Circuit with Lateral Displacement as a Parameter	101
58	Determination of Maximum Allowable $4\pi M_s$ as a function of Transverse Demagnetizing Factor	105
59	Relating to the Description of Low Field Loss in Relation to Resonance Loss	107
60	Measurement of Transmission Loss of Brass Structure Loaded on One Side with Ferrite Ring Section	109
61	Measurement of Transmission Loss of Brass Structure Loaded on One Side with Ferrite Ring Section, $a = 1$ mm	110
62	Plot of Attenuation by the Ferrite versus Radial Excursion from the Surface of the Circuit in Presence of Can	114
63	Measurement of Transmission Loss of Brass Structure Loaded on One Side with a Ferrite Ring Section	115

Figure		Page
64	Measurement of Transmission Loss of Brass Structure Loaded on One Side with a Ferrite Ring Section, can in place	116
65	Graphical Method for Determining the Location of the Ferrite Ring with respect to the Surface of the Circuit	119
66	Determination of ID of Ferrite Rings with $4\pi M_s / \Delta H$ as a Parameter	120
67	Description of Second Order Non-Linear Effect: Normalized Susceptibility versus Inverse of $h_{RF}$ Field	127
68	Block Diagram of an Array Arrangement in which Several Antennas are fed from each Power Amplifier	134
69	Tube Cost per Antenna Element as a Function of Number of Tubes per Antenna Element for an L-band Array Radiating 100 kw Peak per tube	138
70	Relative Tube Cost per Antenna Element as a Function of Number of Tubes per Element for an L-band Array Radiating 1 Mw Peak per Element	139
71	Relative Increase in Component Cost as a Result of Power Division and Phase Shifting in the High Power Line as a Function of the number of Antenna Elements per Tube	140
72	Relative Cost as a Function of Frequency	142

Table		
I	Properties of Ferrite Materials which seem Best Suited for our Requirements	130
II	Estimated Tube Cost for Various L Band Array Configurations	136

## 1.0 INTRODUCTION

During the period covered by this report, effort has been expended along a number of different lines in preparation for the next stage of the program which is the construction and evaluation of groups of identical tubes. The areas of effort have been:

- (1) Evaluation of present tube designs
- (2) Redesign of the tubes based on this evaluation and for the purpose of incorporating liquid cooling through the circuit bars to raise the average power level
- (3) Study and evaluation of magnetics problems for tubes mounted in an array
- (4) Study of phase measuring equipment available and procurement of this equipment
- (5) Planning of a life test set up and ordering of the necessary equipment
- (6) Studies of the problems involved in the incorporation of a ferrite attenuator in the tubes
- (7) Economic study as requested by ARPA of the relative costs of one versus several tubes per antenna element.

These areas of effort will be covered individually in the following sections.

## 2.0 EVALUATION OF EXISTING TUBE DESIGNS

### 2.1 The Internal Magnetic Circuit of the SFD-209

At the end of August 1962 there were two versions of the SFD-209. One of these had magnetic end hats and a flux guide behind the cathode surface. This design permitted us to obtain a magnetic field in the interaction space higher than that in the permanent magnet material located just outside the vacuum envelope. Figure 1 shows a sketch of the magnetic parts of this design and Figure 2 shows the measured magnetic field strength along the cathode, anode and wall surfaces. The axial variation of magnetic field is small although there is a considerable radial field variation. From the magnetics standpoint, this arrangement made the most efficient use of the permanent magnet material. The function of the soft iron flux guide in this design was to provide the axial field uniformity. Without the flux guide, the magnetic field strength at the center of the gap would have been much less than at the ends. This is shown in Figure 3 which shows the axial flux density variation with the magnetic end hats but with the flux guide removed. As may be seen from Figure 1, the flux guide is a step approximation to a tapered cylinder. It operates at magnetic saturation, and its effect can be viewed to a first order as a squeezing out of flux in the center where its cross-section is a minimum, to make up for the deficiency of flux which would otherwise occur at the gap center. The thickness of the flux guide at its center section is sufficiently small so that the total flux carried by it is a small fraction of the total flux supplied by the magnet. The presence of the flux guide thus requires a negligible increase in the permanent magnet area.

The alternate design was one in which the end hats were made of a non-magnetic material and the soft iron flux guide was entirely eliminated. Figure 4 shows the axial magnetic field variation in this case. The radial variation is eliminated but now the field in the



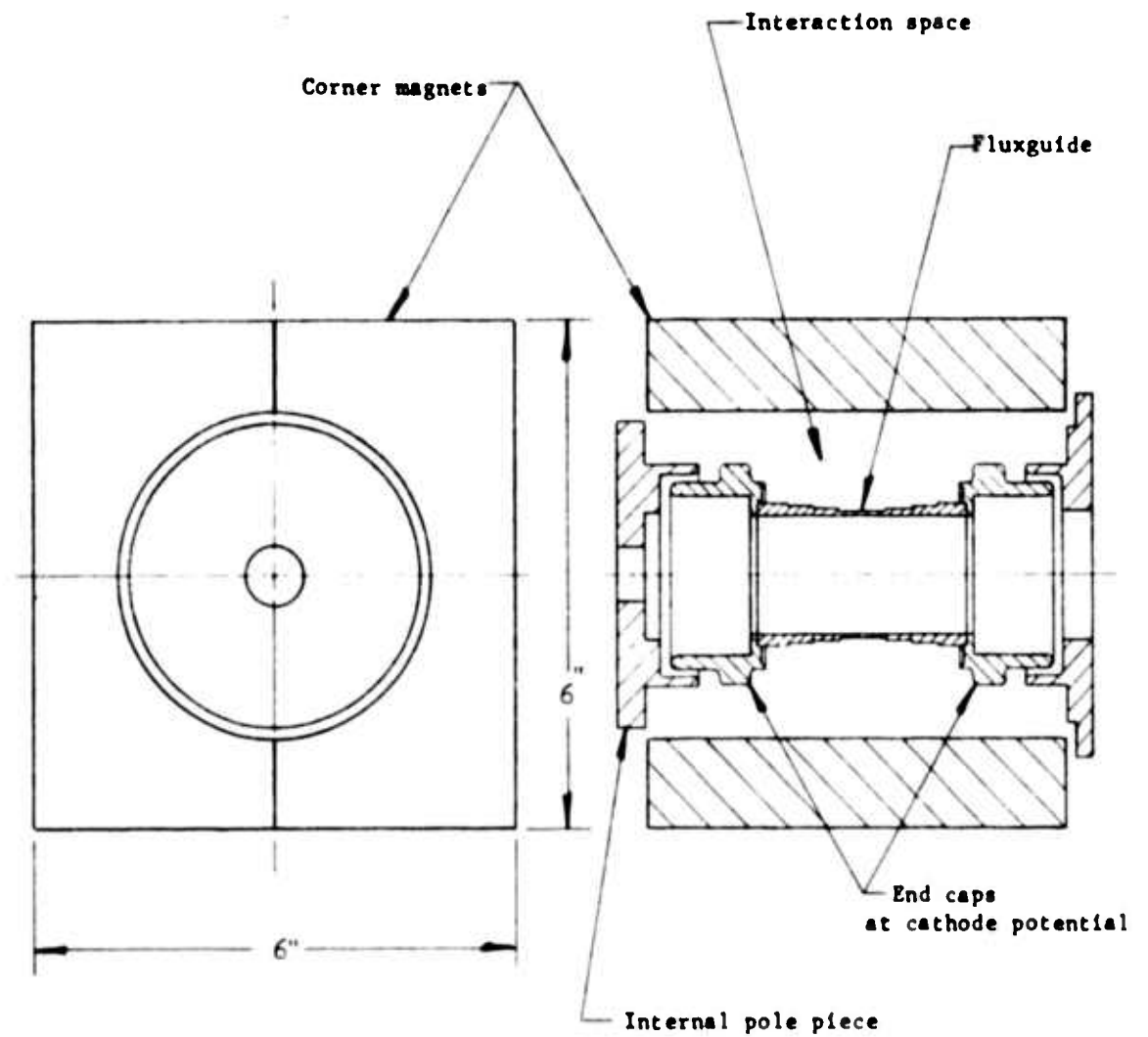
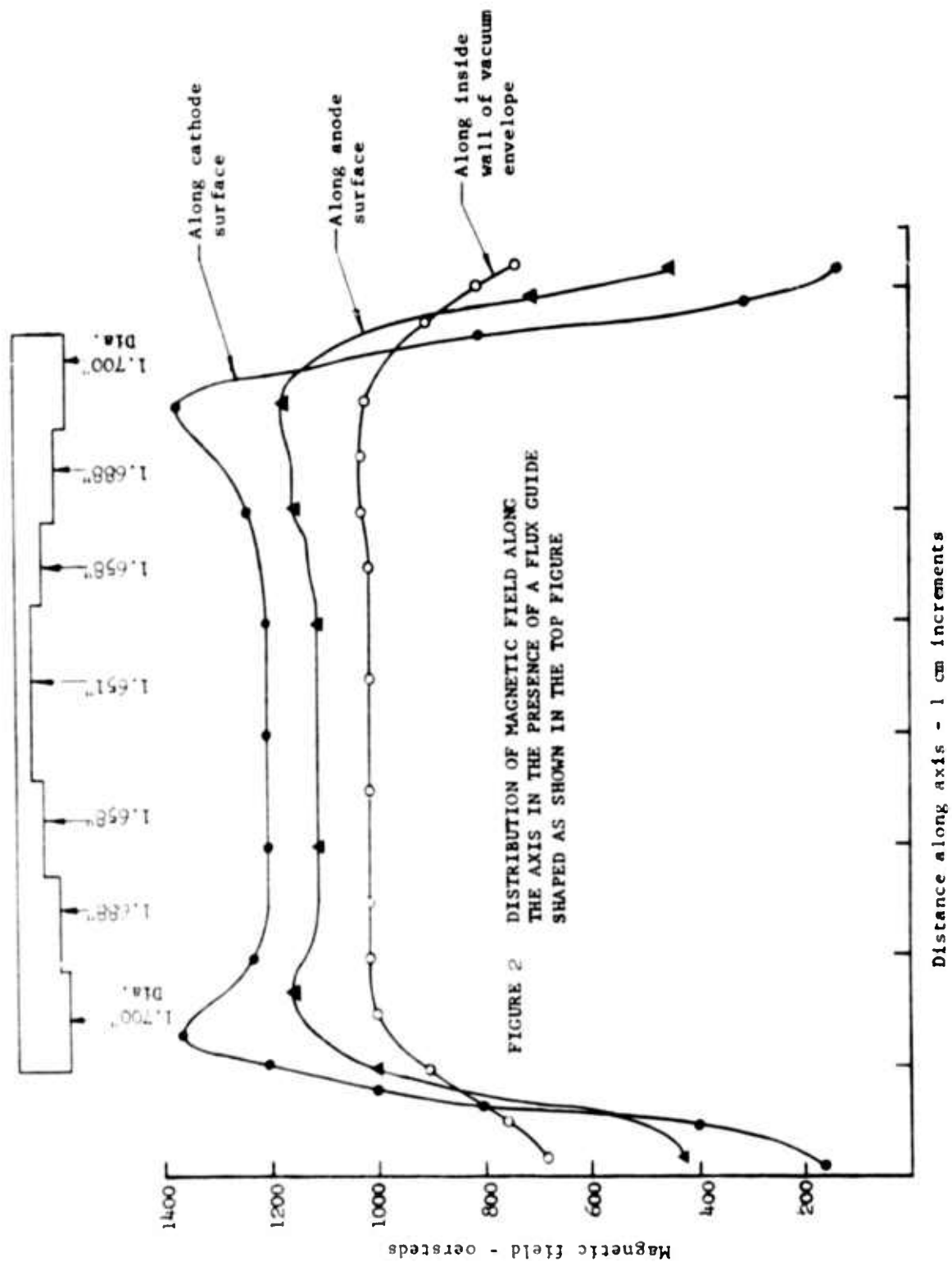
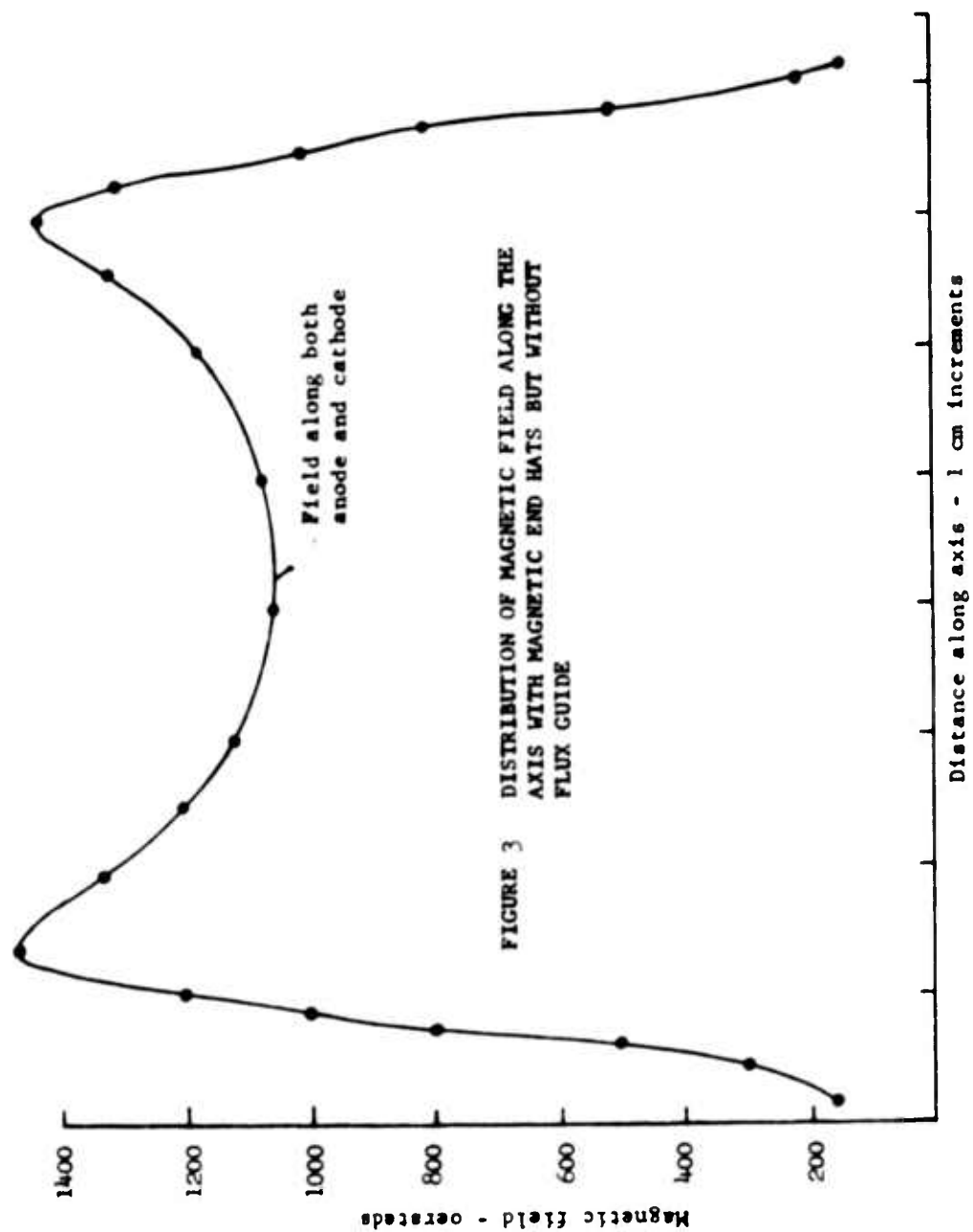


FIGURE 1 SKETCH OF THE INTERNAL MAGNETIC PARTS OF THE SFD-209  
 The flux guide steps are shown exaggerated so as to be visible. In reality they are from 3 to 15 mils high.





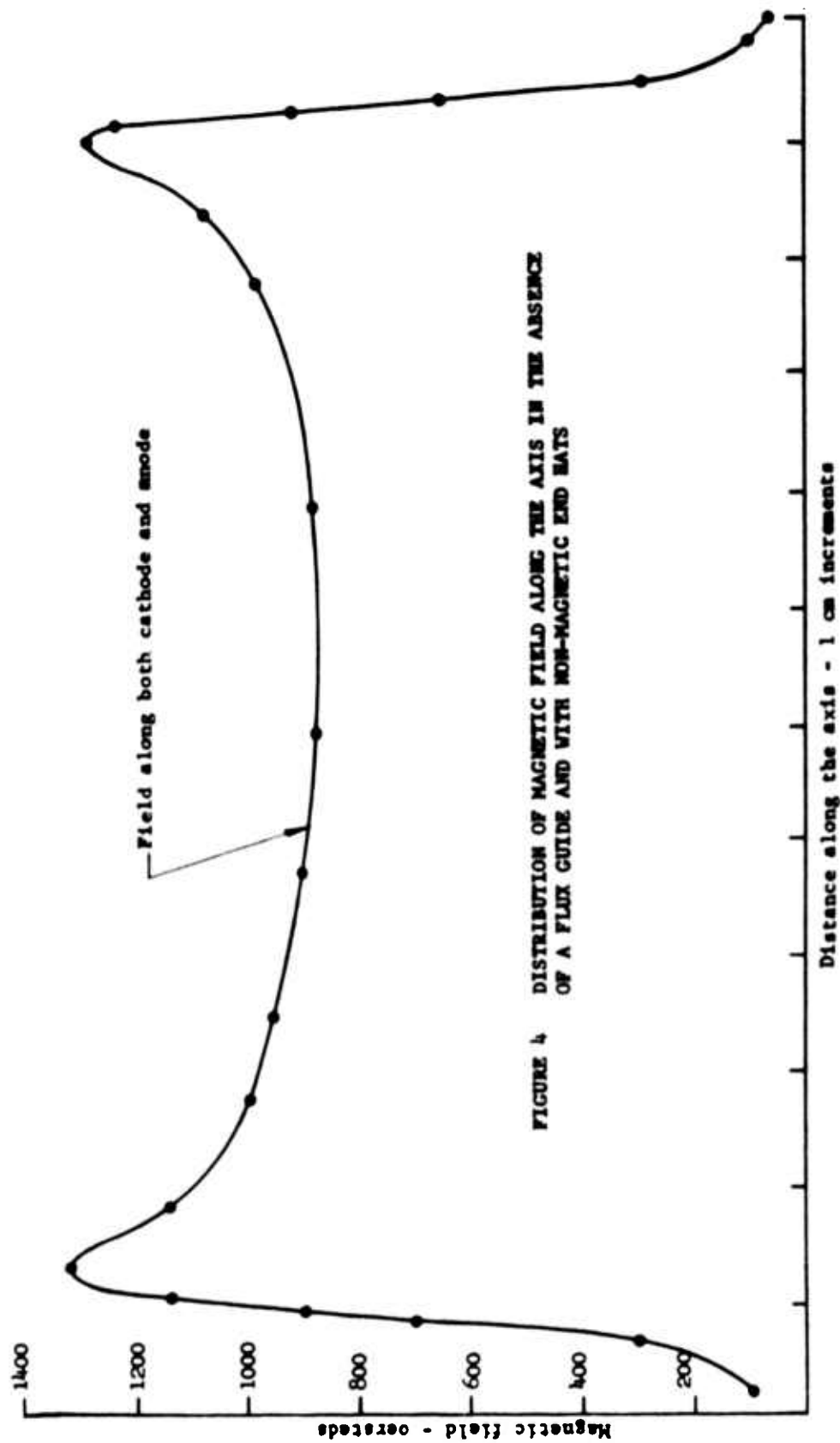


FIGURE 4 DISTRIBUTION OF MAGNETIC FIELD ALONG THE AXIS IN THE ABSENCE OF A FLUX GUIDE AND WITH NON-MAGNETIC END HATS

interaction space is the same as that in the permanent magnet material. This means that the field in the magnet must be raised to about 1000 oersteds. This can be done only at the expense of operating the magnet material at a lower energy product than if it were operated at 600 to 800 oersteds as would be possible with the flux guide. The length of the magnet is determined by the spacing of the pole pieces which must be at least the anode bar length. Thus advantage cannot be taken of the 1000 oersteds in the magnet to shorten the magnet length. These factors result in a requirement for a considerably larger magnet if the flux guide and magnetic end hats are not used.

The RF performance of the SFD-209 was evaluated using these two magnetic circuit geometries. Figure 5 shows the most conclusive results. Here V-I curves are shown for a tube with magnetic end hats and flux guide and then for the same tube as rebuilt with non-magnetic end hats and no flux guide. The V-I curves with the flux guide are much steeper and the total current available is less. The efficiency is also lower and the tube more noisy for this magnetic configuration. Results of this sort were confirmed several times over in tests on other tubes. They clearly showed that the flux guide scheme would have to be abandoned even though it provided savings in magnet weight.

Some insight into the effect of the flux guide may be seen by reference to Figure 6 which shows a sketch of the magnetic equipotentials and flux lines in the presence of the flux guide. Since the flux guide is operating saturated, the magnetic field lines need not leave it perpendicularly. The action of the flux guide is to space the equipotentials uniformly along its length, but it does this at the expense of the introduction of a considerable component of radial magnetic field. This radial field interacts with the circumferential electron velocities to produce a strong focusing force toward the center of the interaction space. Some such force is often helpful in confining the

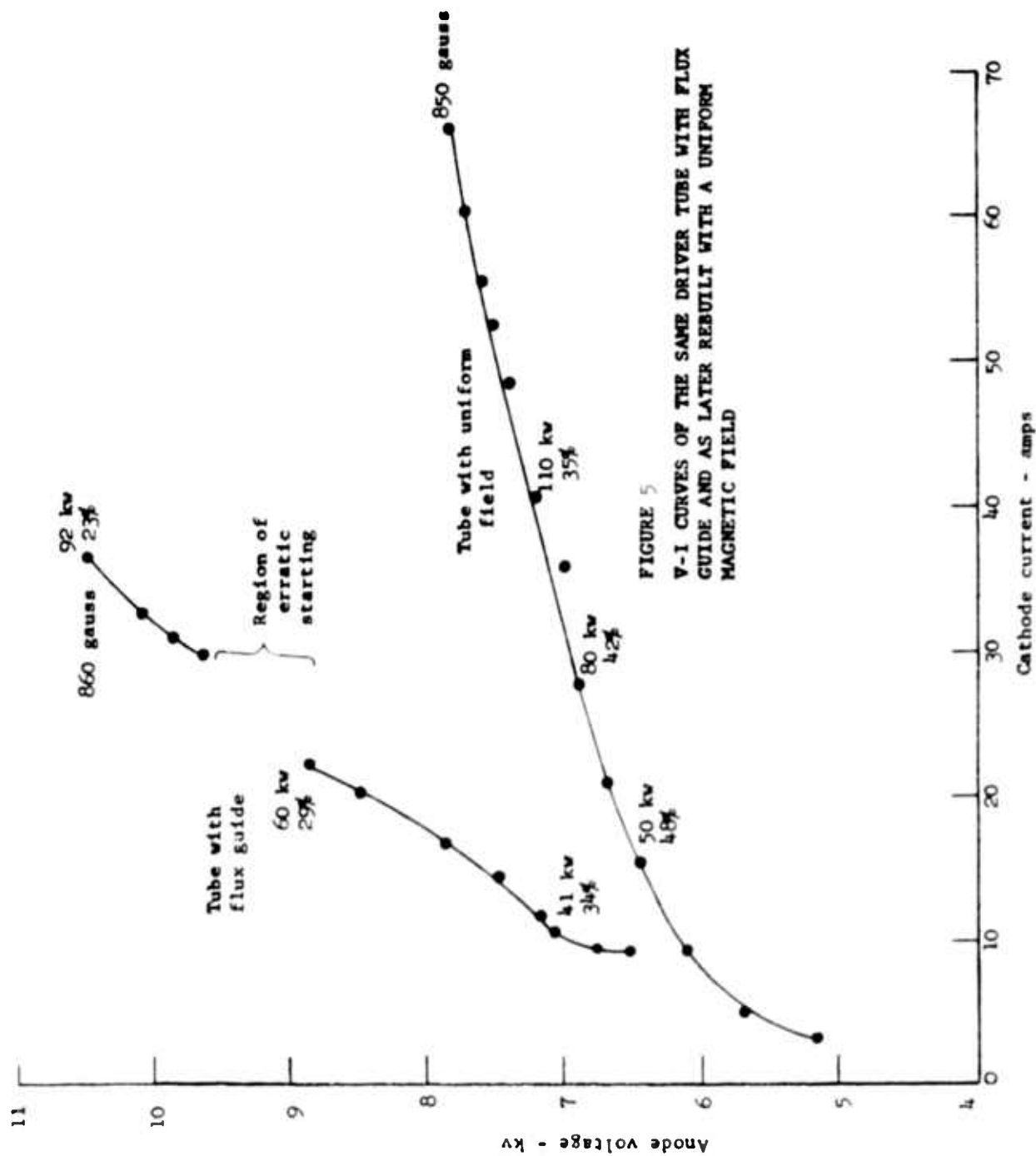


FIGURE 5  
V-1 CURVES OF THE SAME DRIVER TUBE WITH FLUX  
GUIDE AND AS LATER REBUILT WITH A UNIFORM  
MAGNETIC FIELD

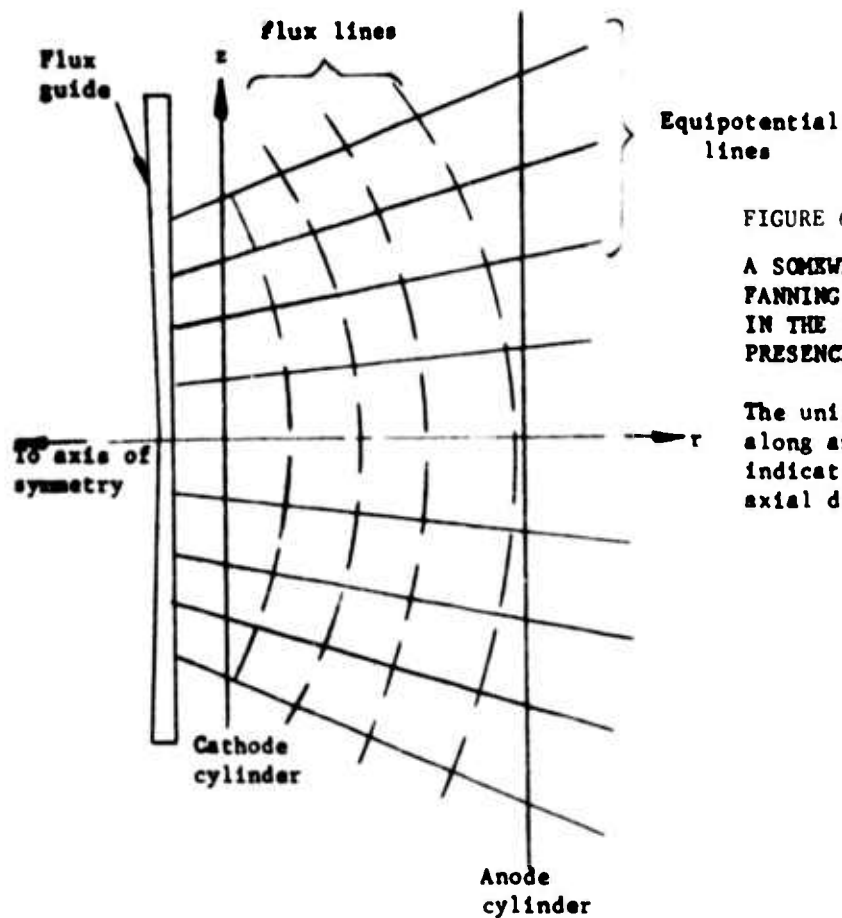
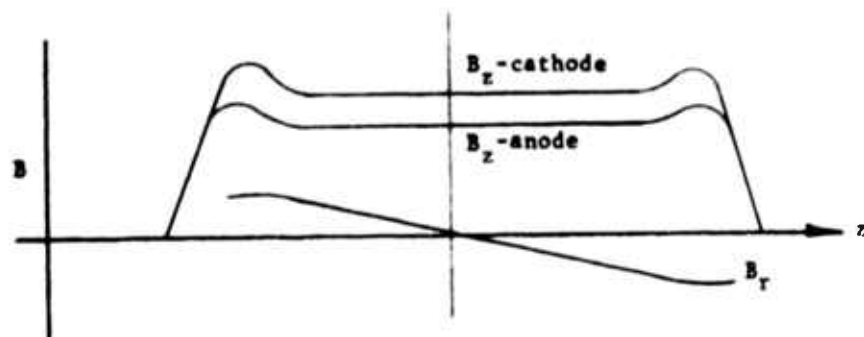


FIGURE 6

A SOMEWHAT EXAGGERATED SKETCH OF THE FANNING OUT OF MAGNETIC EQUIPOTENTIALS IN THE INTERACTION SPACE IN THE PRESENCE OF A FLUX GUIDE.

The uniform spacing of equipotentials along anode and cathode cylinders indicates the constancy of  $B_z$  with axial distance ( $z$ ).



THE AXIAL VARIATION OF  $B_z$  AND  $B_r$ . These quantities are related by  $\frac{\partial B_r}{\partial z} = \frac{\partial B_z}{\partial r}$  which follows from  $\nabla \times \mathbf{B} = 0$

electron cloud but here its effect is excessively large. Its apparent effect is to make only the central portion of the cathode effective in producing current. Hence less current is obtained for a given operating voltage than with a uniform magnetic field.

These results with the flux guide have led to abandoning its use and to choosing the second design which gives a more uniform magnetic field. The same design will be used for both the SFD-209 and the SFD-216. Various permanent magnet arrangements which were considered to go with this design are discussed in section 3.0.

## 2.2 Sources of Feedback in the SFD-209

Feedback of a signal from output to input is undesirable because it tends to enhance the noise output of the tube and because it introduces a sinusoidal component into the phase versus frequency characteristic. The noise is an attempt of the tube to oscillate and occurs at frequencies for which the feedback is positive. Actual oscillation is prevented except in the presence of very large feedback by non-linear effects which lock the space charge into the spoke pattern dictated by the input RF signal. The sinusoidal component of the phase versus frequency characteristic is undesirable because linearity of this characteristic is needed for good reproduction of "chirping" signals. Further, since the sources of feedback are less well controlled than are the basic characteristics of the circuit, the sinusoidal component they introduce into the phase characteristic will tend to have a somewhat random nature and therefore will lessen the tube-to-tube reproducibility of the phase characteristic. For these reasons it is necessary to investigate and to minimize the various sources of feedback.

The three major sources of feedback are shown schematically in Figure 7. They are:

- (1) reflections from the transducers between slow wave circuit and coaxial line



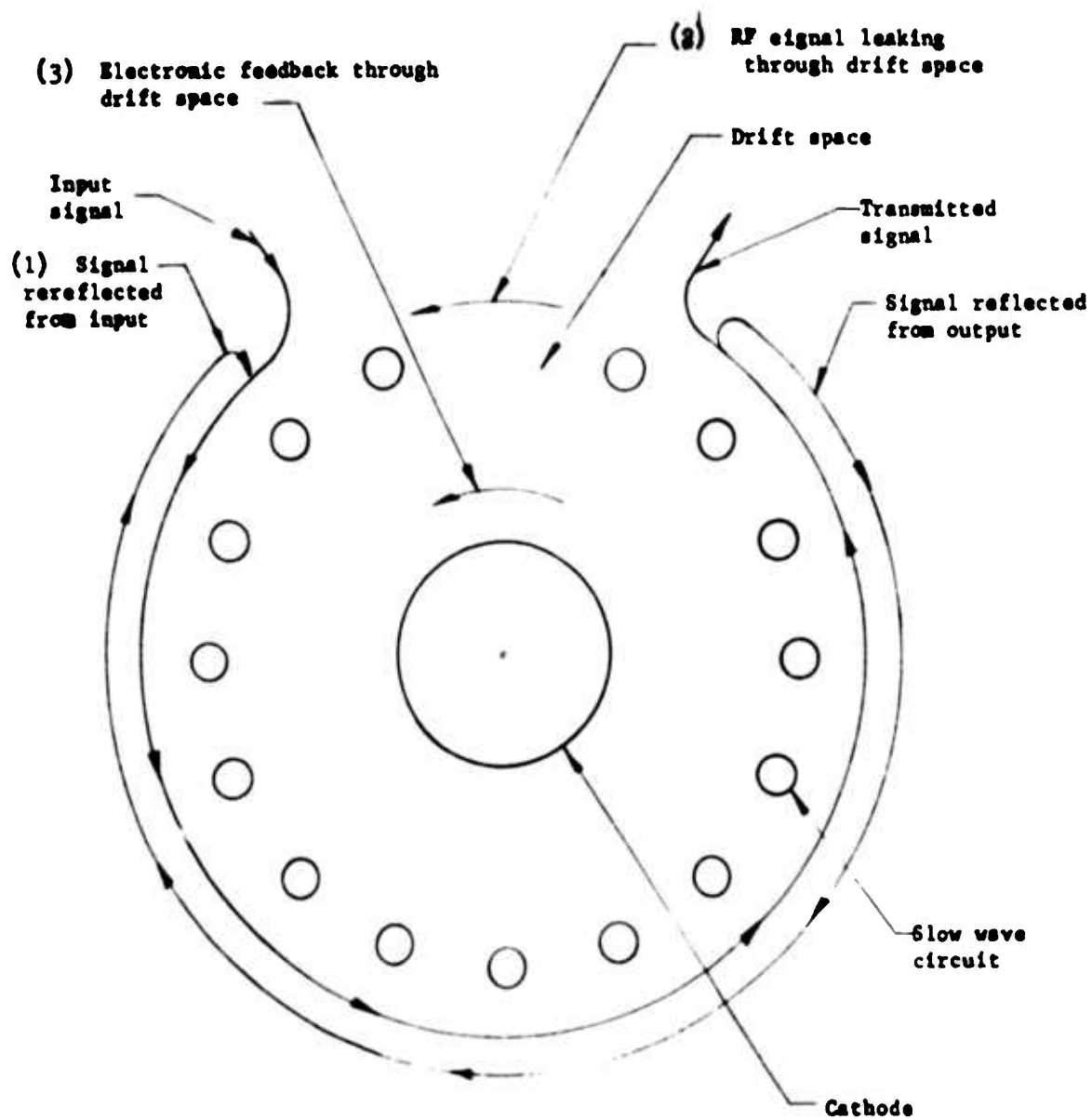


FIGURE 7 SCHEMATIC SHOWING THE THREE MAJOR SOURCES OF FEEDBACK

- (2) RF leakage through the drift space. This occurs largely because the cathode and the drift space bars opposite them act as a slow wave circuit with some finite bandwidth. It is minimized by the use of an absorber behind the drift space bars.
- (3) electronic feedback through the drift space as a result of incomplete debunching of the electron space charge as it passes through this region.

The magnitude of the first two sources may be evaluated from cold tests. Figure 8 shows the reflection from a coaxial to slow wave circuit transducer. Reflections are held to a return loss of 15 db or better over the useful part of the band. For a feedback path made up of a reflection from the output transducer, transmission back through the 2 to 3 db loss of the circuit and rereflection from the input, the loss would be about 33 db. For a 20 db gain tube, this would mean a feedback signal down 13 db on the input signal.

The magnitude of the RF feedback through the drift space may be measured by terminating the slow wave circuit with lossy material and measuring the residual transmission. In our tests we have used Emerson and Cuming, Eccosorb material. Increasing amounts of this material have been placed on the circuit until the transmission does not decrease with further additions of it. This remaining transmission must be getting from output to input via some path other than the slow wave circuit. That this path is the drift space can be checked by the introduction of lossy material here. In this manner it has been determined that the RF leakage through the drift space is in the 35-40 db range.

We have to arrive at a figure for the magnitude of the electronic feedback by more indirect reasoning. Figures 9 through 15 show the results of RF measurements on one of the SFD-209 tubes that will be used for this purpose. Figures 9 and 10 are frequency response runs at 1 kw and 5 kw peak input signal respectively. Curves are shown

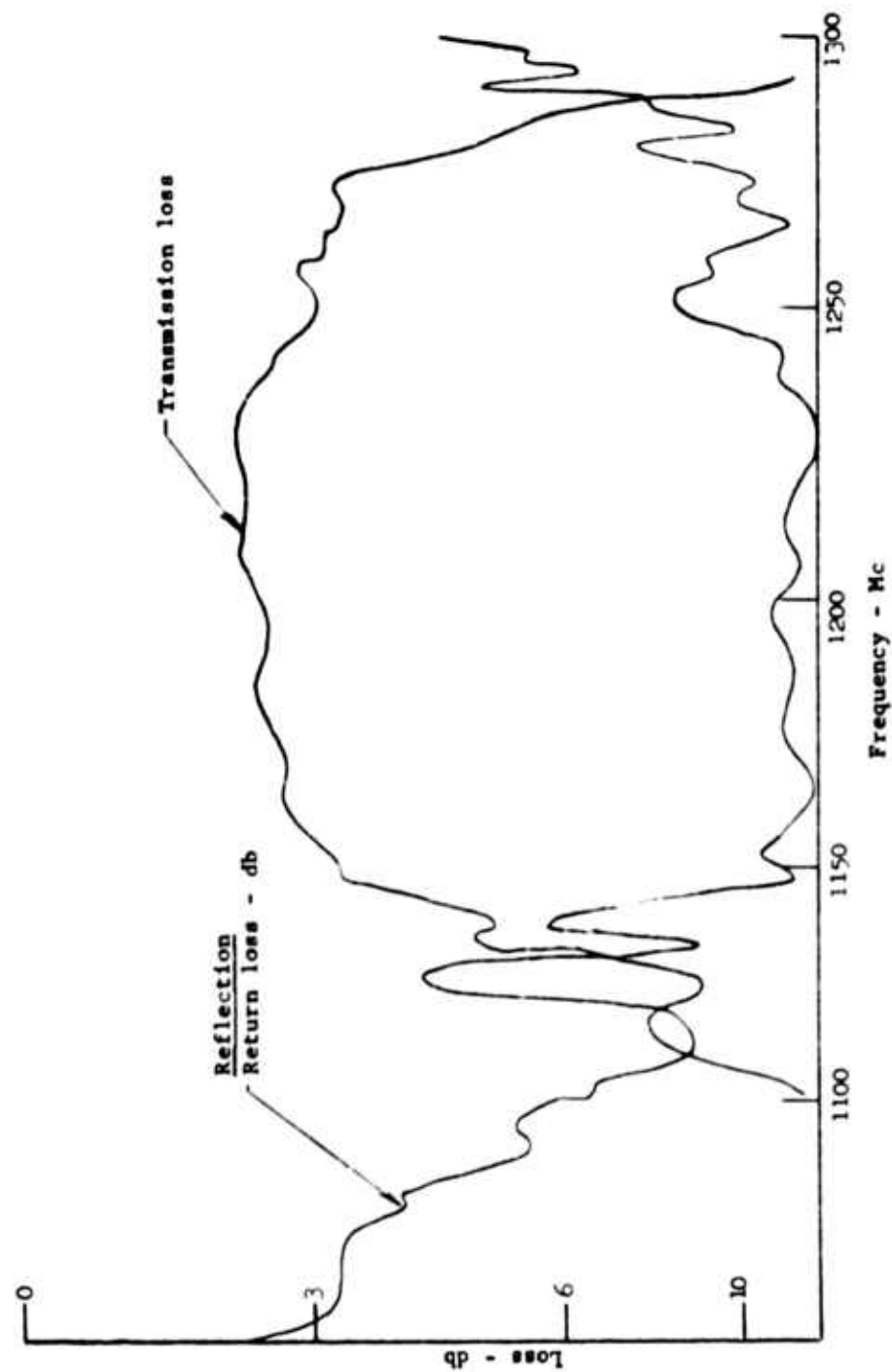


FIGURE 8 TRANSMISSION LOSS AND RETURN LOSS FOR THE SFD-209 DRIVER AS FUNCTIONS OF FREQUENCY  
 The return loss was measured with a termination connected to the output coaxial line. The reflections measured, therefore, represent the sum of reflections from the two ends of the circuit.

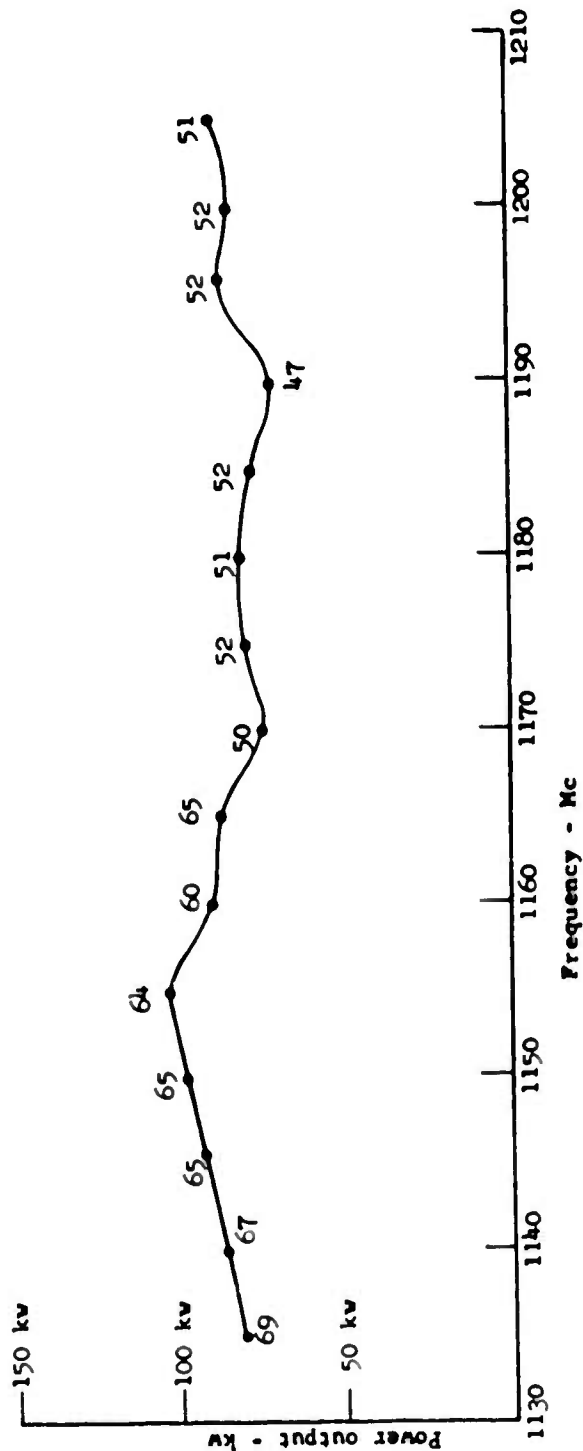
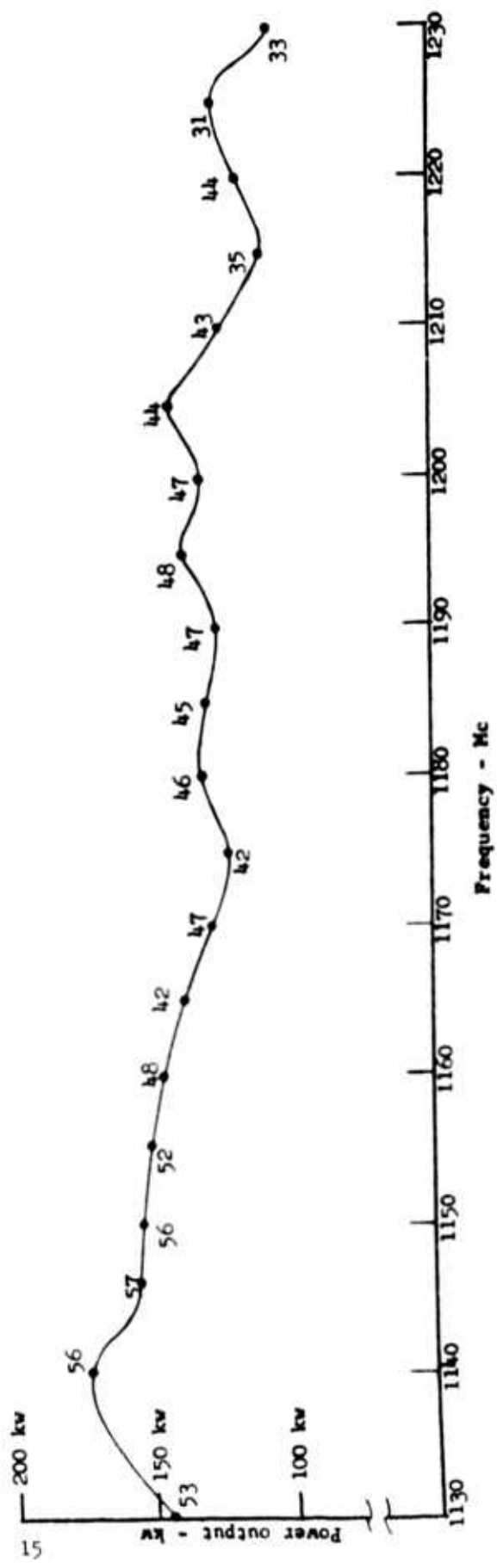


FIGURE 9 POWER OUTPUT AS A FUNCTION OF FREQUENCY FOR A RECENT SPD-209 TUBE  
 Power input was fixed at 1 kw peak and voltage at 8.2 kv. Magnetic field was 1000 gauss. Numbers alongside the points are the efficiencies in percent.

FIGURE 10 POWER OUTPUT AS A FUNCTION OF FREQUENCY FOR A RECENT SPD-209 TUBE  
 Power input was fixed at 5 kw peak and voltage was fixed at 8.7 kv.  
 Magnetic field was 1000 gauss. Numbers alongside points are the  
 efficiencies in percent.



with constant anode voltage and with the anode voltage optimized for the maximum output power. The constant voltage curves are relatively flat but the maximum output curves show a definite periodicity as a consequence of feedback. The feedback signal viewed at the tube input alternately adds and subtracts from the input signal as the total phase shift around the feedback loop varies with frequency. Thus a net input signal which is the vector sum of the input signal and the feedback signal can be considered as impressed at the input end of the slow wave circuit. As was discussed in the last report, the tube is operated as a saturated amplifier and the output signal amplitude changes only a small amount with input signal changes. This is the reason the effect of feedback is not in evidence in the constant anode voltage curves. When the anode voltage is varied, however, the effect of feedback in determining the effective input signal amplitude becomes evident. When the feedback is positive, the effective input signal is larger and the anode voltage can be raised to a higher value without the input signal losing control of the space charge and causing the tube to become noisy. The reverse is true when the feedback is negative. Thus the periodicity caused by feedback comes clearly into evidence when the anode voltage is optimized for maximum output.

Feedback because of reflections from the transducers may be separated from feedback through the drift space caused by either RF leakage or incomplete electron debunching by the periodicity of the output variations as a function of frequency. If the feedback is caused by reflections, the feedback path length is twice the length of the slow wave circuit - i.e., the feedback signal travels from input to output, is reflected there and travels back to the input where it is reflected again from the transducer to coaxial line. The total phase shift in the feedback path is thus  $2N\theta$  where  $N$  is the number of circuit periods and  $\theta$  is the phase shift per section. Suppose the

feedback is positive at a frequency for which the phase shift per section is positive and again for a frequency for which the phase shift per section is  $\theta + \Delta\theta$ . The total change in phase of the feedback signal between these two frequencies is  $2\pi$ . Thus we find that

$$2N\Delta\theta = 2\pi \quad \text{or} \quad \Delta\theta = \frac{\pi}{N}$$

If the feedback is via the drift space the feedback signal traverses the slow wave circuit once and then returns along an electrically short path to the input. For this case, neglecting the phase shift through the drift space, we find

$$\Delta\theta = \frac{2\pi}{N}$$

Thus the periodicity for drift space feedback is twice what it is for circuit reflections.

Figure 11 shows an  $\omega$ - $\beta$  curve for the tube used to obtain the data of Figures 9-15. For the observed periodicity of about 20 Mc in Figures 9 and 10, the periodicity in  $\theta$  is about 8 degrees. This corresponds very closely to what we would expect for feedback through the drift space.

Figures 12 and 13 show performance charts at 1 kw and 5 kw drive at a frequency for which the feedback is regenerative and Figures 14 and 15 show the same data at a frequency for which the feedback is degenerative. From a study of these results, we find that the effect of going from a regenerative to a degenerative frequency is less than that of going from 5 to 1 kilowatt drive at a fixed frequency. Further study shows that a reasonable conclusion is that going from regenerative to degenerative frequencies is roughly equivalent to reducing the power halfway between 5 and 1 kilowatt drive. Thus the

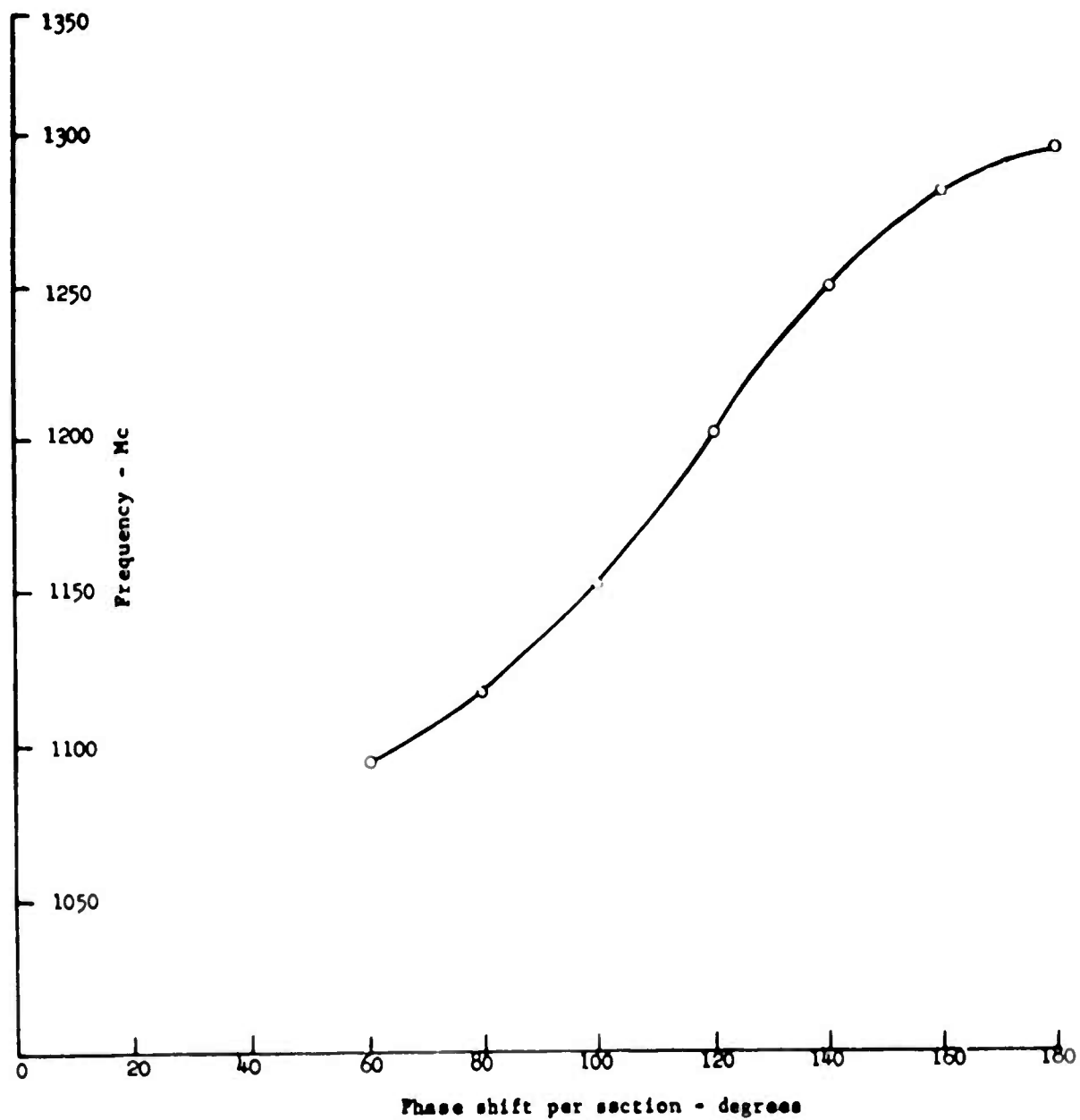


FIGURE 11 THE  $\omega$ - $\beta$  CURVE FOR THE 9FD-209 TUBE WHICH GAVE THE PERFORMANCE SHOWN IN FIGURES 9 AND 10 AND FIGURES 12 THROUGH 15



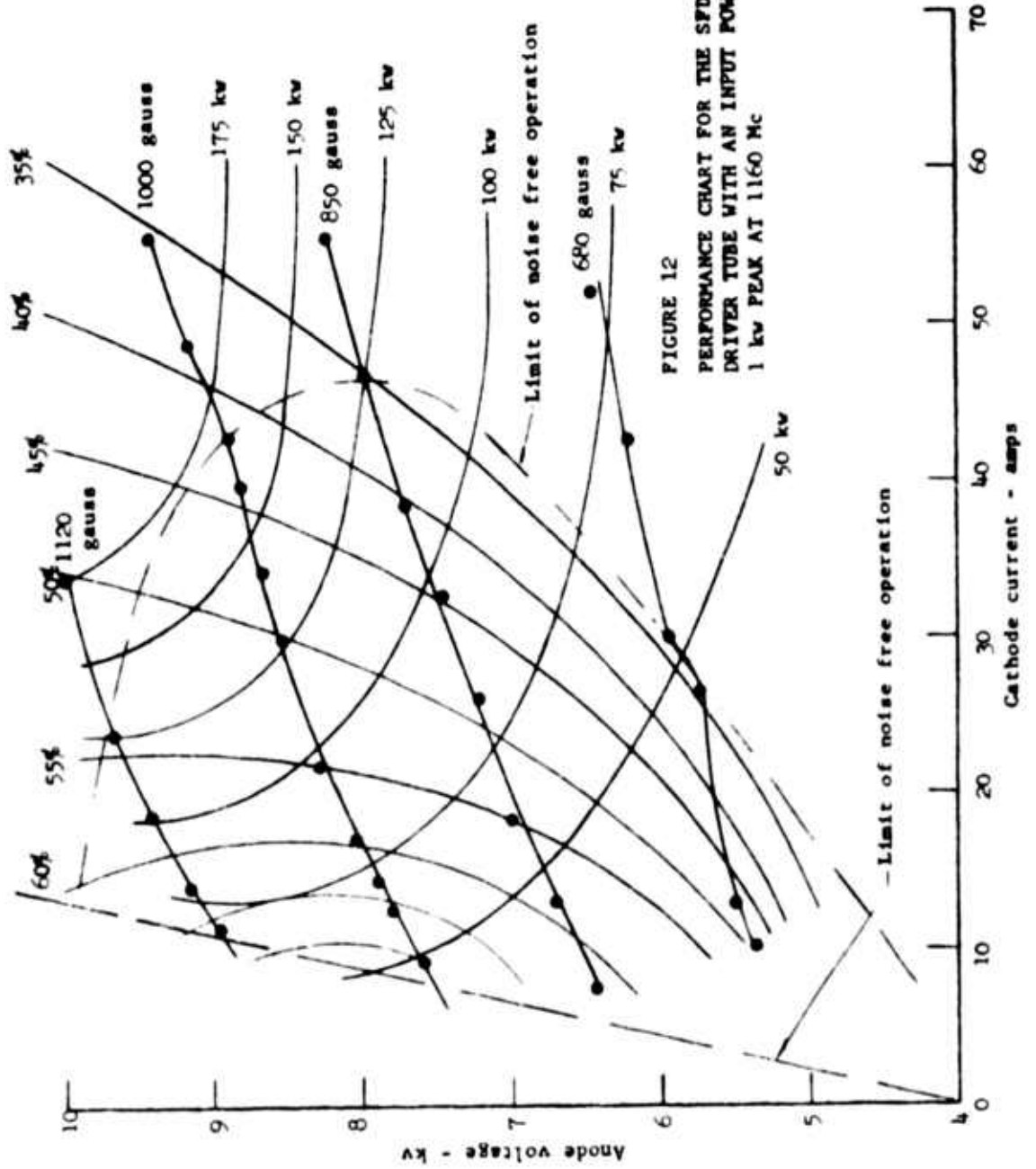
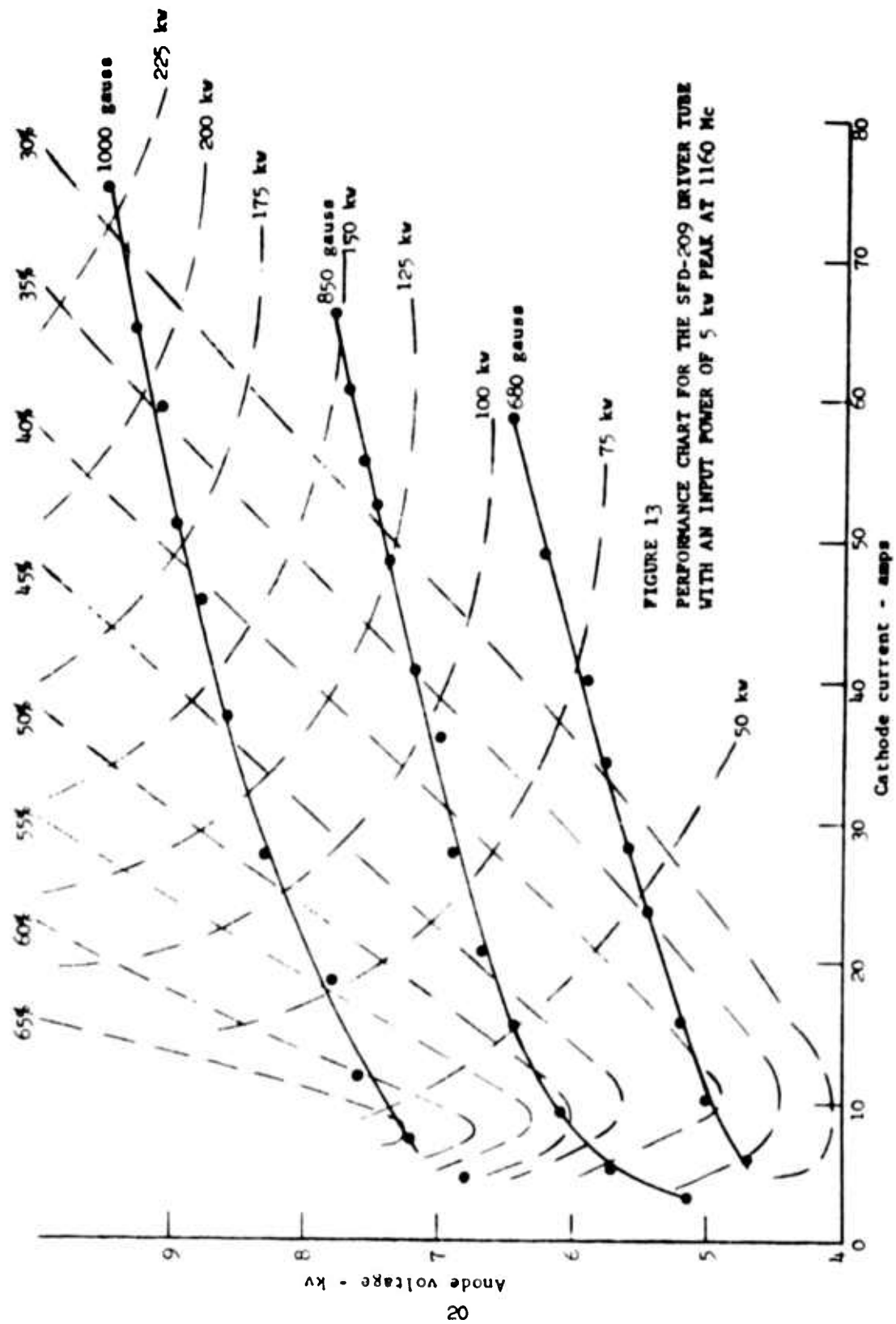


FIGURE 12  
PERFORMANCE CHART FOR THE SFD-209  
DRIVER TUBE WITH AN INPUT POWER OF  
1 kw PEAK AT 1160 Mc



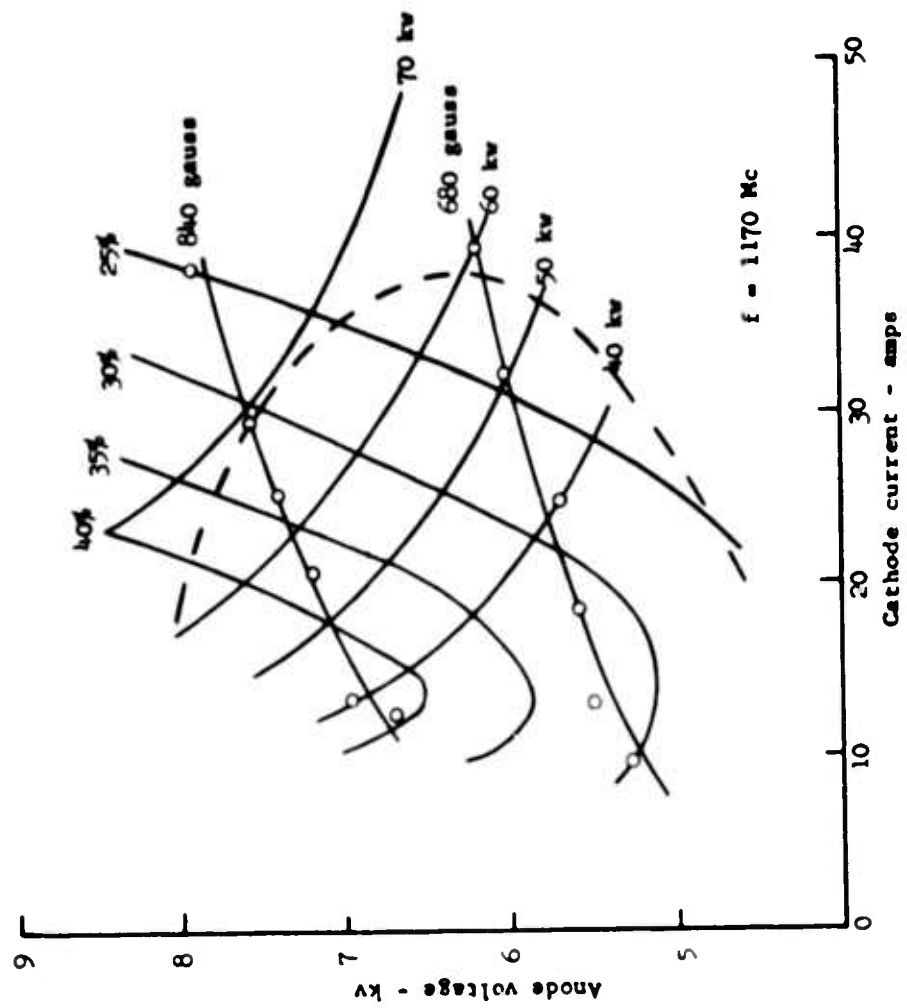


FIGURE 14 PERFORMANCE CHART FOR 1 kv INPUT FOR A FREQUENCY FOR WHICH THE FEEDBACK IS DEGENERATIVE

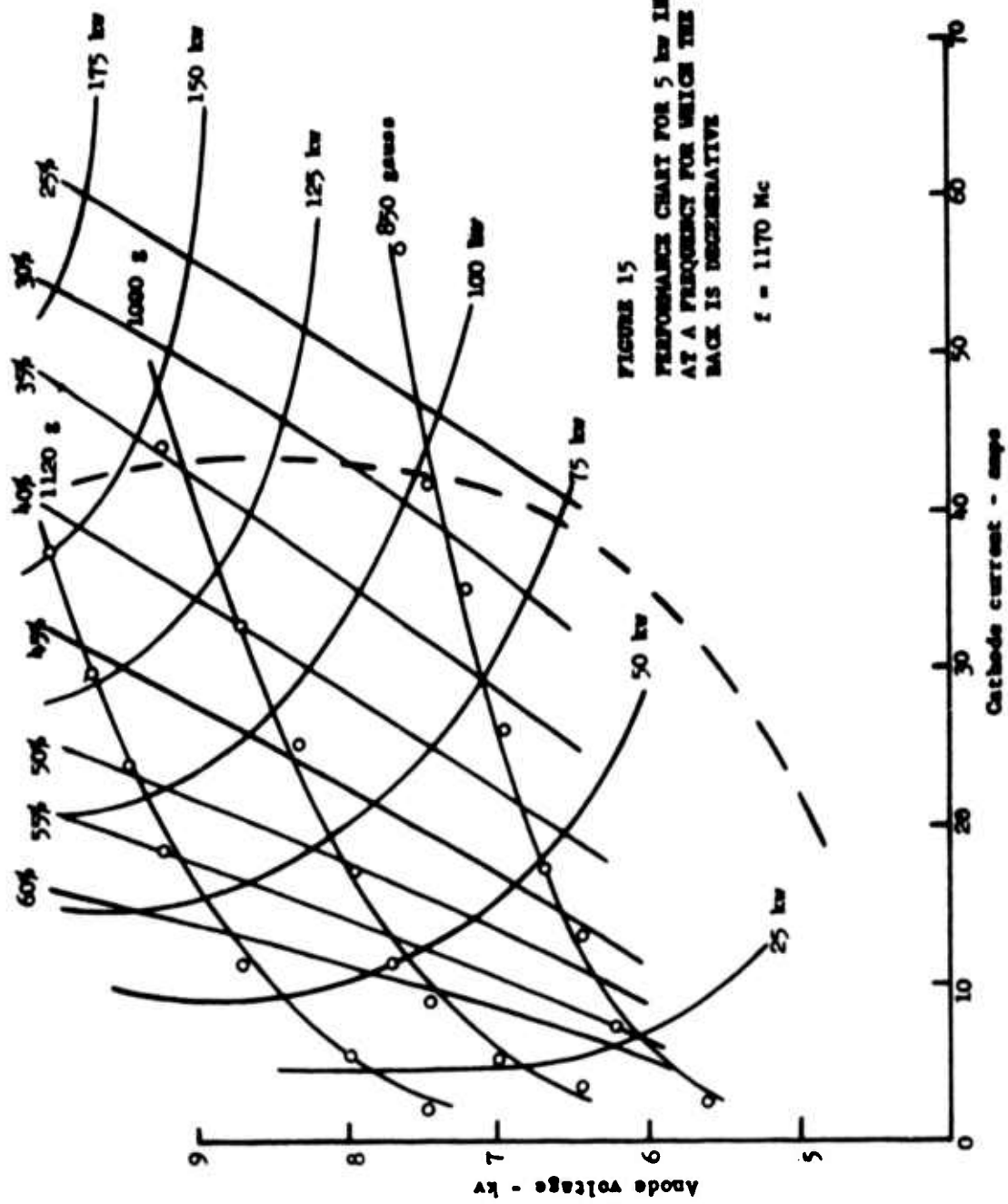


FIGURE 15  
 PERFORMANCE CHART FOR 5 kw INPUT  
 AT A FREQUENCY FOR WHICH THE FEED-  
 BACK IS DEGENERATIVE  
 $f = 1170 \text{ Mc}$

RF field strength at regenerative and degenerative frequencies is approximately in the ratio of the square root of 2.5 or 1.58 to 1. Such a ratio is produced by an interfering component down 13 db on the main signal component. In this case the main signal component is the input signal and the interfering component is the feedback signal. The feedback ratio is then 13 db plus the tube gain of about 14 db or about 27 db - i.e., the loss through the feedback path is about 27 db.

It remains to determine whether this feedback is electronic (i.e., due to incomplete electron debunching) or RF leakage. The RF leakage measured on cold test was in excess of 35 db so we conclude by the process of elimination that we have electronic feedback with an equivalent loss in the feedback path of about 27 db. Thus for this tube we arrive at the following feedback ratios

- |  |              |
|--|--------------|
| (1) for feedback by circuit reflections            | -33 db       |
| (2) for feedback by RF leakage through drift space | -35 to 40 db |
| (3) for electronic feedback                        | -27 db       |

We would like to have greater values for these ratios. For example in a 30 db gain tube with a feedback ratio of -40 db, the feedback signal will be 20 db down on the input signal. The interference of this signal with the input signal would be expected to produce a 5° peak amplitude sinusoidal component in the phase versus frequency characteristic. This is about the maximum value we would like to see for such a component. Means of reducing these feedback ratios which are being tried out in new tube designs will be discussed in section 3.0. Another means of measuring electronic feedback which gave a much lower value for a different tube will also be discussed in the next section on phase measurements. This result is not necessarily in contradiction to that presented in this section because slight differences in tube geometry could make a considerable difference in the feedback ratio.

### 2.3 Phase Measurements and Phase Measuring Equipment

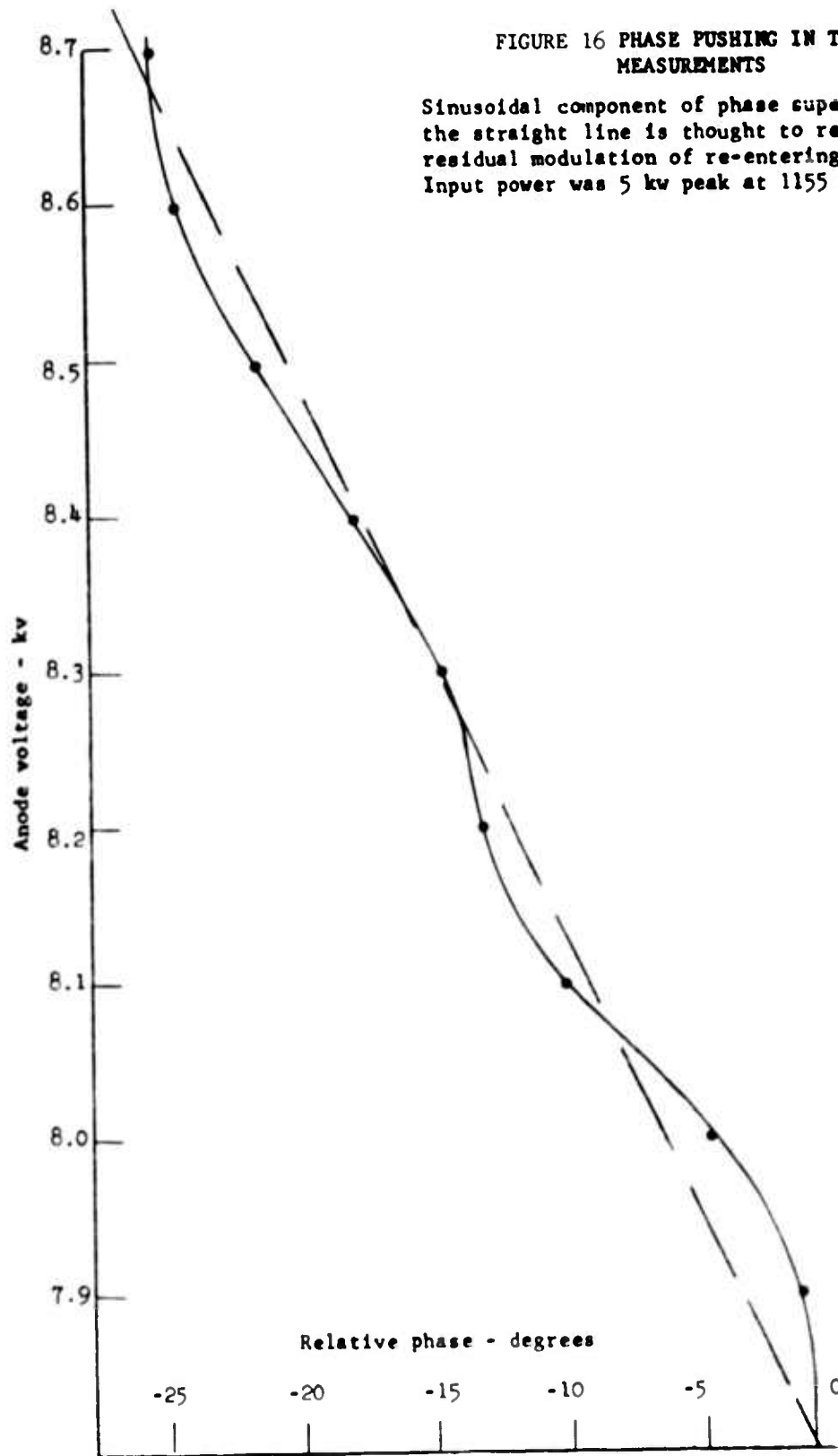
The only phase measurements made thus far are those of "phase pushing". This term refers to the variation in output phase as a function of anode voltage. Figure 16 shows measurements of this property. These measurements were taken using a slotted line set up as shown in Figure 17. At the reference value of anode voltage, a null was established in the line by adjusting the attenuators so that equal signal amplitudes were fed into the line from the opposite ends. The position of the null was then tracked as anode voltage was varied without further changes in attenuator position. Figure 16 shows the resulting relative phase shift as a function of anode voltage. It is seen that this takes the form of a linear slope of about 2 degrees phase shift per 1% voltage variation with a superimposed sinusoidal component of about  $4^\circ$  peak to peak amplitude.

The sinusoidal component found here is believed to be the result of electronic feedback. The phase of the residual component of bunching in the electron cloud emerging from the drift space will be a function of anode voltage which determines the drift velocity of electrons through the drift space. The periodicity of the effect would correspond to the electron velocity in the drift space being about half what it is in the main interaction space. In view of the increased anode-to-cathode spacing in this region (because of the cathode cut back) this is not wholly unreasonable though it is a bit less than would be predicted on the basis of spacing alone. The peak-to-peak amplitude of the sinusoidal component would indicate that the feedback signal is down about 27 db on the input signal. Under the conditions of these measurements, the tube gain was about 13 db so the feedback ratio would be about 40 db.

Studies were made during the period of this report of the best way of making the phase versus frequency measurements. The methods studied were

FIGURE 16 PHASE PUSHING IN THE SFD-209  
MEASUREMENTS

Sinusoidal component of phase superimposed on the straight line is thought to result from residual modulation of re-entering space charge. Input power was 5 kw peak at 1155 Mc.



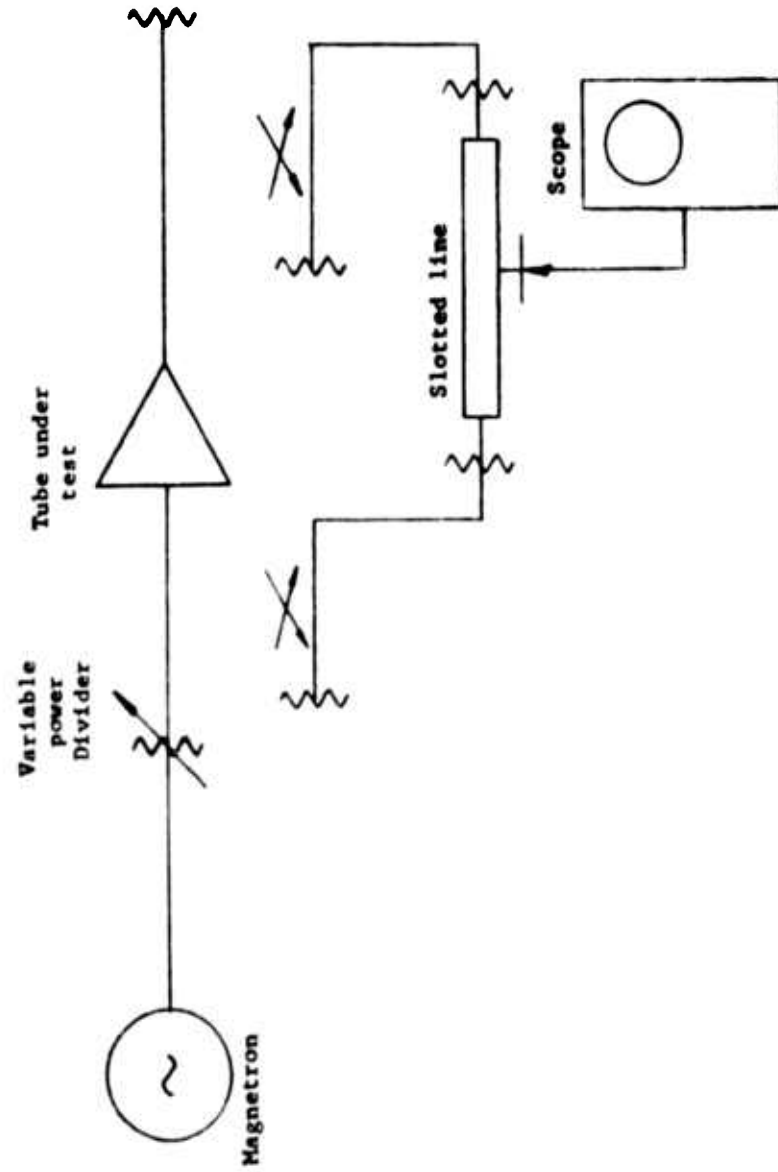


FIGURE 17 SIMPLIFIED BLOCK DIAGRAM OF THE TEST SET USED TO MEASURE PHASE PUSHING



(1) Hetrodyne system in which the phase information is converted to a fixed IF frequency at which phase comparisons may be made. This system has the advantage of eliminating problems of calibrating the phase versus frequency characteristics of the phase reference. A block diagram of a system suggested to us by the Merrimac Corporation is shown in Figure 18. The double modulation scheme is used so that image frequencies can be conveniently filtered out in the reference path. The phase resolver used is capable of accuracies of 0.1 degree. Because of its complexity this scheme was the most expensive of all those considered. Further it had not been fully engineered in this double modulation form so that its accuracy and its problems could not be fully evaluated. These considerations led us to reject this system.

(2) Bridge system in which a simultaneous amplitude and phase balance is required. Figure 19 shows a block diagram of such a system. This system has been used in phased array studies at Lincoln Laboratories. It is excellent for CW measurements. For pulsed measurements it poses a problem in case the tube under test exhibits amplitude compression as do the crossed-field amplifiers. In this case the pulse shapes fed to the two arms of the bridge may have different shapes. A perfect balance of the bridge could not then be obtained over the full width of the pulse. The bridge output is quite sensitive to the balance condition. Thus if balanced at the center of the pulse interval there would be large output spikes at the beginning and end of the pulse. These spikes might cause overloading of the video amplifiers. The sensitivity of the output to amplitude balance would in any case make the interpretation of phase variations within a pulse extremely difficult. This scheme was rejected for this reason.

(3) Bridge system insensitive to amplitude variations. Figure 20 shows the block diagram of such a system. The two signals must be fed into the bridge exactly in quadrature to insure insensitivity



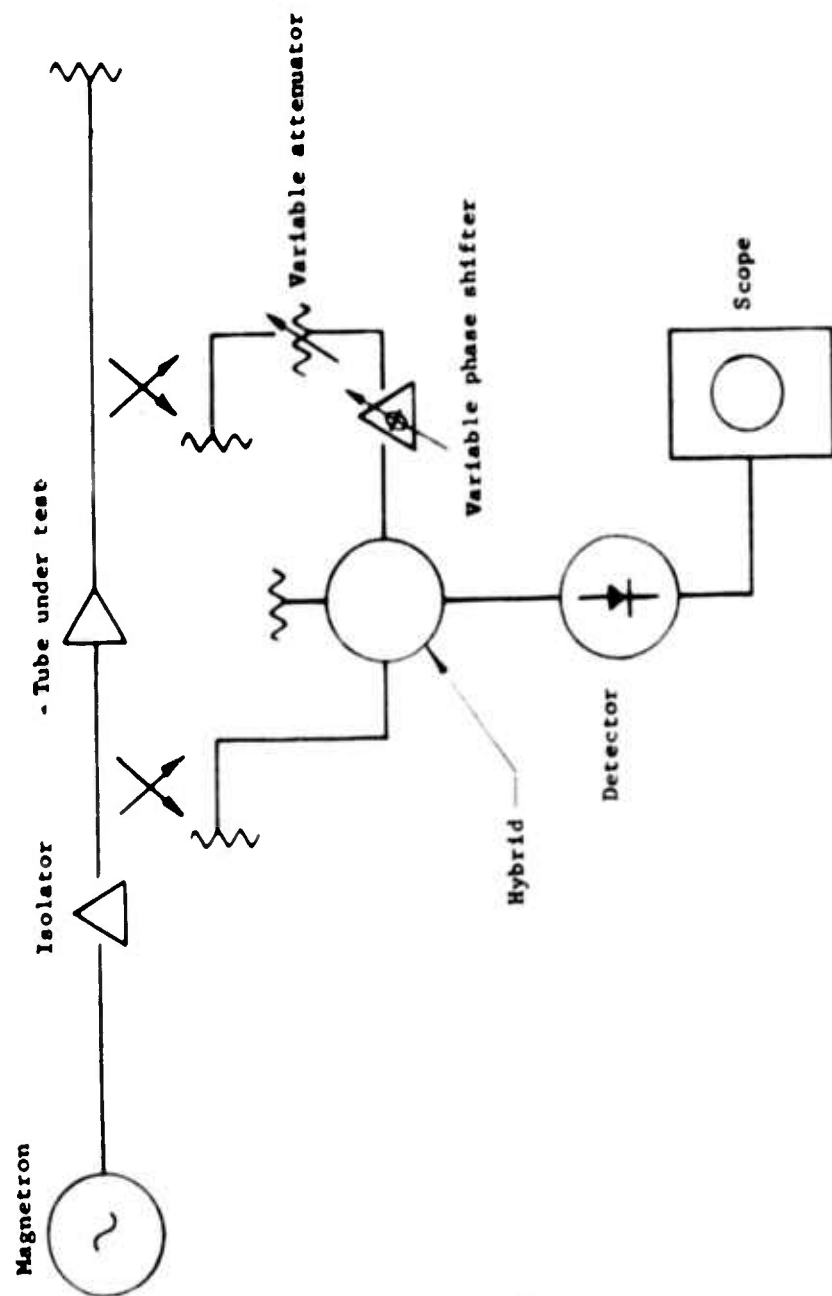


**FIGURE 19** BLOCK DIAGRAM OF PHASE BRIDGE SET UP REQUIRING A SIMULTANEOUS AMPLITUDE AND PHASE BALANCE. A HYBRID JUNCTION IS USED AS THE PHASE COMPARATOR

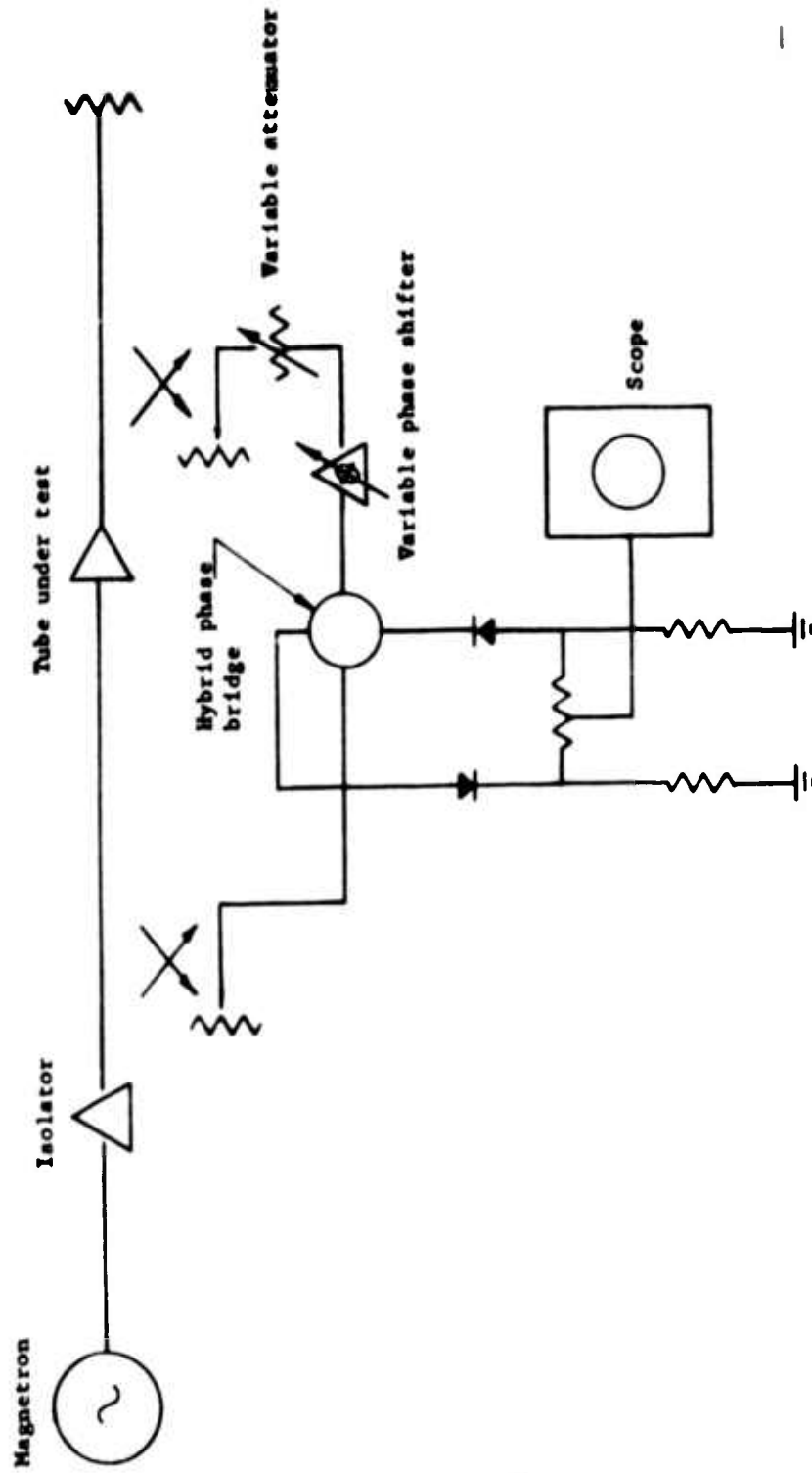


**FIGURE 20 BLOCK DIAGRAM OF PHASE MEASURING SYSTEM IN WHICH THE OUTPUT OF THE PHASE DETECTOR IS INSENSITIVE TO AMPLITUDE VARIATIONS IN THE INPUT ARMS**

The bridge is balanced and output is zero when the two inputs to the hybrid are in phase quadrature.

to amplitude variations. The two detectors must track simultaneously in amplitude and frequency and the bridge must stay in balance over the full frequency range. This appeared to be more of a development problem than we wanted to tackle.

(4) Double probe slotted line technique. Figure 21 shows a block diagram of this system. The difference in output from the two detectors when the probe is located at the center of the line is proportional to the difference in phase of the signals fed into opposite ends of the line. The line must be calibrated at each frequency by moving the double probe to the positions for maximum differential output and adjusting the output of the differential amplifier to a reference level corresponding to  $\pm 90^\circ$ . The calibration is a function of the amplitude of the signals in the sense that the output is proportional to the product of the input amplitudes. There are no large spikes of output during rise and fall time of the pulses as in method (2) above although the calibration is different during the rise and fall time than it is on the top of the pulse. As compared with a single probe slotted line, the double probe line has the advantages that phase readings can be taken directly from a meter and that nulls of the output pattern are always infinitely deep even if the signals applied to the two ends of the slotted line are not equal. The principal disadvantage of this technique is that reflections of the reference signal, entering at end A of the line in Figure 21, from end B appear as additions to the test signal entering at end B and vice versa. If either of these signals is much larger than the other, this can be a very serious effect. This difficulty is encountered in a single probe line as well as a double probe line. In spite of these difficulties we have chosen the double probe line method for our measurements. A line and indicating unit have been obtained from the Wiltron Company. A pair of specially matched padding attenuators were also obtained. When connected to the

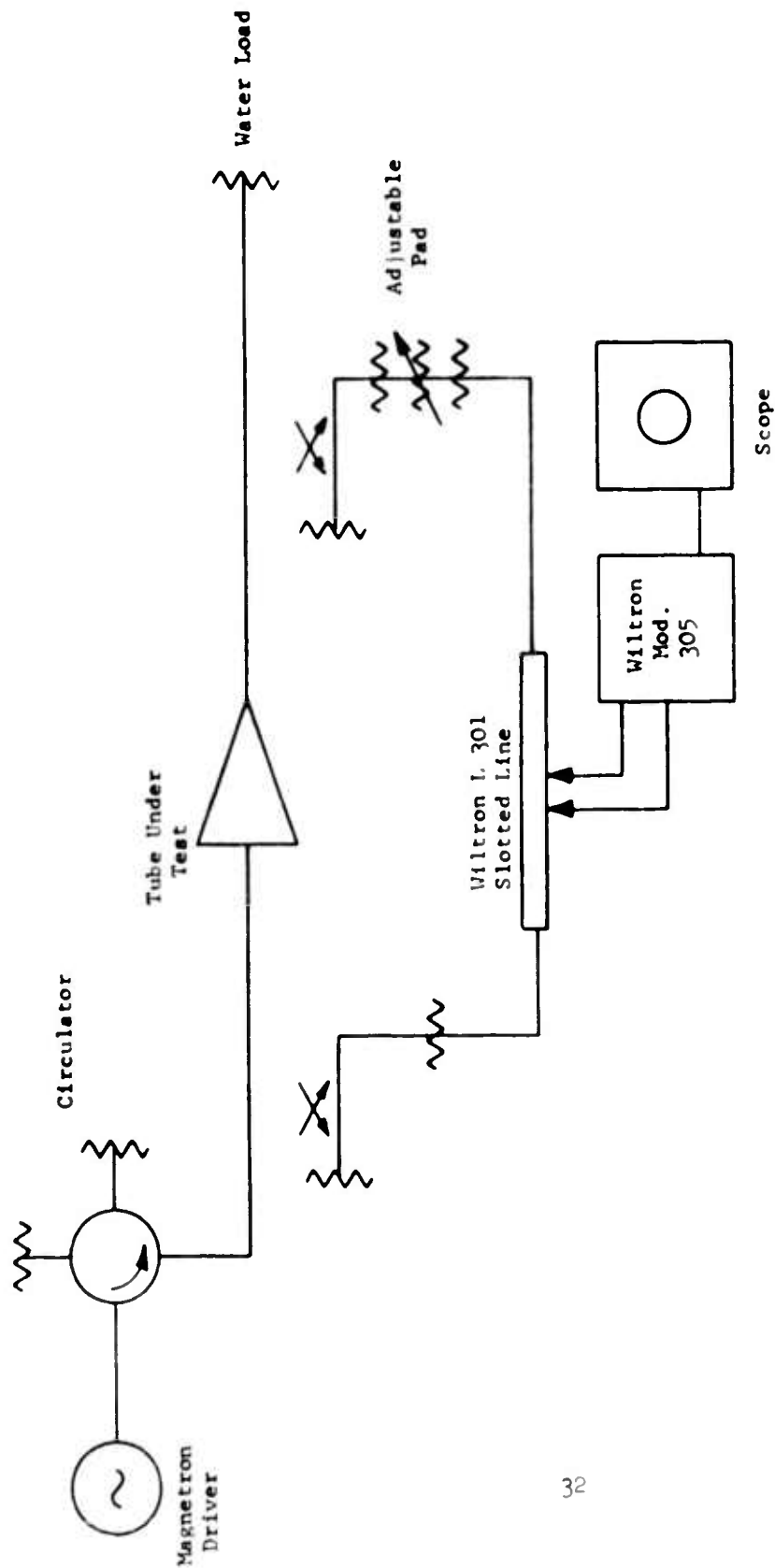


FIGURE 21 BLOCK DIAGRAM OF PHASE MEASURING EQUIPMENT TO BE USED IN TESTING THE L-BAND TUBES. THE WILTRON PHASE MEASURING SYSTEM, CONSISTING ESSENTIALLY OF A DOUBLE PROBE SLOTTED LINE AND DIFFERENTIAL AMPLIFIER AND DETECTOR WILL BE USED. IT WILL BE NECESSARY TO EMPLOY EXTREME CARE IN SETTING UP THE SYSTEM TO MINIMIZE THE ERRORS CAUSED BY MISMATCH EFFECTS. SPECIAL DIRECTIONAL COUPLERS AND ATTENUATORS WILL BE REQUIRED

line they have a VSWR of about 1.03. For equal input signals the maximum phase error that can be caused by reflections from ends of the line is about plus or minus one degree. Even this effect can be calibrated out by a proper measurement procedure. To calibrate the whole system, the tube under test will have to be replaced by a known length of transmission line. To equalize the inputs to the slotted line, a pad will then have to be removed from the measuring system as shown in Figure 21. The phase characteristics of this pad will have to be carefully measured as a separate problem.

All the equipment necessary for the phase measurements has now been acquired and assembly of the phase measuring system is starting.

#### 2.4 Control Electrode Characteristics

The control electrode characteristics of the SFD-209 and SFD-216 were investigated. Figure 22 shows the basic control electrode circuit discussed in the last report and used in these tests. Figures 23 and 24 show oscillograms of the RF pulses and of the control voltage and control current pulses. The inverting transformers used in these experiments have proven to be somewhat of a problem. Initially we did not know what control electrode impedance to design for and the transformers we obtained turned out to be for too high an impedance level. As a consequence they were very heavily loaded in this application and their rise times were quite long. This is in evidence in the oscillograms. A second problem with a pulse transformer is that the load it sees is quite variable, from a low value when the pulse is first applied to a very high value after the tube has turned off. This causes a problem for the transformer then tends to oscillate when the tube turns off. If the oscillation is severe enough, the control voltage can drop to a point where the tube turns on again. The solution to this is to put a damping resistor across the transformer secondary as shown in Figure 22. The presence of this resistor however wastes power and further slows the transformer rise time.

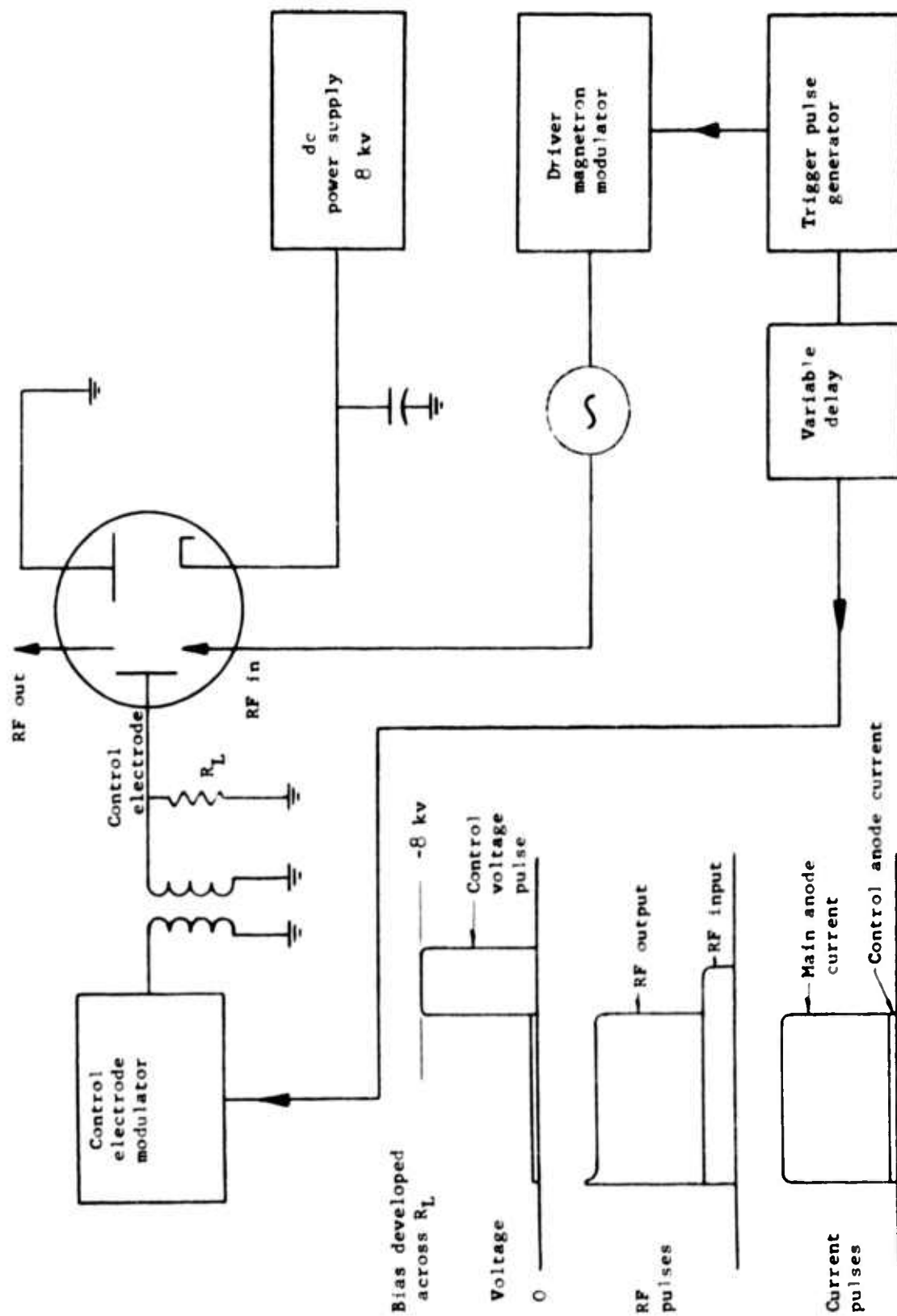
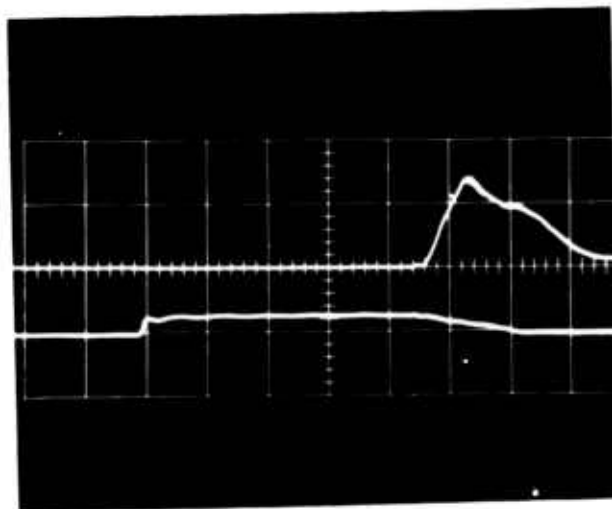


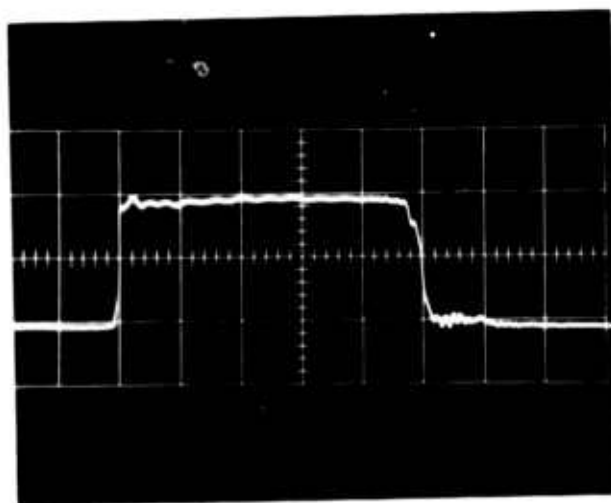
FIGURE 22 BLOCK DIAGRAM OF THE PULSING SCHEME USED WITH A CONTROL ELECTRODE ON THE ANODE SIDE OF THE DRIFT SPACE





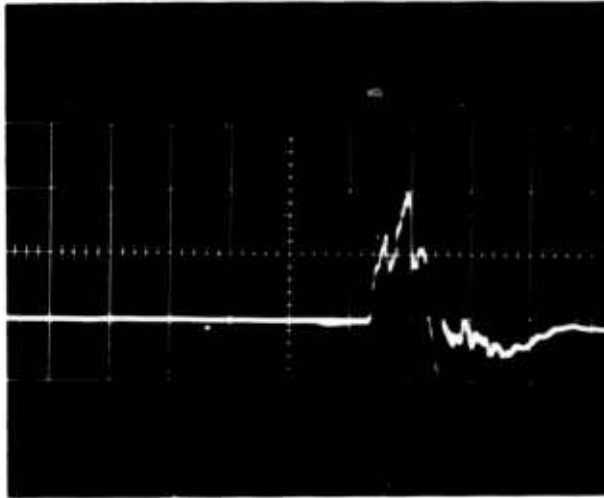
Photograph showing oscillograms of the input RF pulse and the control voltage pulse for the SFD-209.

(Time base = 1 microsecond per large division)

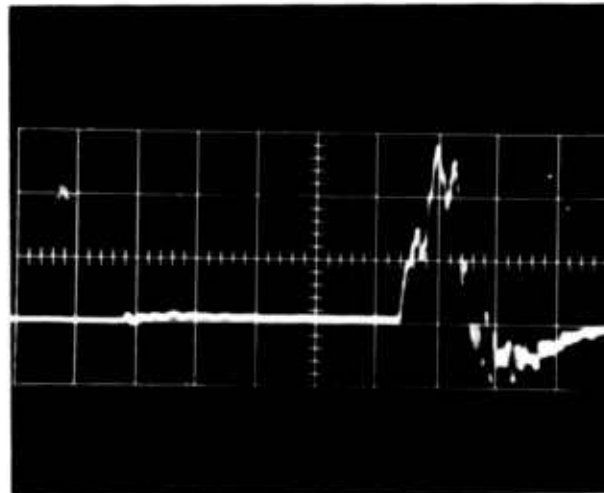


Photograph showing oscillogram of the RF output pulse.

FIGURE 23 PHOTOGRAPHS SHOWING OSCILLOGRAMS OF THE RF INPUT PULSE, CONTROL VOLTAGE PULSE AND RF OUTPUT PULSE FOR THE SFD-209



Photograph showing oscillogram of the control electrode current pulse with no RF input. Vertical calibration is 5 amps per large division. This current is capacitive charge and discharge current.



Photograph showing oscillogram of the control electrode current pulse with the tube operating.

FIGURE 24 PHOTOGRAPHS SHOWING OSCILLOGRAMS OF THE CONTROL ELECTRODE CURRENT PULSE

We have recently found that we can obtain better characteristics in inverting transformers by winding them ourselves on ferrite cores than we can by purchasing commercial ones. We can now obtain a rise time of about 0.2 microseconds into our variable load and not have excessive oscillations as long as we use about 1500 ohms of damping resistance. Experiments are underway on somewhat improved models and details of these results along with instructions on how to wind these transformers will be given in the next report.

An alternate approach to the transformer problem is to get rid of the transformer. Two circuits now being investigated in the breadboard stage and which do not require an output pulse transformer are shown in Figures 25 and 26. In Figure 25, the output tube is a high vacuum tetrode incorporated into what is known as a "bootstrap circuit". The secondary of the interstage transformer must ride up to the full output pulse voltage along with the cathode of the output tube. There must be adequate insulation between the transformer windings to make this possible and low enough capacitance so that the power dissipated in charging and discharging it is not excessive. The hard tube circuit is one that can be used when pulse groups with short time intervals between pulses in the group are used. The second modulator circuit (Figure 26) now under test uses a thyatron which cannot recover in the interval between pulses in such groups. In other applications, however, it may be advantageous. We plan to use a circuit of this sort in our life testing because the current capability of a relatively small thyatron is such that it can handle several tubes at a time. Results of tests using these circuits will be given in the next report.

Through a study of the control voltage and control current oscillograms, an approximation of the V-I characteristics of the control electrode of the SFD-209 has been derived. This result is shown in Figure 27. In obtaining this characteristic some smoothing

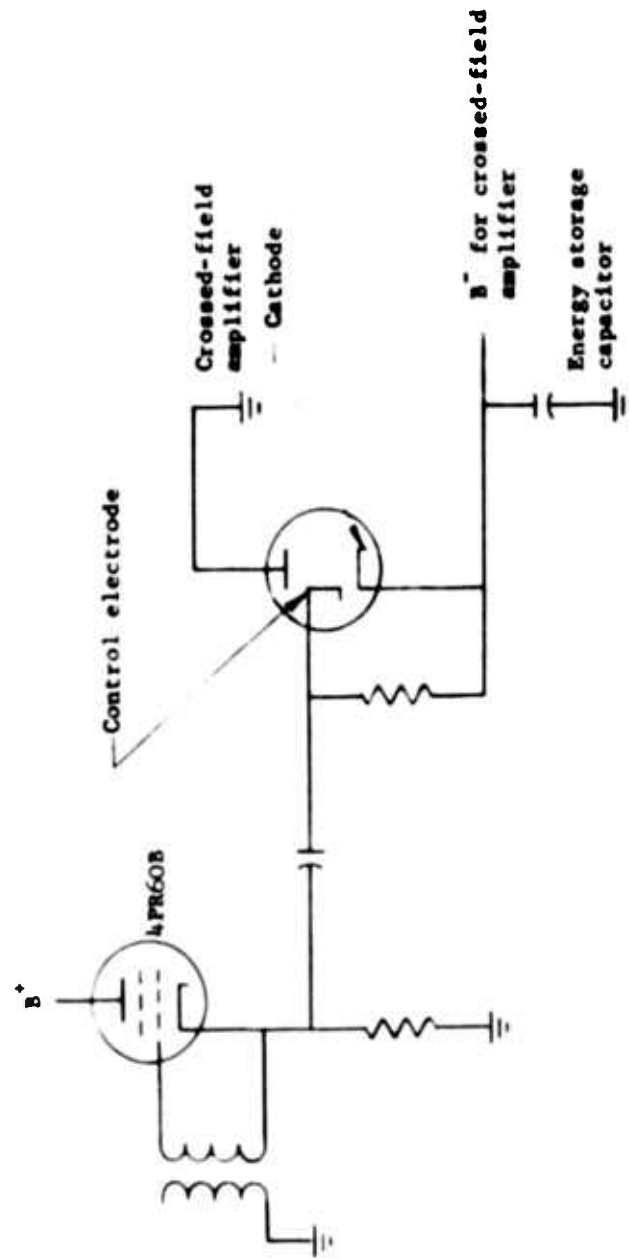


FIGURE 25 A BOOTSTRAP PULSING CIRCUIT FOR THE CONTROL ELECTRODE MODULATOR

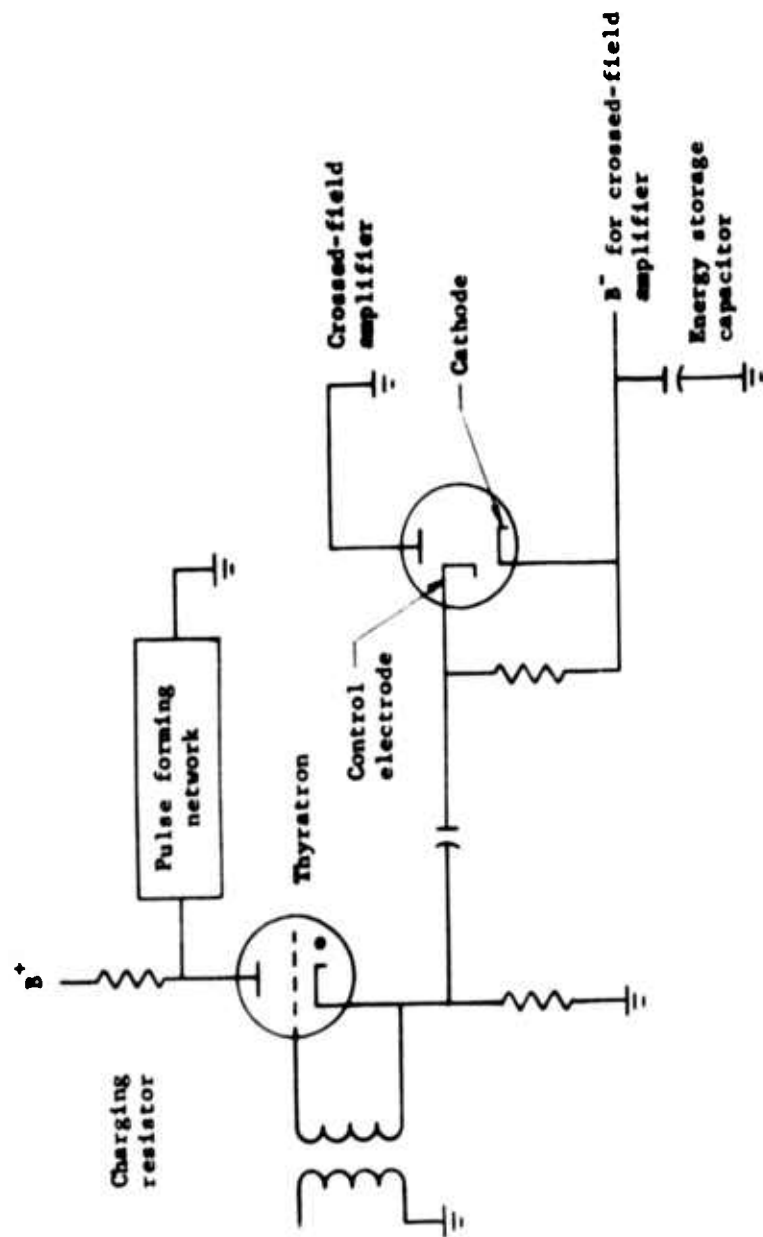


FIGURE 26 A THYATRON PULSING CIRCUIT FOR THE CONTROL ELECTRODE WHICH DOES NOT REQUIRE AN OUTPUT TRANSFORMER

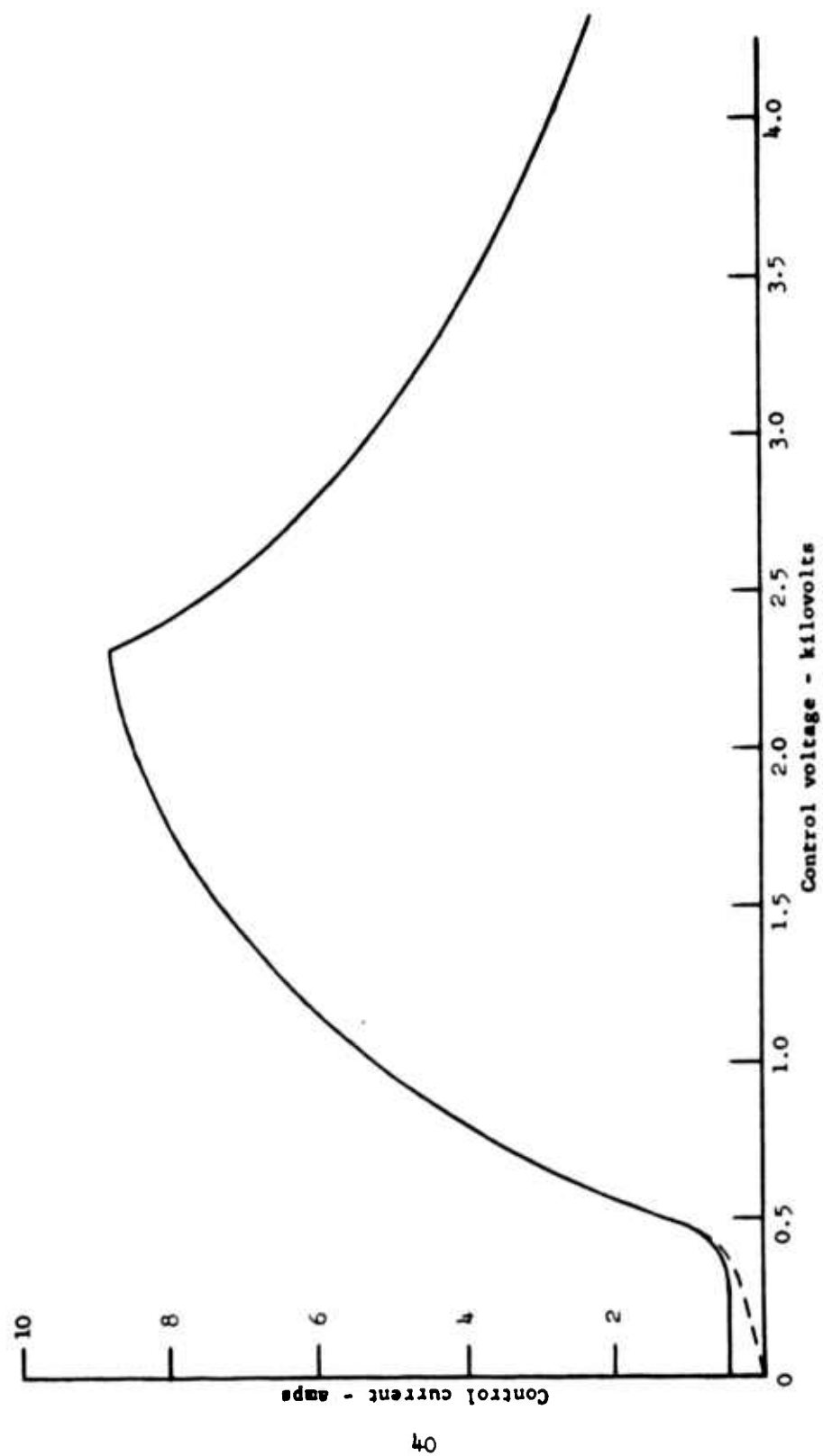


FIGURE 27 THE V-I CHARACTERISTICS OF THE CONTROL ELECTRODE

over of high frequency oscillations in the control circuit has been necessary. We feel, however, that the result shows the major features of the control electrode operation.

As indicated in Figure 27, there are three major characteristics of interest, the voltage corresponding to the maximum current, the maximum current and the minimum impedance. Once the voltage for maximum current has been exceeded, turn off will occur. If this voltage is not exceeded the control electrode will operate stably at points along the solid curve in Figure 27. (The dotted "negative resistance" region of the curve does not represent stable operation.) Thus the control modulator must be capable of reaching the turn off voltage while passing the peak control current, and it must do this in the face of the minimum impedance indicated in Figure 27. The peak current may be drawn for a very short period of time and may represent a very small average power but nevertheless the output tube must be able to pass it instantaneously. This is of particular importance when choosing a high vacuum output tube which has clearly defined peak current limitations which are dependent on the applied voltages.

The control electrode turn off procedure has been applied to the SFD-216 power tube as well as the SFD-209 driver. The approximate control electrode characteristics for the two tubes are as follows.

	<u>SFD-209</u>	<u>SFD-216</u>
Turn off voltage	2.8 kv	4.5 kv
Peak control current	10 amps	25 amps
Minimum impedance	200 ohms	200 ohms

For reliable turn off these minimum voltage and current capabilities of the modulator should be exceeded.

During the period covered by this report, an alternate control electrode arrangement was also tried in the SFD-209. In this experiment the control electrode was placed on the anode side of the

drift space and was pulsed negative toward cathode potential to turn the tube off. The control electrode consisted of the usual drift space bars but these were now insulated from ground and a connection to them was brought out of the side of the can. This arrangement and the control circuitry used are shown schematically in Figure 28. It was hoped that this control electrode would have a high impedance because electrons would be repelled from it by the negative potential and instead would be driven to neighboring sections of the anode at ground potential.

Successful control was achieved with this "positive side" control electrode but the hoped for high impedance was not observed. (This really should have been anticipated as discussed below.) Instead we observed a rather low negative resistance characteristic as shown in Figure 29. Because of the negative resistance the control voltage tended not to stay put during the "on" period of the RF pulse when the control modulator was off but tended rather to oscillate or to drift toward a negative potential so that the tube tended to turn itself off on pulses over 10 microseconds length. The only way this could be prevented was to use a very low modulator load resistance ( $R$  in Figure 28) and this, of course, made the whole circuit rather inefficient. The control pulse amplitude required with this circuit was always a little more than the dc anode-to-cathode voltage.

A useful result of this experiment (and as a matter of fact the original purpose of the experiment before we decided to try pulsing the anode segment) was a measure of the amount of current drawn to the anode surface in the drift space. This was less than one peak ampere under all conditions. This indicated that the drift space was not having an appreciable deleterious effect on efficiency.

An indication of why the negative impedance characteristic of the anode side control electrode is encountered is given by



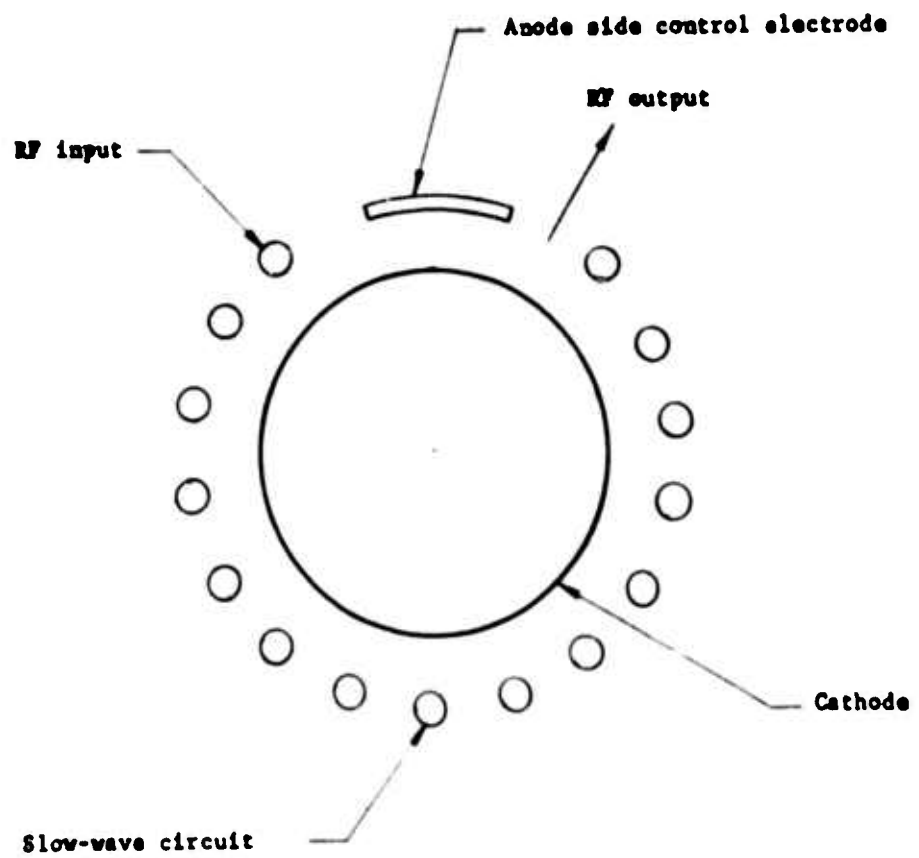


**FIGURE 28** SCHEMATIC DRAWING SHOWING THE LOCATION OF THE ANODE SIDE CONTROL ELECTRODE

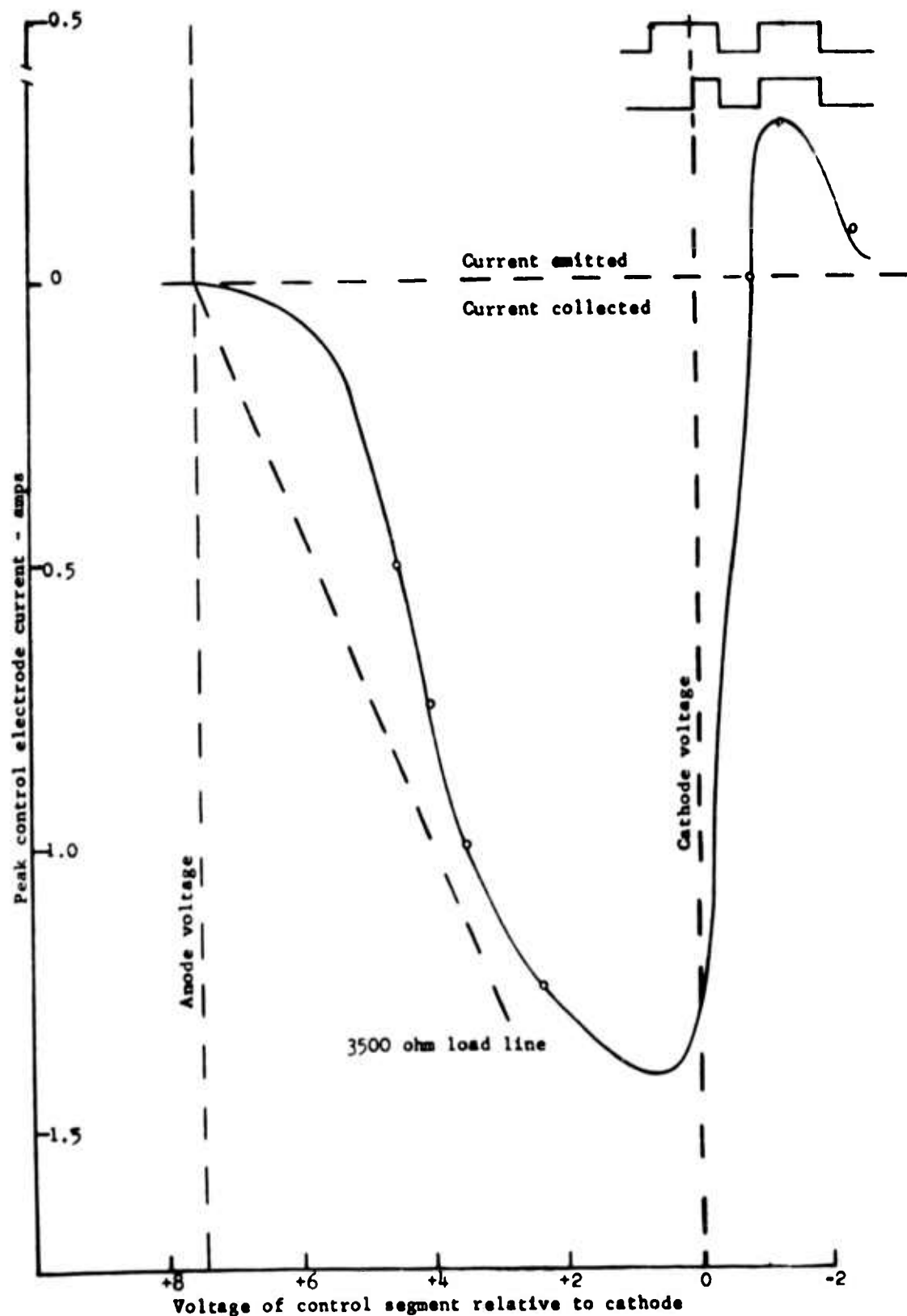


FIGURE 29 THE CONTROL ELECTRODE CURRENT CHARACTERISTIC OF THE ANODE SIDE CONTROL ELECTRODE. IF A RESISTANCE OF GREATER THAN 3500 OHMS IS CONNECTED BETWEEN THE CONTROL ELECTRODE AND GROUND THE CONTROL SEGMENT WILL BIAS ITSELF TOWARD CATHODE POTENTIAL.

Figure 29. Electrons in traversing the drift space tend to follow cycloidal trajectories centered on equipotential lines. As the drift space is pulsed negative, it intercepts equipotential lines of increasingly negative potential and, therefore, an increasing number of electrons can reach it. The more negative the voltage on the drift space anode, the more current can reach it and hence the negative resistance characteristic. The V-I curve of Figure 29 is, as a matter of fact, a rough indication of the energy (and space) distribution of the space charge flowing through the drift space.

Because of these undesirable characteristics of the anode side control electrode and because we want to maintain full freedom to design the anode side of the drift space to minimize RF leakage, we have decided to abandon the idea of the anode side control electrode.

## 2.5 Long Pulse Tests

Tests were conducted on the SFD-209 at pulse lengths of up to 600 microseconds with no signs of performance degradation. These tests were conducted by operating the tube as a self-excited oscillator using an external feedback loop. The tube was triggered on by the input RF signal from the magnetron driver and then allowed to oscillate until turned off by the control voltage pulse. The maximum pulse length obtained was limited by the amount of storage capacity available.

## 2.6 Water Cooled SFD-209

Two SFD-209 tubes were constructed with hollow copper clad stainless steel anode bars through which cooling water could be passed. This is the major change required in the driver to raise its average power output to the range required for it to be considered as a final transmitter tube. These tubes were not in themselves high average

power tubes because other changes which are required in the method of cooling the cathode and the output coaxial line were not attempted at this time. One of these tubes was tested up to an average power output level of 200 watts under which condition it ran quite satisfactorily and was, in fact, cold to the touch. These tests were made with the tube operating from a dc power supply with control electrode pulsing. The two hundred watt average power level is of significance because this is the requirement for the driver tube when operated as part of the two tube package.

The construction of these water cooled tubes proceeded without difficulty. Brazes of all the anode bars to the cooling chambers were vacuum tight on the first attempt. Even though they are hollow, the copper clad stainless bars are considerably more rigid than the copper-zirconium alloy bars used previously. This is reason enough for this method of construction even when water cooled bars are not required to meet average power dissipation requirements.

One difficulty encountered with the water cooled tubes was with the RF leakage through the drift space. To cool the coaxial lines it was necessary to braze extra cooling bars along the drift space side of the coaxial lines. This in turn necessitated reducing the number of free bars in the drift space with a consequent increase in RF leakage through this region. Measures being taken to correct this will be considered in a later section.

## 2.7 Miscellaneous Experiments on the SFD-209

A number of design variations were tried in the SFD-209 with varying degrees of success. In the first of these a series of slots 2 inches long were cut in the surface of the cathode. The purpose of this slotting was to destroy the cathode surface as a ground plane, thereby enhancing the RF field near the cathode. This was tried in a

demountable tube and while the results were not completely conclusive there was evidence of improved operation at low power levels. This experiment was followed by one in which the slots were made longer by making them go over the top and bottom of the cathode cylinder in a "U" shape. Again there was evidence of improved low level performance at some frequencies. However, the presence of these long slots caused interference with the transmission and match of the slow wave circuit. As a result performance was degraded at certain frequencies. We tentatively conclude that cathode slotting may be a useful procedure if the slots are kept resonant well above the circuit pass band. Again enhancement of up to 3 db may be available by this procedure. We hope to investigate it further in the coming months.

Another experiment tried was the construction of a tube with a variable phase velocity around the slow wave circuit. The phase velocity was varied by a smooth taper in the anode bar lengths from input to output. The phase velocity was made higher at the input than the output so that for a given dc operating voltage the percentage overvoltage would be less at the input. The lower overvoltage where the RF signal is weak is believed to enhance locking of the space charge and thereby reduce the required input power. Tapering the bar length varies the  $\pi$  mode cut off frequency and shifts the whole  $\omega$ - $\beta$  curve. Estimates of the  $\omega$ - $\beta$  curves at the input and output are shown in Figure 30. This tube did not behave as expected but tended to oscillate in the regions shown in Figure 30 where one end of the circuit was propagating and the other was cut off. This was considered a rather conclusive negative result and the concept of a tapered bar length circuit has been abandoned. The concept of tapered phase velocity, however, is not invalidated by these experiments. The tapering, however, should be of the form shown in Figure 31 where the cut off frequencies at the two ends of the circuit are the same. This type of phase velocity tapering could be obtained by tapering the width or thickness of the  $C_{13}$  couplers.

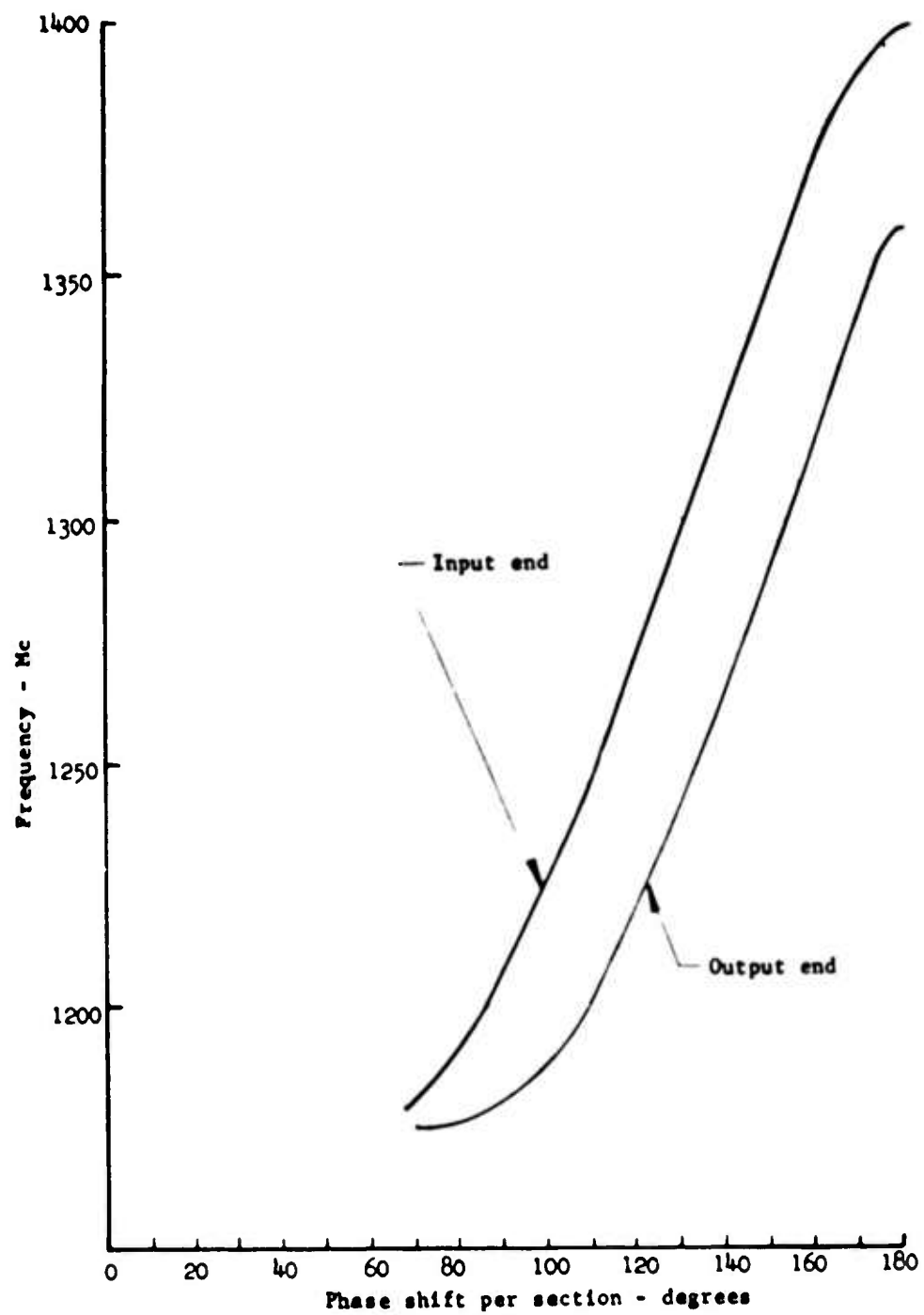


FIGURE 30  $\omega$ - $\beta$  CURVES OF TAPERED SFD-209 CIRCUIT AT THE EXTREME ENDS

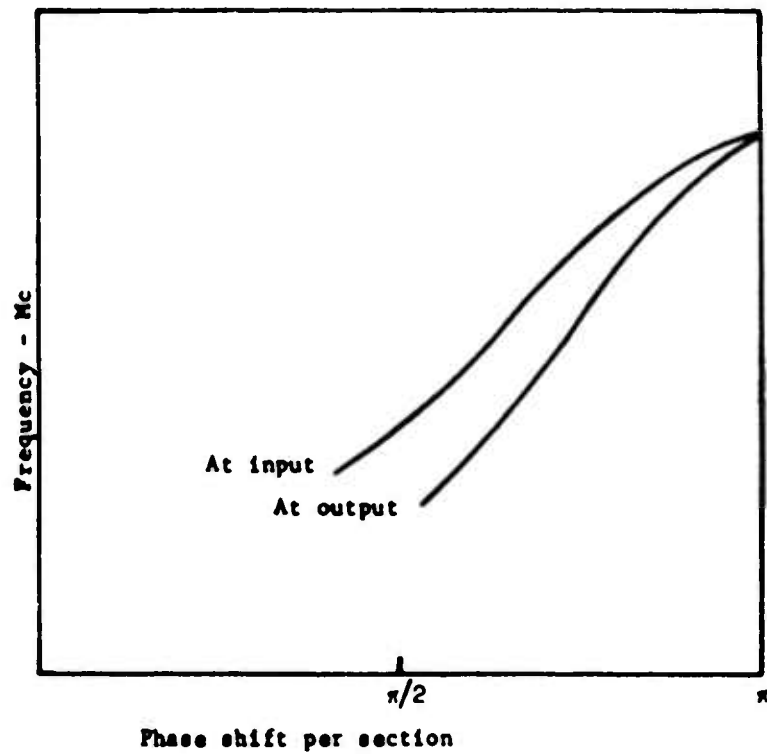


FIGURE 31 SKETCH SHOWING A FORM OF CIRCUIT TAPERING WHICH MAY BE PREFERABLE TO THAT OF FIGURE 30

Here the cut off frequency remains constant around the tube while the bandwidth is varied. This could be accomplished by varying the  $C_{13}$  coupler spacing or thickness around the circuit.

## 2.8 Experiments on the SFD-216

Effort on the SFD-216 has been carried on during the period of this report at a lower level than that on the SFD-209. This tube type has given the objective of one megawatt of peak output power. Output as a function of frequency is shown in Figure 32. These tests were taken using a line type modulator and output was limited by the modulator capability. The tube was subsequently operated from a dc power supply with control electrode pulsing at substantially the same power levels. During these tests the tube began to show some sort of breakdown phenomenon on the trailing edge of the RF pulse. This now occurs on both pulsed and dc operation. Its nature is currently under investigation.

One difficulty with the present SFD-216 design is that the band is centered at too low a frequency. Figure 33 shows an  $\omega$ - $\beta$  plot for the tube. The frequency range starting at 1150 Mc which we can reach with our driver magnetron corresponds to phase shifts per period of the circuit of over  $130^\circ$ . Experience with the SFD-209 indicates that this is close to the top edge of the band for best performance. Thus we cannot test the tube in the frequency range where performance should be optimum. This will be corrected in new tubes by shortening the anode bars.

The match to the SFD-216 circuit has been improved. Figure 34 shows transmission and return loss as functions of frequency. Adding the cathode to the tube introduces holes into the characteristic above 1200 Mc as a consequence of RF leakage through the drift space. Methods of eliminating this will be discussed in Section 4.



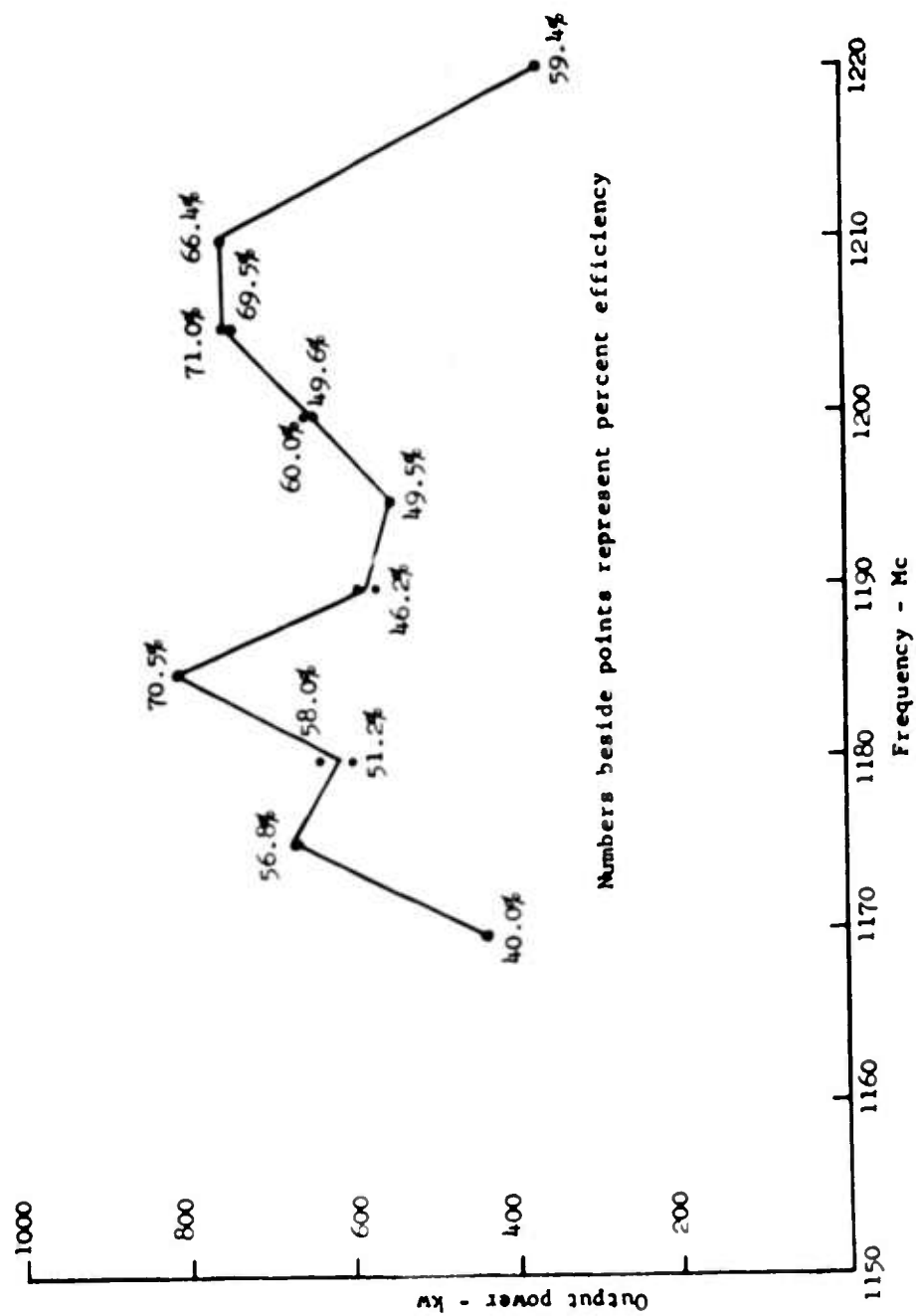


FIGURE 32 A FREQUENCY RESPONSE CURVE MEASURED ON THE SFD-216

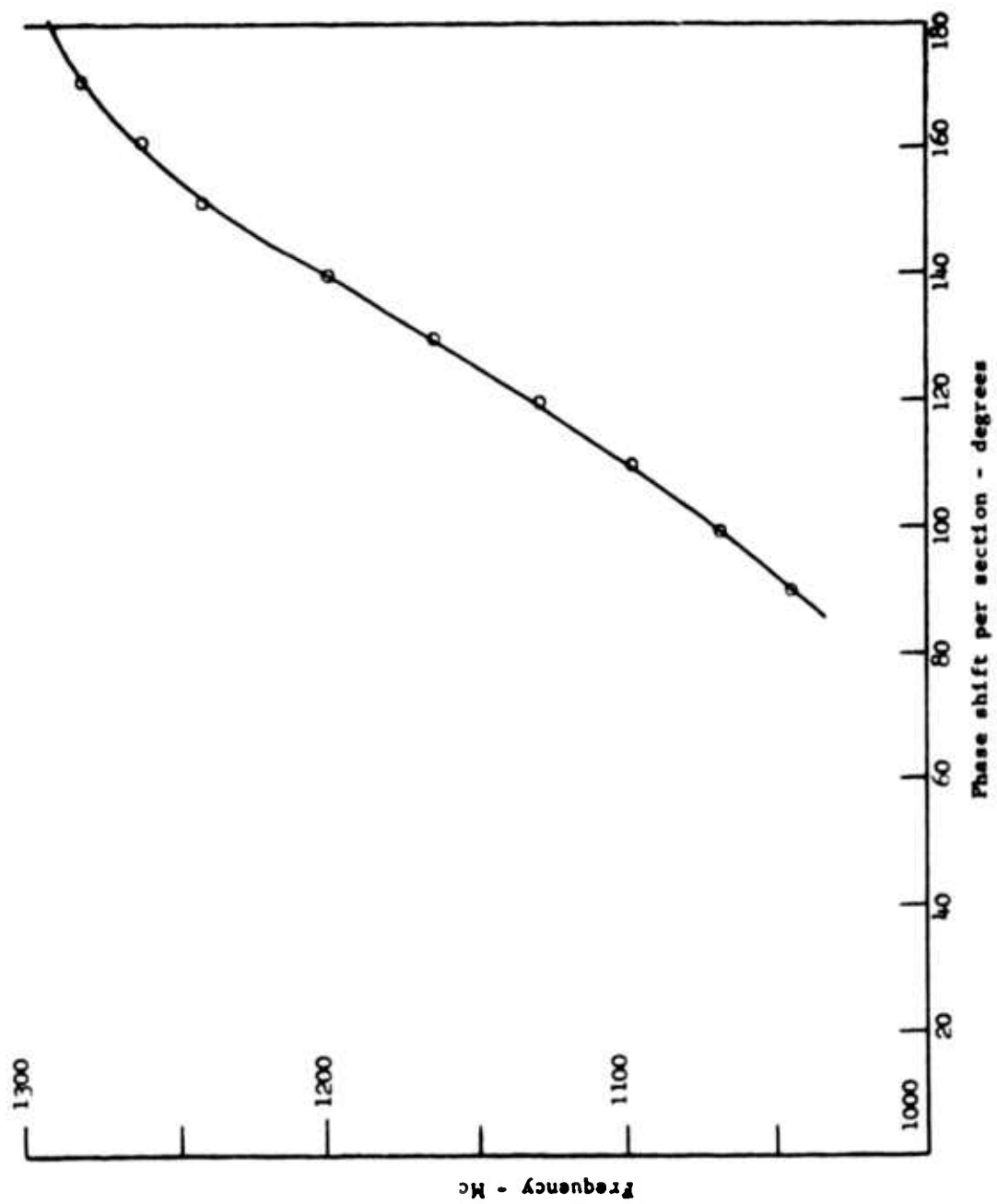


FIGURE 33 THE  $\alpha$ - $\beta$  CURVE FOR THE SFD-216

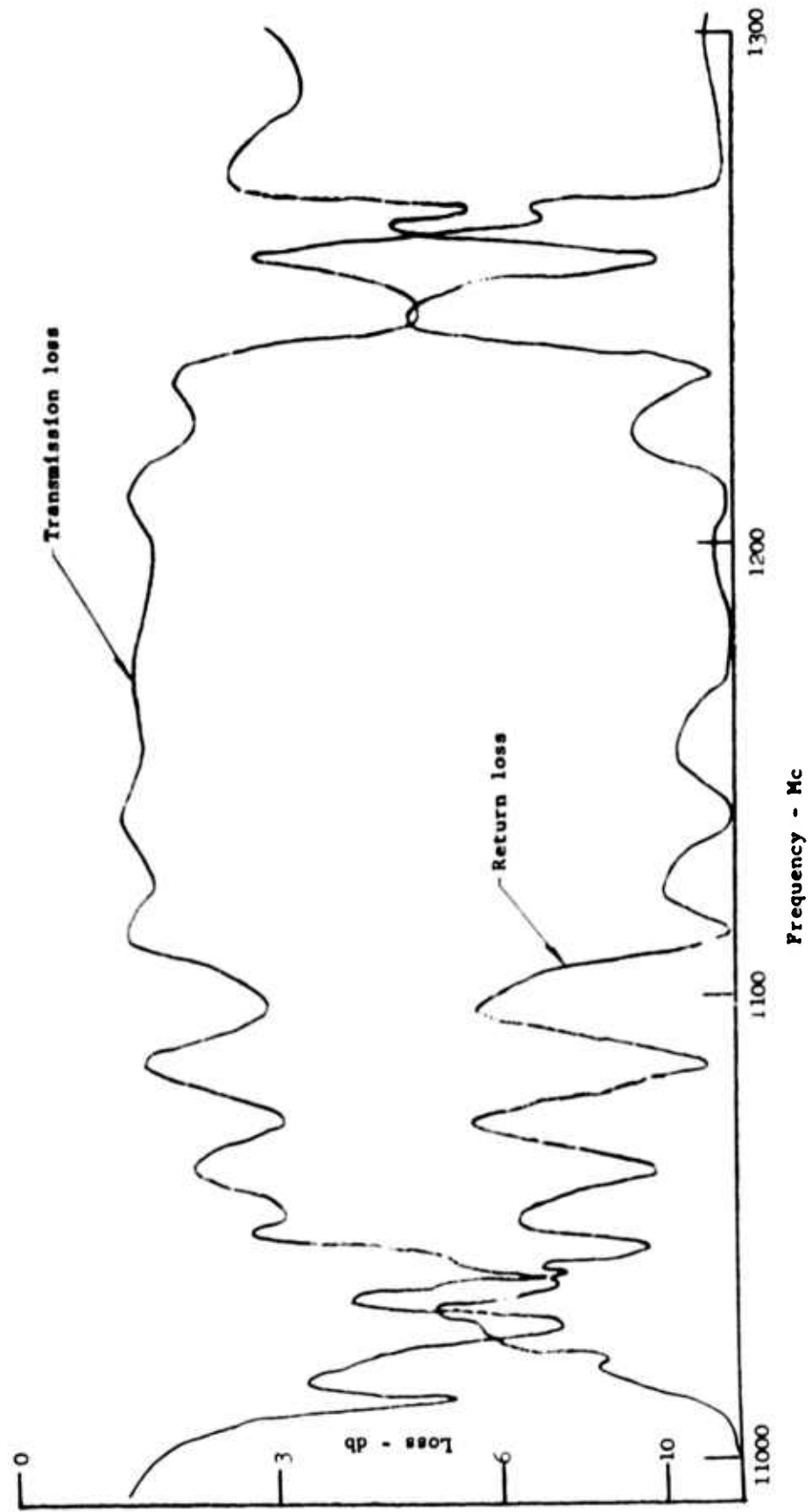


FIGURE 34 TRANSMISSION AND RETURN LOSS AS A FUNCTION OF FREQUENCY FOR THE SFD-216

### 3.0 STUDY OF MAGNETIC DESIGN AND PROBLEMS RELATED TO MOUNTING TUBES IN AN ARRAY

#### 3.1 The Requirements and Different Approaches to satisfying Them

A study was made of the various possible magnet configurations for tubes in a phased array. Features of an ideal arrangement would include:

- (1) uniformity of the magnetic field in the interaction space. Our experiences reported in Section 2.1 demonstrate the importance of this consideration
- (2) minimum interaction of neighboring tubes and minimum magnetic fields external to the array
- (3) package of tube and magnet to fit within a half-wavelength center-to-center spacing
- (4) minimum package weight
- (5) reproducibility of magnetic field from tube to tube. This is required so that all tubes may be operated from the same dc power supply.

The various magnet arrangements considered were:

- (1) shielded package in which the magnets were mounted on the ends of the tube and connected by a soft iron yoke
- (2) magnet located inside the cathode
- (3) magnet surrounding the tube and packaged with the tube
- (4) magnets fixed in the array with tubes plugged into the magnets.

Of these arrangements, numbers 2 and 3 proved to be impractical. The magnet inside the cathode could be made to give adequate magnetic field but the field uniformity in the interaction space was far short of what was desired. External magnets packaged with the tubes would result in excessive nearest neighbor effects when tube packages were changed.

A shielded package would be very desirable from the standpoint of minimizing nearest neighbor effects and external magnetic fields. It would also permit adjustment of individual magnets to the same magnetic field within a close tolerance. The method of constructing a shielded magnetic package would be to mount magnets on either end of the tube and connect them with a soft iron yoke. Unfortunately, the presence of this yoke tends to make the magnetic field in the interaction space non-uniform unless the diameter of the yoke is fairly large. Thus the magnetically shielded package tends to violate either the field uniformity or the maximum diameter requirement. It appears possible to compromise both of these requirements a bit and obtain a workable solution with this approach. This requires some significant complication in the tube design as will be discussed below.

Magnets fixed in the array and surrounding the tubes seems to represent the easiest means of obtaining a close approach to the desired objectives without compromising the tube design. The magnet weights are no more than the magnet plus yoke weight for the shielded package, and further this weight does not have to be handled each time a tube package is replaced. Replacements of tubes will have little effect on the magnets which remain fixed in place. The spacing requirements can be met without introducing field uniformity problems. The tube-to-tube reproducibility of magnetic field and the external field of the array are more serious problems than with the shielded package. However, as will be discussed below, there are ways of surmounting these problems.

A consideration of the relative merits of the shielded package and the fixed external magnets led us to the conclusion that the latter approach would be preferable. Its disadvantages are minor and it does not sacrifice tube performance. Discussions were held with magnet suppliers about the problems of the fixed magnet array.

From these discussions we came to an agreement with the Arnold Engineering Company by which they will construct a nine position demonstration magnet array module. This module should be available for testing during the summer of this year. For our laboratory tests on tubes, we are in the meantime obtaining individual cylindrical magnets which will operate a tube as an isolated entity. These magnets are fairly large since in this method of operation the magnet must supply the total external flux that would otherwise be supplied by adjacent magnets. They do, however, duplicate the conditions a tube will be in in an array.

A more detailed discussion of the various magnetic configurations will be given in the following sections.

### 3.2 The Magnetically Shielded Package

Figure 35 shows a sketch of the arrangement envisioned for a magnetically shielded package. Magnets are located on the two ends of the tube and are connected together with a soft iron yoke. It is the presence of this yoke close to the interaction space that causes non-uniformities in the magnetic field distribution.

The magnetic field distribution was studied in an electrolytic tank with the results shown in Figures 36 and 37. For the purposes of this study, the inside diameter of the yoke was taken as 4.9 inches. The central plane of symmetry of the tube and the yoke was represented by one electrode in the tank and the pole piece by a second electrode. A third electrode biased to a potential of 75% of the way from yoke to pole piece was used to represent a plane inside the magnet and thus give the solution a bit more accuracy near the magnet. An attempt was made to keep the magnet diameter as small as possible to minimize the flux leakage between magnet surface and the inside of the yoke.

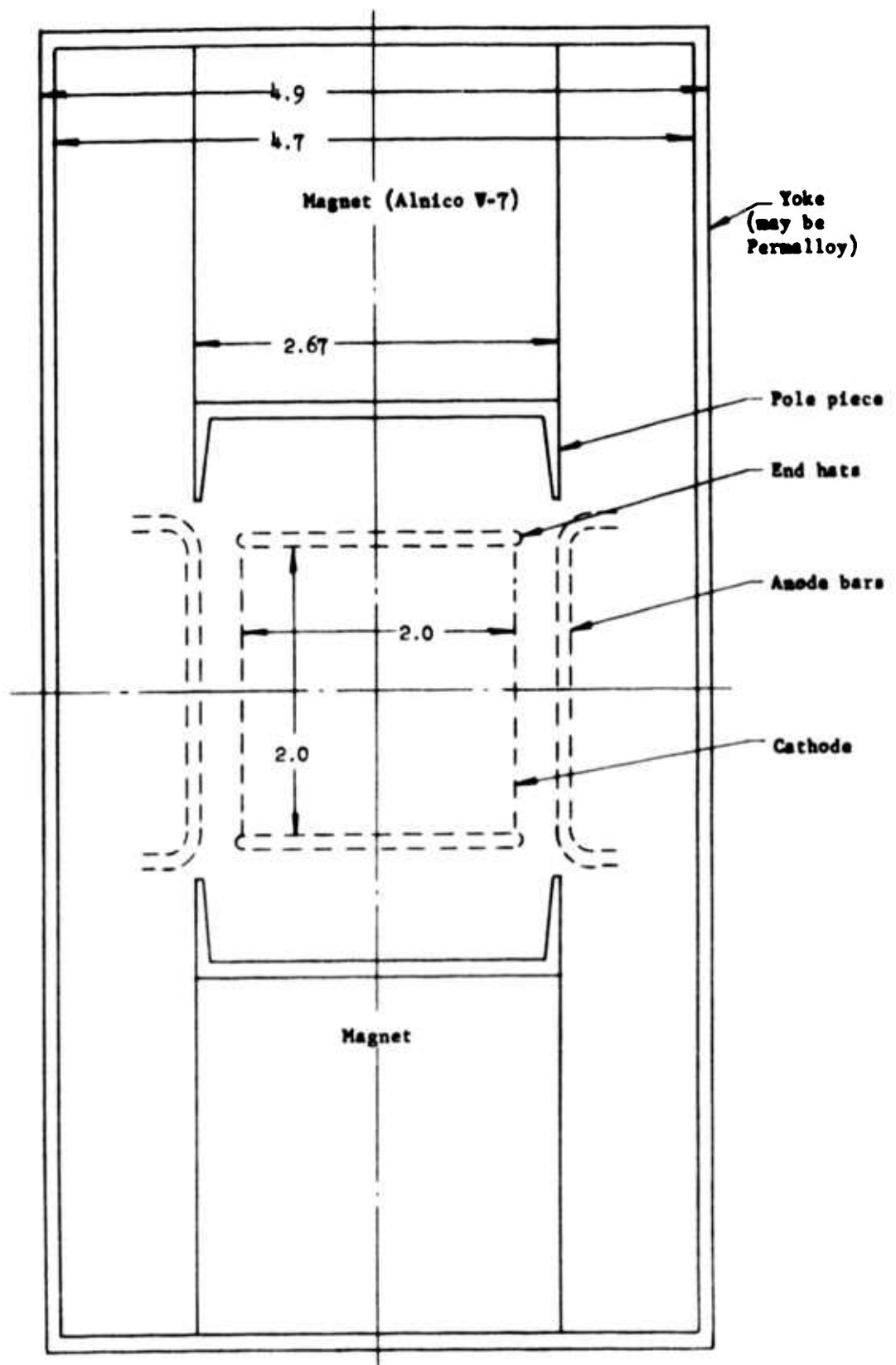
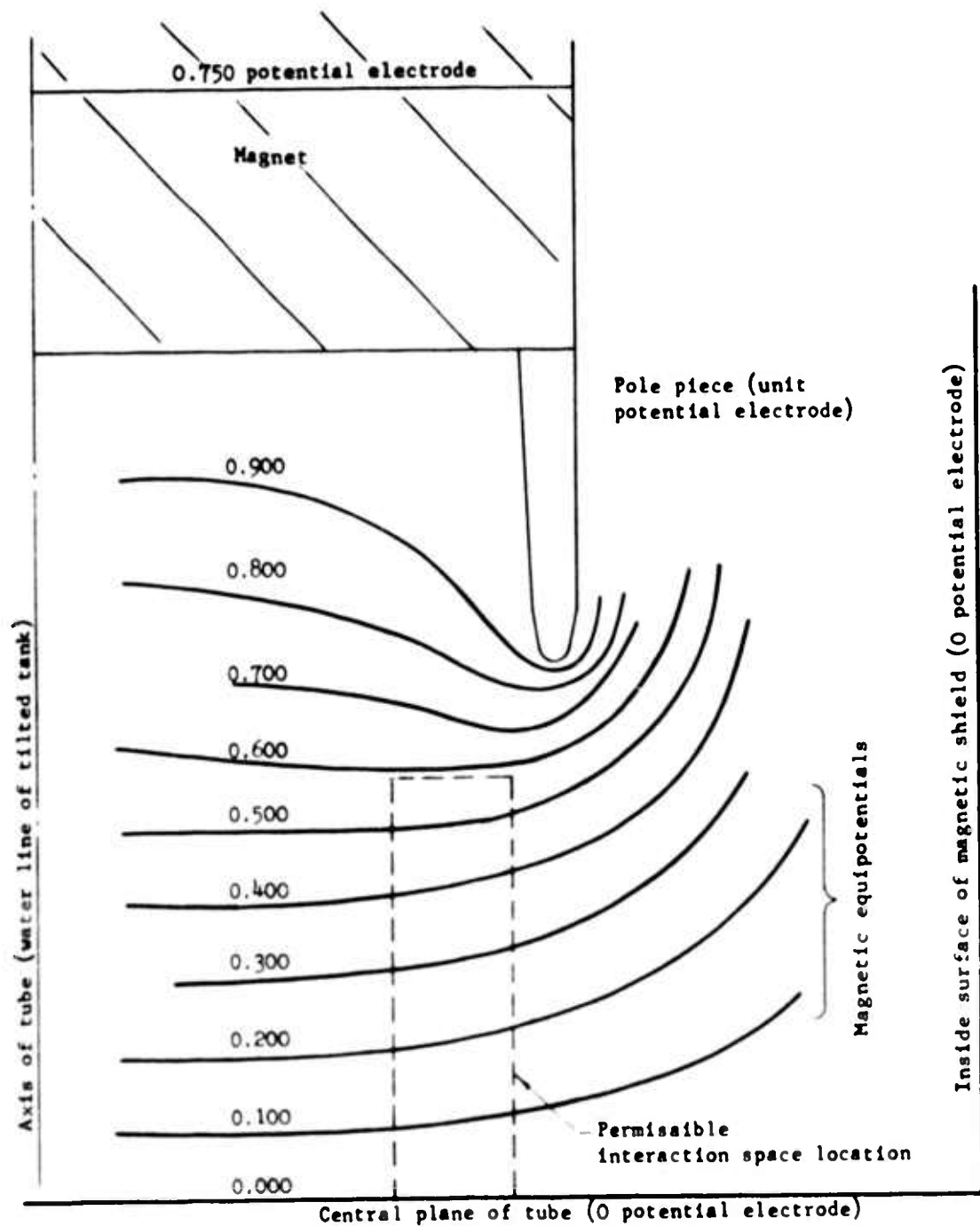


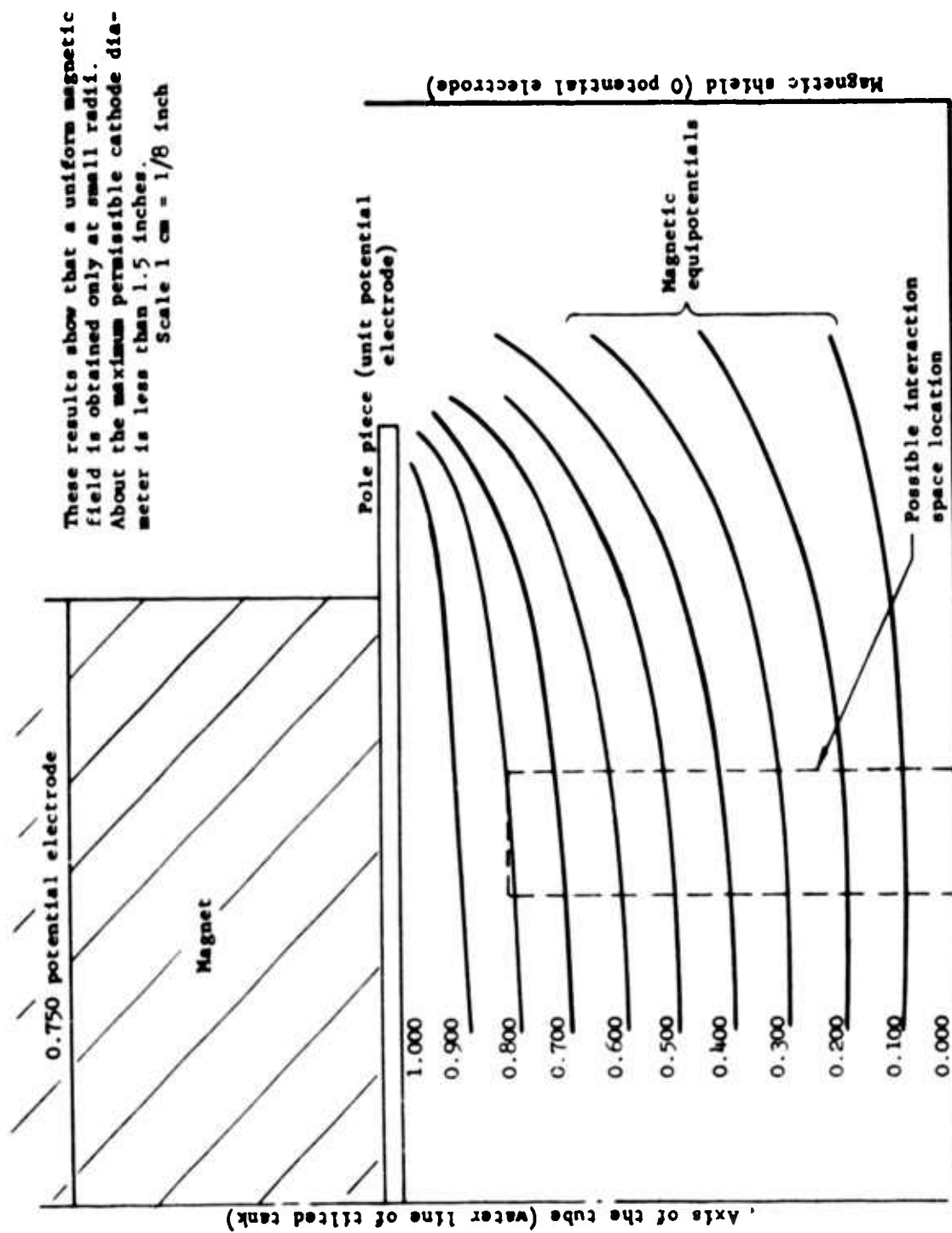
FIGURE 35 TENTATIVE MAGNETIC CIRCUIT DESIGN FOR SHIELDED PACKAGE



**FIGURE 36** ELECTROLYTIC TANK PLOT OF A TENTATIVE MAGNETIC CIRCUIT DESIGN OF THE REQUIRED TUBE

Further shaping of the pole piece may help to improve field uniformity. Scale 1 cm = 1/7 inch





These results show that a uniform magnetic field is obtained only at small radii. About the maximum permissible cathode diameter is less than 1.5 inches. Scale 1 cm = 1/8 inch

FIGURE 37 ELECTROLYTIC TANK PLOT OF A TRIAL SOLUTION FOR THE MAGNETIC CIRCUIT DESIGN OF THE REQUIRED TUBE

As may be seen from Figures 36 and 37, the presence of the yoke causes a bending of the equipotential lines since only the center equipotential can intercept the yoke which is at a potential midway between that of the pole pieces. The closer the yoke to the interaction space, the greater this bending will be. As a consequence of the bending, the flux lines which are sketched orthogonal to the equipotentials will have considerable radial components near the edges of the interaction space. The relative magnitudes of the magnetic field are indicated by the relative spacing of the flux lines. The bending of the flux lines also tends to increase the axial variation of the magnetic field. In theory we could minimize the axial variation by making the gap long and using only the central portion of it. This, however, increases the magnet length and with it the total leakage flux from the side of the magnet to the yoke. We must be careful not to raise the total flux through the magnet too far or the magnet diameter will become too large for the yoke size chosen. This tends to be a "run away" phenomenon because an increase in the total flux requires an increase in the magnet diameter which brings the magnet wall closer to the yoke wall. This in turn requires a further increase in the total flux through the magnet, etc. Thus we must be careful that the gap length we choose is consistent with what may be obtained with magnets of available materials.

Figure 36 shows the equipotential and flux line distribution when a simple pole piece was used. As may be seen, adequate magnetic field uniformity is obtained only out to about a 1.5 inch diameter whereas we need an interaction space mean diameter of about 2.5 inches to have sufficient power generating area.

Figure 37 shows a method of improving the situation through the use of permendur pole pieces protruding from the magnet. This solution represents one of the best found after a number of trials.

It gives the best field uniformity at a point just inside the pole piece diameter. In the solution shown the interaction space becomes about 2-1/2 inches in mean diameter by 2 inches long, just slightly smaller than in the SFD-209. The axial field variation over this two inches is about 10% and the radial field variation about 15%. Although these values are larger than we would like, they may be tolerable. Experience with coaxial magnetrons indicates that the magnetic field variations should be much less than this (of the order of 2%) to minimize frequency pushing. The same may apply to phase pushing in the amplifier so that one consequence of this design as compared to one giving a uniform field may be an increase in the sensitivity of output phase to voltage.

To use the design of Figure 37, the pole pieces must extend beyond what would normally be the anode bore diameter. This means that the anode bars must be bent as sketched in Figure 37. This is an undesirable complication in the mechanical design of the tube.

Figure 38 summarizes the permeance calculation for the configuration of Figure 37. The main gap permeance obtained is roughly comparable with that obtained by square counting on the electrolytic tank plot. As may be seen from Figure 38, the resulting magnet just fits assuming the use of Alnico V-7, the highest energy product material now available. This does not allow for a hole through the magnet for the stem which will make the design even a bit more marginal.

As may be seen from this discussion, the shielded package within array dimensions is marginal. The chances are that it would work but would make the tube more complicated and hence more expensive and would degrade performance as compared with an external magnet. The performance degradation from our experience would probably show up as lower efficiency and higher sensitivity of phase to operating voltage. These comments about the undesirability of the shielded package no longer hold if we consider an isolated tube application in which we do

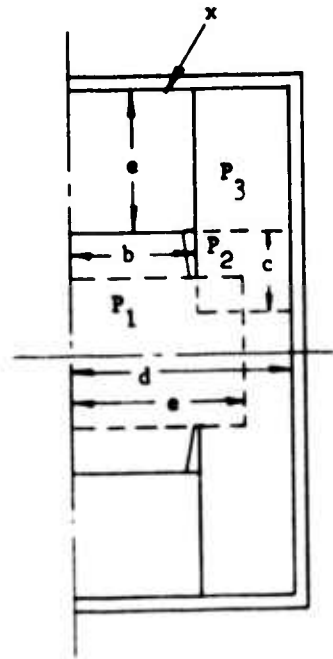
From a study of electrolytic tank plot, it is seen that permeances may be estimated by main gap permeance  $P_1$  and leakage permeances  $P_2$  and  $P_3$ .

$$P_1 = \frac{\pi e^2 B}{(\text{mmf})} ; P_2 = \frac{2\pi c}{n \frac{d}{b}} ; P_3 = \frac{2\pi a}{n \frac{d}{b}}$$

Problem is to find maximum flux density in magnet which occurs at plane x. The full mmf acts across  $P_1$ . Half the mmf acts across  $P_2$ . The mmf across  $P_3$  varies from zero to half the mmf and thus averages to one quarter the mmf. Thus

$$\phi = (\text{mmf}) \left( P_1 + \frac{P_2}{2} + \frac{P_3}{4} \right)$$

$$B_m \text{ (at } x) = \frac{\phi}{\pi b^2} = \frac{(\text{mmf})}{b^2} \left[ \frac{e^2 B}{(\text{mmf})} + \frac{\left( c + \frac{a}{2} \right)}{n \frac{d}{b}} \right]$$



From Figures 35 and 36

$$a = 2.5 \text{ inches} \quad c = 1.2 \text{ inches} \quad e = 1.70 \text{ inches}$$

$$b = 1.34 \text{ inches} \quad d = 2.35 \text{ inches}$$

$$\text{mmf} = \frac{1000 \text{ oersted} \times 2 \text{ inches} \times 2.54 \text{ inches}}{0.6} = 8460 \text{ oersted-cm}$$

M mmf is calculated knowing that end of 2 inch long cathode lies on the 0.6 equipotential from Figure 36.

Using the above values

$$B_m = 10,000 \text{ gauss at } x.$$

FIGURE 38 PERMEANCE CALCULATION FOR SHIELDED PACKAGE DESIGN

not have a half-wavelength diameter restriction. If the yoke in the designs considered could be made about seven inches in diameter, the field uniformity problem would be greatly eased and the leakage permeance of the magnet sides much reduced. In such an application, the shielded package would probably be the best solution.

### 3.3 Magnet Inside the Cathode

Figure 39 shows the contemplated location of the magnet inside the cathode. One way of mounting the magnet here would be to seal it inside a vacuum container and place it inside the cathode during tube assembly. It could then be charged after the tube is pumped by immersing the whole tube in a charging solenoid. Another method of locating it inside the cathode would be to design the tube with a hollow center so the region inside the cathode would be exposed to air and accessible from one end. The magnet could then be dropped in after the tube is pumped.

In this configuration, the magnet is in parallel with the interaction space so that the magnetic field in this space cannot exceed that in the magnet. To obtain the required 1000 oersted field an Alnico VIII magnet would be required and its length to diameter ratio would have to be about unity.

The magnetic field uniformity near such a magnet was studied with a flux meter. Figure 40 shows the actual flux plots taken near an Alnico VIII magnet of approximately the right length to diameter ratio. The fields are seen to be quite non-uniform with both considerable axial and radial variation. Because of the radial decay of field, the magnitude in the interaction space would be less than desired. Pole pieces over the ends of the magnet will help some but not enough. Because of its lower effective permeability, a ferrite magnet may be expected to give a more uniform field. Such magnets were tried but the fields were still quite non-uniform. This high degree of field non-uniformity appears to rule the magnet inside the cathode arrangement out of consideration.

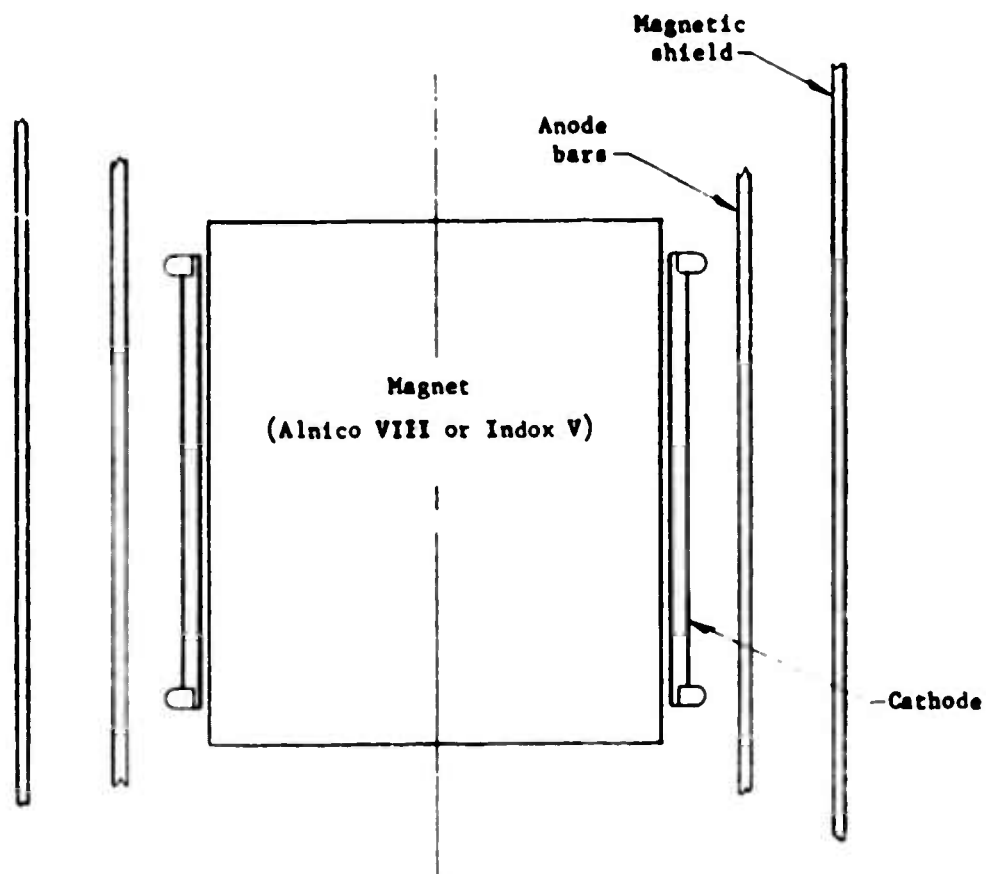


FIGURE 39 SKETCH SHOWING LOCATION OF A MAGNET INSIDE THE CATHODE WHICH WAS CONSIDERED.

This arrangement gives excessive magnetic field non-uniformity

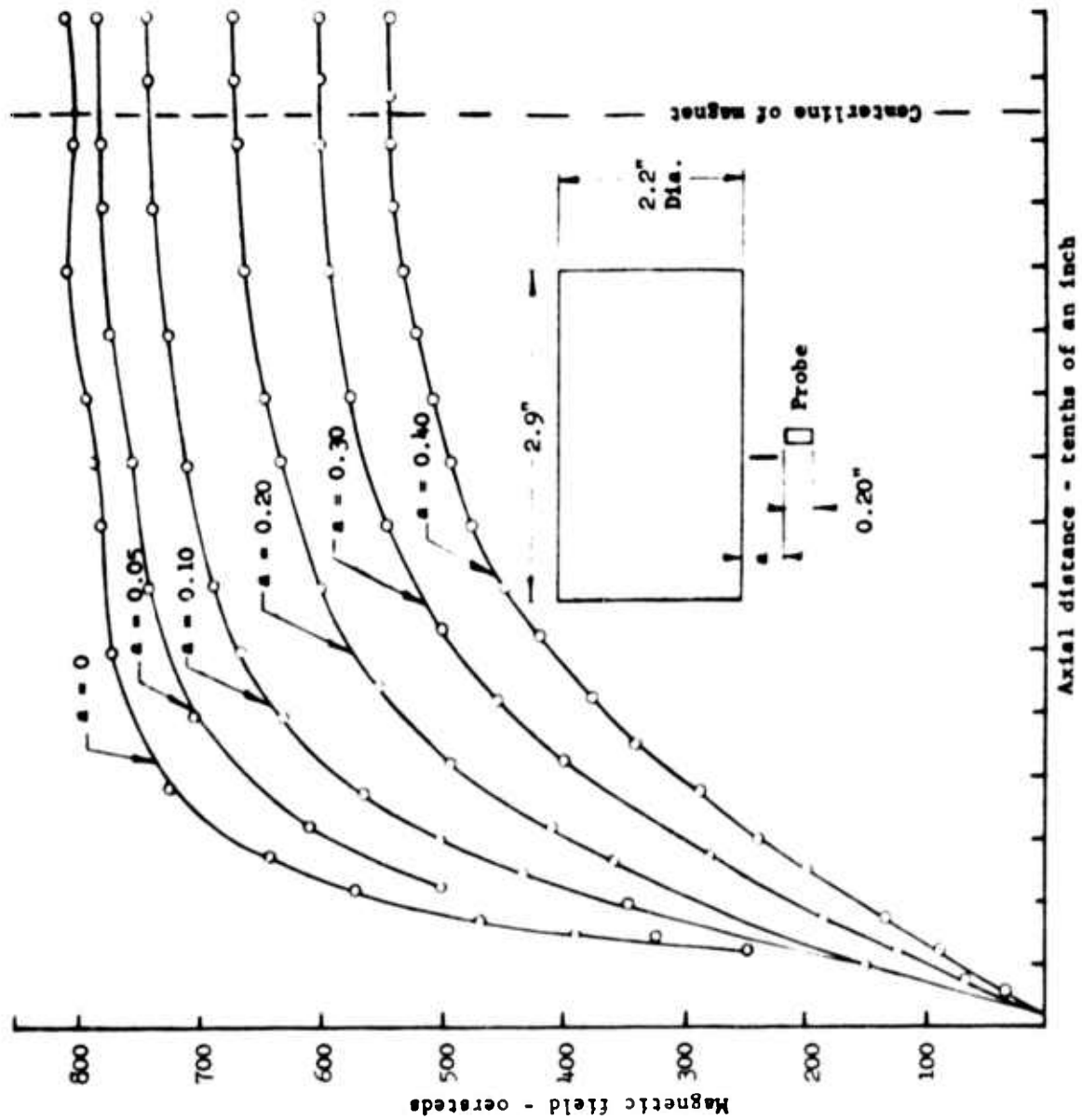


FIGURE 40 MAGNETIC FIELD INTENSITY NEAR THE SIDE OF A CYLINDRICAL ALNICO VIII MAGNET. SIMILAR VARIATIONS OF FIELD INTENSITY WERE OBTAINED WITH AN INDOX MAGNET

### 3.4 Magnets External to the Tube and Packaged with the Tube

For this arrangement, a magnet having a square external cross-section with a hole in the center for the tube would be used. Since the magnet is in parallel with the interaction space, the field in the magnet should be the same as that in the interaction space. (Use of some re-entrancy of the internal magnetic parts could have made the field in the magnet less but again this gives rise to field non-uniformity.) An Alnico VIII magnet will be required to obtain the necessary magnetic field.

In this arrangement, each magnet need supply only the total flux required for its individual cell. However if a magnet is removed from such an array, the magnets surrounding the hole must now supply the additional flux that goes through the hole. Thus their total flux is increased. For a rectangular array in which eight magnets surround the hole, we estimate that the total flux required from a magnet on the edge of the hole might increase about 10% to 15%. (The four magnets with their broad sides to the hole will encounter the maximum effect. The flux increase will be less than 25% because of the contributions of the four corner magnets and because the flux density in the hole will be less than in a tube position.) This increase in total flux will change the magnet field by about 3% to 5%. This is a relatively large change. We would like to keep the magnetic fields constant to within 1%. Under these conditions, it may be necessary to turn off four or eight adjacent tubes when replacing a tube. With this arrangement there is also the problem of whether all the magnets will come back to their original field strengths after replacement of a tube. With proper magnet stabilization this problem should be surmountable. However setting up the array in the first place might pose a bit more of a problem.



When a tube and magnet package were withdrawn from an array, the field would drop to a low value because the magnet would now have to supply the total external flux without assistance from nearest neighbors. Thus to test the tube independently, it would have to be plugged into a test position in which it would again be surrounded by other magnets. Other disadvantages of this approach arise from the extra weight the magnets add to the removable package, the magnetic forces on the packages during replacement and the problems of storing spare magnetized packages. This approach thus seems to have all the problems of magnets fixed in the array plus a number of additional ones. We thus feel that it has nothing to offer compared to the fixed magnet approach.

### 3.5 Magnets in a Fixed Array

Figure 41 shows the configuration for magnets fixed in an array worked out with the help of P. P. Cioffi of the Arnold Engineering Company. Equality of magnetic field from cell to cell is assured by using common pole pieces for all the magnets. These pole pieces may be thin because they need only carry the flux for a single cell plus the small amount of flux flowing between cells because of inequality in the magnets from cell to cell. To further minimize the field differences from cell to cell, a soft iron flux guide will surround each tube. The flux guide will in turn be surrounded by a non-magnetic spacer and then the magnet. The magnets will be 4.5 inches square and the cells 4.75 inches square so that there will be some space between magnets for additional supports, cooling liquid pipes, etc. The magnets will be cast of Alnico VIII of improved quality - i.e., of higher energy product than usually shown in the literature for this material. It is predicted that with the means of equalizing flux between cells used here, cell to cell variation will be less than 1%.

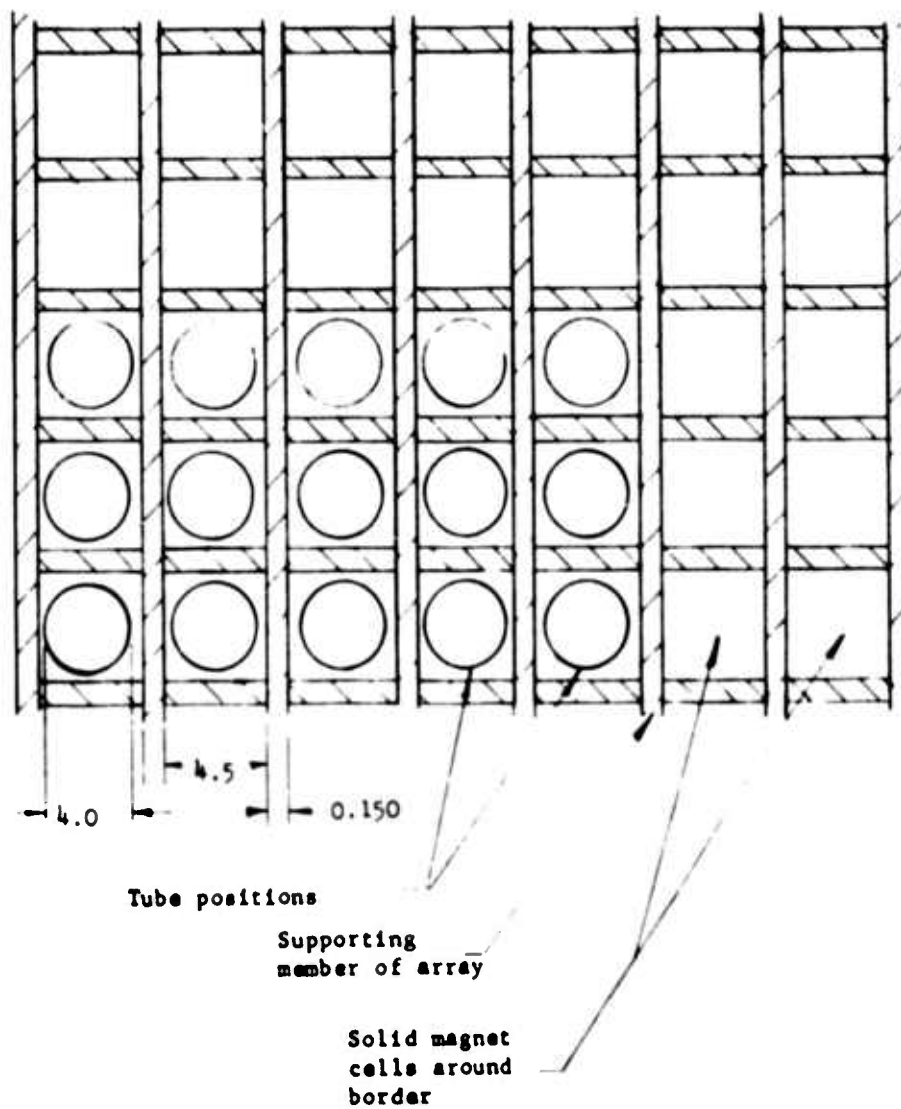


**FIGURE 41 SKETCH OF AN ARRAY OF FIXED PERMANENT MAGNETS INTO WHICH TUBES MAY BE INSERTED**

Around the edges of the array a number of dummy cells will be placed. These will provide a border of magnetic material to provide the external flux from the edges of the array. The first row of tube cells will thus see the same conditions surrounding them as are seen by the cells in the center of the array.

Some thought has been given to how the array might be assembled. The best procedure appears to be to construct it in modules of nine or more tubes. These modules would be magnetized at the factory and then shunted down with soft iron keepers around the outsides or in the tube positions. They could then be shipped and the array assembled with a minimum of inconvenience. Once the array was assembled, keepers in the tube positions could be removed and the array allowed to come up to full strength. The pole pieces of the modules would mate in lap joints to provide a low impedance magnetic path.

The external magnetic field of an array of this sort is important because if excessive it can severely interfere with other electronic equipment nearby. If an array of 30 or 40 tubes on a side could be approximated by an ellipsoid, its ratio of thickness to diameter would be very small and as a consequence, the magnetic material would be operating very near its coercive force and the external magnetic flux density (and, therefore, magnetic field) on either side of the ellipsoid would be very small. (The field in the material approaches the coercive force and the external flux approaches zero as the ratio of thickness to diameter approaches zero.) Near the center our actual array looks like an ellipsoid with a large number of holes punched through it. The magnetic material now supplies the flux which floods these holes. The ratio of  $B$  to  $H$  in the magnetic material assumes a value equal to the ratio of the cross-sectional area of a cell filled with non-magnetic material to that filled with permanent magnet material. (The saturated flux guide would have to be taken

into account by an equivalent area of unity permeability carrying the same total flux.) Away from the array a distance equal to one or two cell spacings, the field would again look like the ellipsoid field and would be very low.

What we have said so far holds for the field near the center of a large array and a short distance from its face. A practical array differs from an ellipsoid in having a constant thickness rather than one which tapers toward zero near the edges. Therefore we can expect the field near the edges of the array and a short distance from its face to be larger than that for an ellipsoid. To investigate this effect, we measured the field near the top plate of the configuration shown in Figure 42 with the results also shown there. We know by analogy with the ellipsoid problem that the results will be a function of the ratio of transverse dimension ( $s$ ) to the thickness ( $t$ ). It further makes no difference in the field distribution beyond a couple of cell spacings from the array that we have used solid plates to represent the array pole faces and have provided the magnetomotive force between them by a small magnet in the center. Thus we can get information of interest about a large array from this small scale model. (The plates were about 1 ft. square.)

Figure 42 shows the distribution of magnetic field over the face of the square plates for different ratios of side length to thickness. These results show that the magnetic field drops very rapidly as we move in from the edge of the plate. Figure 43 shows the magnetic field a distance of 0.1 times the side of the plate in from the edge. This field decreases rapidly as we approach the thickness to side ratio which would be encountered in an actual array.

From Figure 43 we conclude that if we move in 0.1 of the way from the edge of an array operating with a magnetic field of 1000 oersteds in the tube positions, the field near the array face will be less than 10 oersteds. Thus we arrive at a recipe for

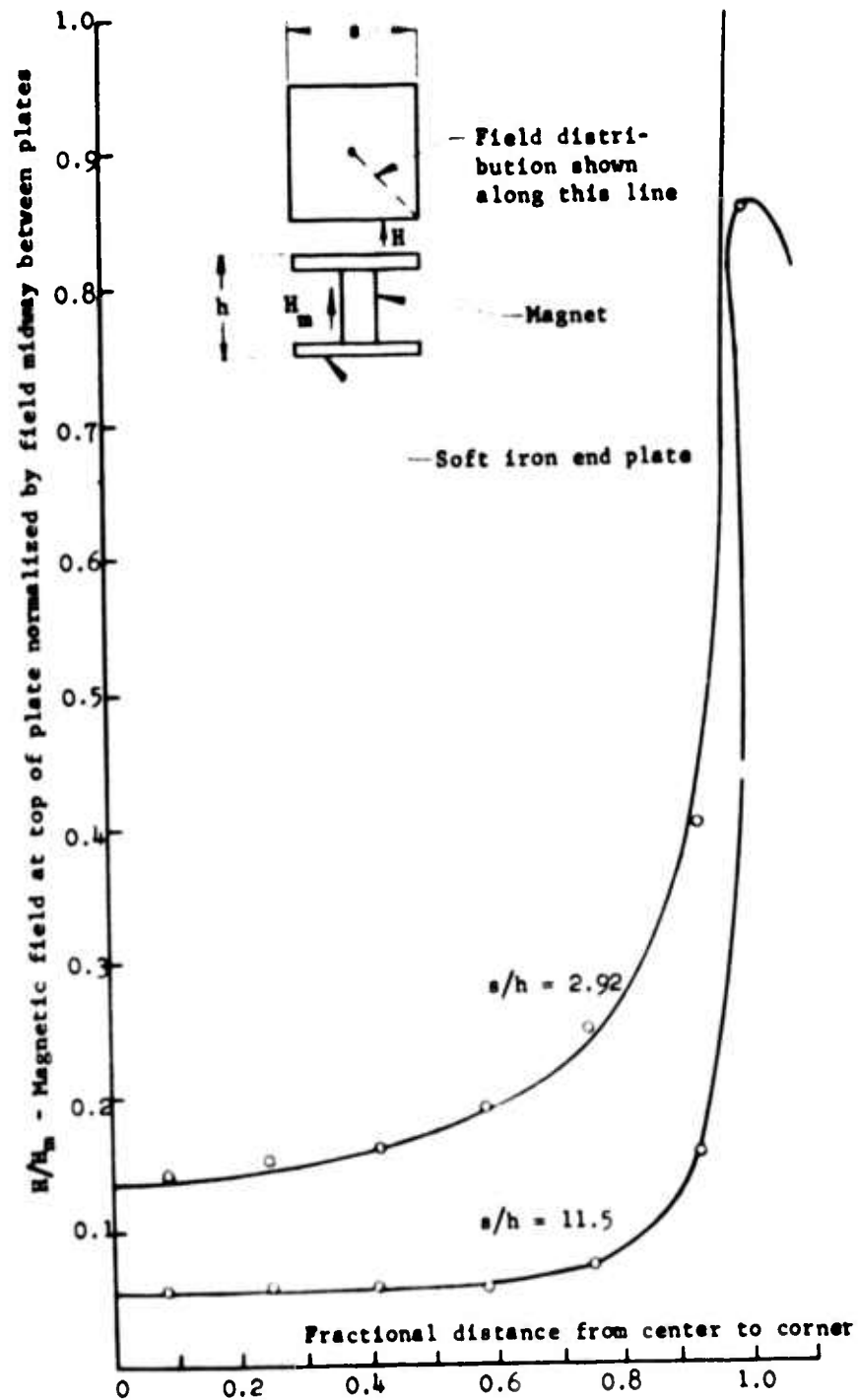


FIGURE 42 DISTRIBUTION OF MAGNETIC FIELD FROM CENTER TO CORNER OF POLE FACES FOR A MAGNET BETWEEN LARGE SOFT IRON POLE FACES.

The pole faces simulate the end pole faces of an array and the magnet simulates the MMF between these pole faces. This experiment shows how the magnetic field near the pole faces drops to a low value near the center. For an actual array, the  $s/h$  ratio would be of the order of 100.

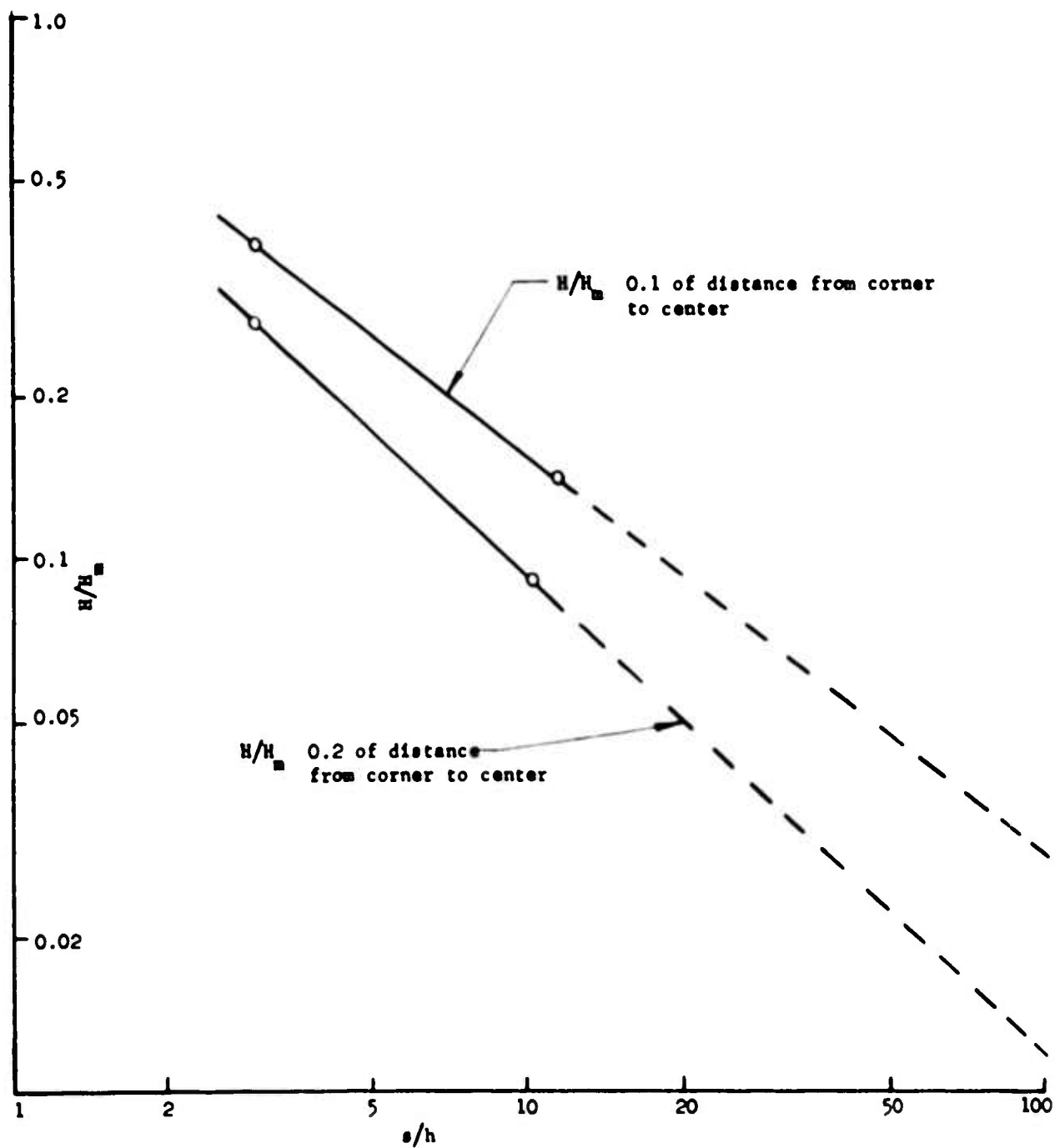


FIGURE 43 RATIO  $H/H_0$  FROM FIGURE 42 AS A FUNCTION OF THE RATIO  $s/h$

Dotted portions of the curve show extrapolation to large  $s/h$  or thin flat structures which would be used in a phased array.

insuring that electronic equipment behind the array will not be disturbed by stray magnetic fields. We simply plan to make the active part of our array take up only 80% of the side of the full magnet array. Fields behind this active part of the array where we want to place driver tubes, control modulators, etc. will then be very small. Large leakage fields will be confined to the region around the edge of the array that we can conveniently stay away from. What this means in a practical array may be a 12 ft. x 12 ft. active array surrounded by an 18 inch border of permanent magnetic material. (To provide adequate protection to the first row of tube positions from the field uniformity standpoint, this border may have had to be only 8 inches wide.) The 18 inch border could be tapered in thickness to further reduce the external leakage flux. Thus the only region of high leakage flux from the array would be this border - perhaps 18 inches wide by two feet thick running around the edge of the array.

This approach to the magnetic design of an array meets all our objectives. Field uniformity is excellent. Total weight is no greater than by other approaches and much of the weight is fixed in the array and does not have to be handled when a tube is replaced. The tubes fit within the desired spacing and external field is low, at least in the region where it is of significance. We have thus assumed this type of array construction in our tube design. The Arnold Engineering Company has undertaken the construction of a nine position module plus border magnets to demonstrate the principles involved in this approach. The dimensions of this module have been chosen to be compatible with the SFD-209 when used as a final transmitter tube in an array. For a full package two magnet arrays would have to be used and the spacing would have to be slightly larger to accomodate the larger SFD-216.

### 3.6 Magnets for an Isolated Tube

The tubes being developed on this program may at some point find application in systems in which only a single tube is required. The magnetics considerations in such cases are entirely different from what they are when the tube is used in an array. In the array application, an individual cell magnet is considerably smaller than the external magnet required if a tube is to be used in an isolated tube application. The magnet for an isolated tube must supply leakage flux to a large volume of space that in an array would be occupied by other cells and other magnets. The required increase in magnet cross-section causes an attendant increase in the outside perimeter of the magnet and hence in the leakage flux. For the case of the SFD-209, the array cell magnet is about 4-1/2 inches square whereas a comparable magnet for an isolated tube application is a cylinder with an outside diameter of 8 inches. The cross-sectional area of this magnet is five times that of the array cell magnet. Less than 10% of its total flux appears on the inside of the hole, the remainder is external leakage. Such magnets have been ordered for laboratory and life testing in spite of their size because they will accurately reproduce the magnetic conditions a tube will see in an array.

For an isolated tube application, however, another approach is desirable. One possible alternative is to use a bowl or horseshoe magnet of Alnico V-7, a higher energy product but lower coercive force material than the Alnico VIII required for the array cell magnet. An even more interesting result is obtained by returning to the magnetically shielded package of Section 3.2. By placing the magnets on the ends of the tube, their diameter is reduced by a considerable factor. Further the Alnico V-7 magnets can be used to advantage here. The result is a reduction in weight from the 50 lbs. required for the 8 inch diameter Alnico VIII magnet to 10 lbs. total for the two end magnets of the



shielded package. Putting on a 7 inch diameter return yoke adds another 15 lbs. The total weight of the magnetically shielded package including the tube thus becomes about 40 lbs. as compared to 65 lbs. with the external Alnico VIII magnet. The consideration that has made the magnetically shielded package practical in this case is the relaxation of the diameter requirement. Because of this, the return yoke can be moved far enough from the interaction space so that it does not interfere with the magnetic field uniformity there.

Another interesting solution to the isolated tube problem is to use a magnet geometry similar to that in the shielded package but to leave the return yoke off and make the magnet a bit larger to compensate for the mmf drop of the return path through space. This might reduce the package weight to 25 or 30 lbs. though this would be done at the expense of introducing considerable external magnetic field.

#### 4.0 REVISED TUBE DESIGNS

As a result of the experiments conducted during the period of this report, both the SFD-209 and the SFD-216 were redesigned. The objectives of the redesign were to

- (1) center the frequency band around that of our test equipment
- (2) reduce the electronic feedback to at least 40 db down in the SFD-209 and at least 30 db down in the SFD-216
- (3) reduce the RF leakage through the drift space to these same levels
- (4) increase the average power level by removing the limitations imposed by the cathode and the coaxial lines
- (5) increase the SFD-209 driver bandwidth.

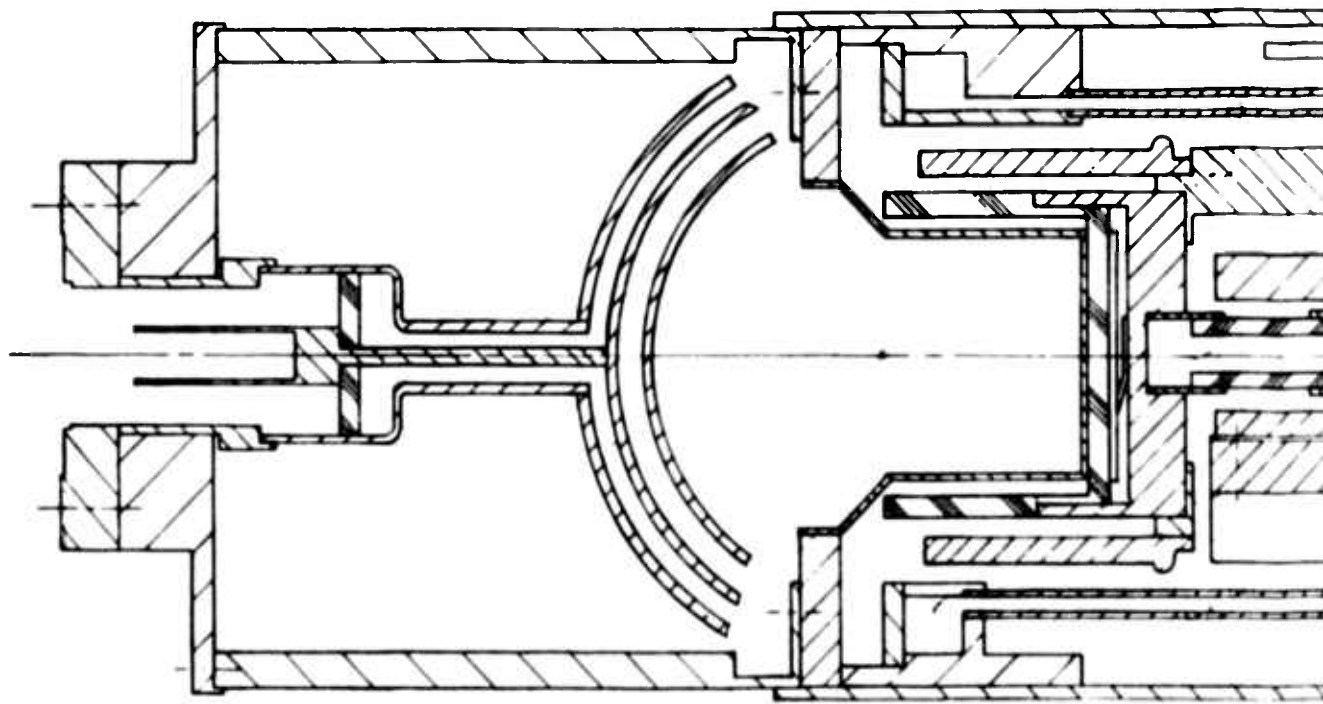
The new designs are referred to as the "B" designs. Tubes of both types incorporating these design changes are now under construction.

Centering the frequency band is a relatively simple process of adjusting the bar length. Increasing the bandwidth of the SFD-209 is also a relatively simple process. An increase in the  $C_{13}$  coupling is called for. Since the coupler slots are about as small as we want to make them, this increase is being obtained by increasing the thickness (radial dimension) of the couplers. At the same time this requires a slight increase in can diameter. Although the bandwidth increase means an impedance decrease, there is a compensating gain from working over a more restricted range of phase shift per circuit section so that the highest frequency used will correspond to a lower phase shift per section than in the original design.

A reduction in the electronic feedback in the driver is being attempted by making the drift space two periods longer and the slow wave circuit two periods shorter. A reduction in the RF leakage

through the drift space in both these tubes is being attempted by making the drift space bars longer than the main slow wave circuit bars. The attempt here is to make the drift space into a cut off filter and at the same time to prevent energy from going around the tops and bottoms of the drift space bars.

Several means of cooling the cathode have been considered. Running cooling fluid directly in contact with the cathode which is at high negative potential is undesirable in a phased array tube because then an insulating coolant is required. This would either mean circulating oil through the cathode probably by an entirely separate cooling system from that required for the anode or it would mean incorporating extensive deionizing equipment into a system using a mixture of water and other constituents. The first B design SFD-209 will use an air cooled cathode assembly. In this arrangement, a heavy shank will be brought out from the cathode and cooling fins will be attached to this shank. Figure 44 shows a layout of an SFD-209 with this type of cooling. In the long run, this air cooling is undesirable since the use of cooling air in a phased array is not anticipated. Thus we want to eventually dissipate the heat produced by cathode back bombardment by the same cooling system used for the anode. A method that will be used in the second B design SFD-209 will be to coat end shields connected to either end of the cathode with a high emissivity material. These end shields will then radiate to the anode water cooling chamber whose inside surface will be similarly coated. With such cooling the cathode may run as hot as  $450^{\circ}\text{C}$  for 200 watts dissipated but there should be no objection to this. The layout of Figure 44 shows one end of the cathode supported by a centering insulator which is in turn supported from a can, one side of which is exposed to air. In another cooling method to be tried, this centering ceramic will be replaced by a ceramic brazed both to the end of the cathode and to the vacuum can. Cooling water



1

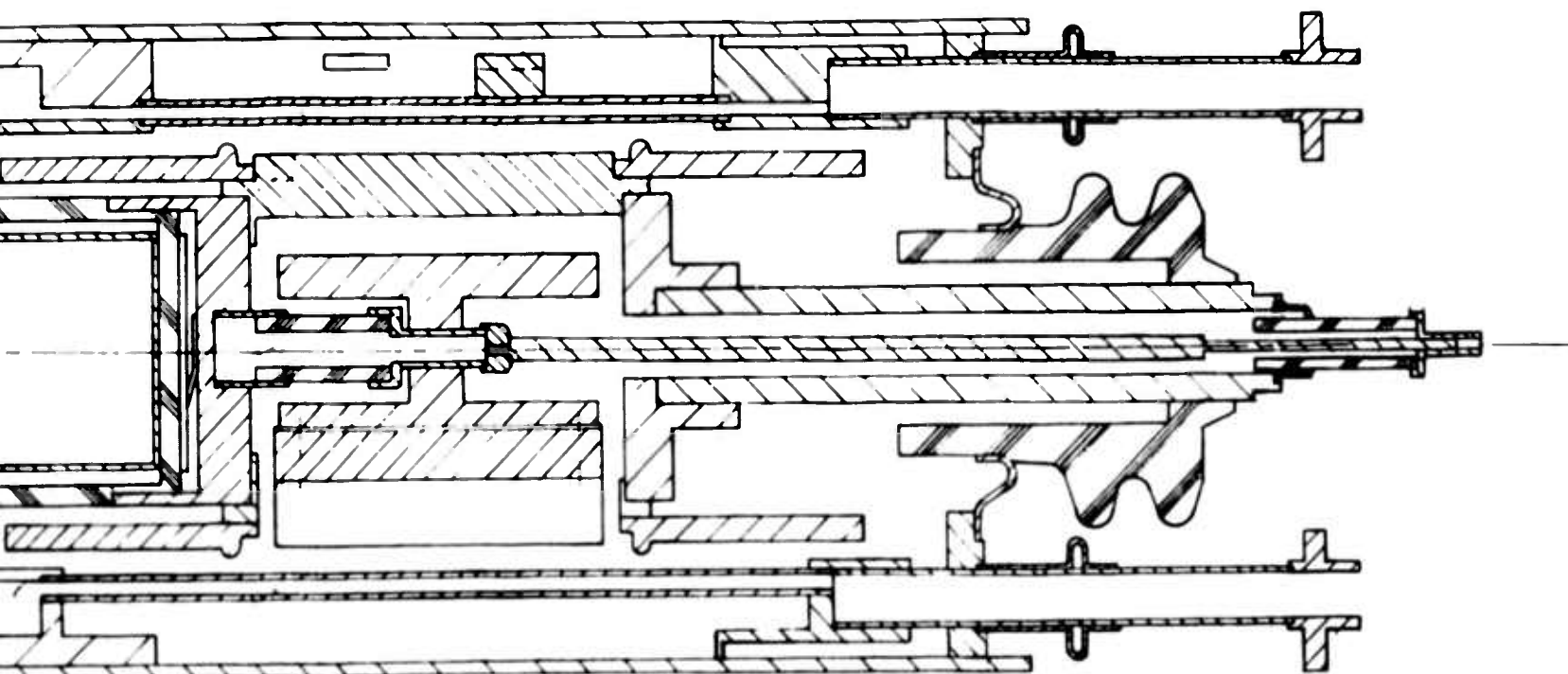


**FIGURE 44**    **REVISED VERSION OF THE SFD-209**

This view shows a section through the  
circuit bars and drift space.

will then be run on the air side of this joint as indicated in Figure 44. This should permit cathode operation at a very low temperature. Consideration was given to a pressure contact to a ceramic wafer metallized on both sides and trapped between the end of the cathode and the vacuum envelope. This would have eliminated the need for brazing the ceramic on both sides. Tests were run to determine the thermal impedance of such a joint. The best we were able to obtain was about  $1^{\circ}$  to  $2^{\circ}\text{C}$  per watt per square inch with about 25 lbs. per square inch of applied pressure, this being the order of magnitude we could contemplate using in a tube. For 200 watts of power dissipated, the cathode would run at about  $400^{\circ}\text{C}$  with such cooling. This is not much lower than can be obtained with radiative cooling so this idea has been abandoned.

The output coaxial lines of both SFD-209 and SFD-216 have been redesigned for liquid cooling. Solid copper or copper-zirconium alloy center conductors would have been thermally adequate here but the copper clad stainless tubing is more rigid and in this sense easier to work with. With these changes both SFD-209 and SFD-216 should be capable of several kilowatts of average power. The windows may now provide the average power limitation.

The tubes as now designed have rather extended coaxial line sections to get the windows centered on the tube package. It is anticipated that this section of the tube could be redesigned to considerably shorten it. This refinement will probably not be tried on this contract since the tube length is not a particularly important characteristic.

## 5.0 PLANS FOR LIFE TESTS

A life test facility for the SFD-209 and SFD-216 is in the process of construction. This facility will permit simultaneous life testing of four packages each consisting of an SFD-209 and an SFD-216 in tandem. During life testing the tubes will be operated in parallel from dc power supplies with control electrode modulation. This will permit us to gain experience with parallel operation of tubes as will be required in a phased array radar. Tubes will be mounted in individual magnets and each test position will provide for connection of an SFD-209 and SFD-216 in tandem with an isolator in between.

Figure 45 shows a block diagram of the life test facility. The input power will be provided by a 5J26 magnetron which will be run considerably below its maximum ratings to maximize its life. (Individual drivers would have been preferable but too expensive.) The output from the magnetron will be fed to the four test positions through directional couplers. Dc power for the tubes under test will be provided by two power supplies which are being purchased as S-F-D laboratories plant items from Research-Cottrell, Inc. The required isolators are being constructed on a special order by Ferrotec, Inc. The dummy loads will be Eimac water loads which will also be used for monitoring the average power. A single control electrode modulator will be used for all the drivers and another for all the power tubes. Individual storage capacitors will be used for each tube. Initial plans called for isolation of each capacitor from the high voltage buss with isolating chokes. Thus in case of an arc or short in a tube, the associated energy storage capacitor would be completely discharged and recharged without appreciably affecting the charge on the remaining capacitors. Such isolating chokes could either be iron core chokes of several henry inductance or air core chokes of much lower inductance. (They could not be low inductance iron core chokes because the high currents flowing

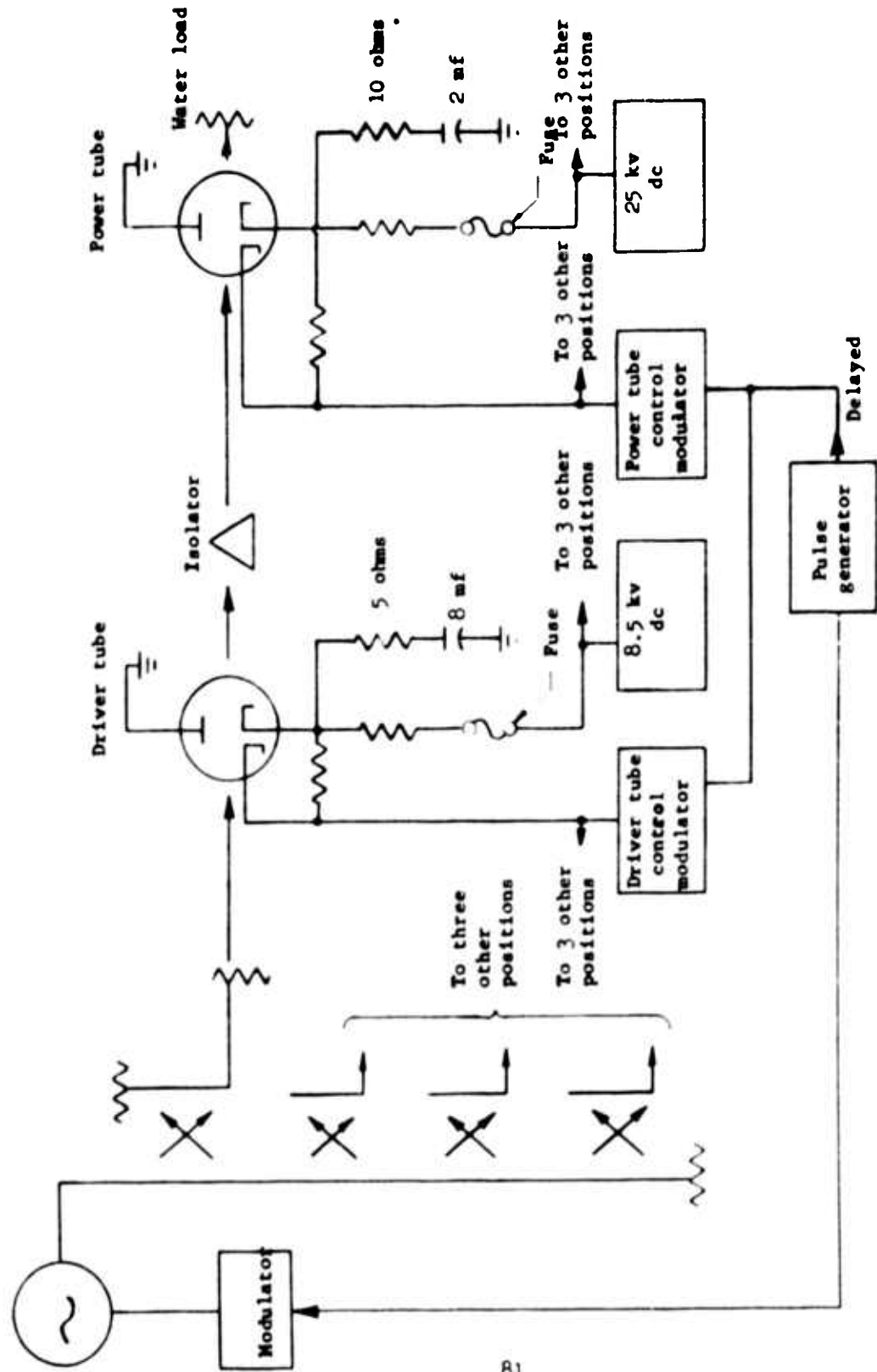


FIGURE 45 BLOCK DIAGRAM OF LIFE TEST SET UP. FOUR IDENTICAL POSITIONS WILL BE PROVIDED



in them in case of a fault would saturate the cores.) Estimates obtained on either type choke indicated that they would be rather large items and therefore undesirable as part of a phased array element. We, therefore, decided to do without the chokes and will use only an isolating resistor sized to dissipate less than 1% of the dc power and fuses which will blow in case of excessive arcing. We believe that arcing will be a sufficiently rare occurrence to make this an acceptable solution. Our life tests should provide a more complete answer about what is necessary to provide protection against occasional arcing.

All the major components for the life test facility have been placed on order and they are beginning to be received. It is anticipated that the facility will be in operation some time in June.

## 6.0 STUDIES ON THE APPLICATION OF NON-RECIPROCAL LOSS TO THE SFD-209 CIRCUIT THROUGH THE USE OF FERRITES

### 6.1 Introduction and General Summary

#### 6.1.1 Why non-reciprocal loss is desirable

Phase linearity as a function of frequency will be enhanced by virtue of unidirectional transmission through the circuit. All waves traveling from output to input will be attenuated; as a result, the ripple on the phase shift versus frequency characteristics will be reduced.

If the circuit is effectively better matched, a high gain can be tolerated before the onset of oscillations.

The gain of the tube will be allowed to be higher for a given deviation in phase linearity.

#### 6.1.2 Some of the problems to be considered

The field patterns set up by the slow wave structure have to be determined in order to properly position the ferrite.

The amount of unidirectional loss introduced by the ferrite is to be determined.

A geometry must be chosen, as well as a proper ferrite material, such as to avoid low field loss as well as the first order non-linear effect. The second order non-linear effect has to be avoided by proper choice of material and proper positioning of the ferrite. This is due to the fact that the  $h_{RF}$  fields associated with a slow wave structure are  $(c/v_g)(h_{RF})$  of a fast wave.

Also, temperature conditions are to be considered inside and in the vicinity of the ferrite. The technology will have to be developed for incorporating the ferrite into the vacuum tube; i.e., sealing, cooling.

Questions relating to chemical reduction of the ferrite in a vacuum atmosphere and the effect of heating above Curie temperature must be answered.

### 6.1.3 Short summary of progress

In order for the ferrite to function as an isolator, it must be inserted in a highly inductive region in which the RF magnetic field is circularly polarized. It will be shown that in the region in which the ferrite will be positioned, a circularly polarized RF magnetic field can exist. Furthermore, experiments performed on the slow wave structure confirm the existence of circularly polarized magnetic field.

The ferrite has to satisfy several criteria which are at times conflicting. As a result a choice of several materials is required. Only through experimentation will the most suitable and desirable material be determined.

In order for these experiments to yield meaningful results, it has been decided to build a linear version of the SFD-209 circuit. This structure will permit an accurate but variable spacing of the ferrite from the circuit.

### 6.1.4 Present status

The linear circuit is in the mechanical design stage. The ferrites for the linear circuit are on order. Consideration is being given as to how the ferrite will be incorporated into the tube; i.e., proper seal from the ferrite to the tube, removal of heat from the ferrite, coexpansion of ceramic and adjacent wall.

## 6.2 Interaction of RF Fields of the SFD-209 Structure with a Ferrite Ring

### 6.2.1 Qualitative Description of the Magnetic Field Pattern

For the slow wave structure in the tube, as a first approximation, it appears plausible that for capacitive coupling between alternate bars ( $C_{13}$ ) the currents will loop in the manner shown in Figure 46.

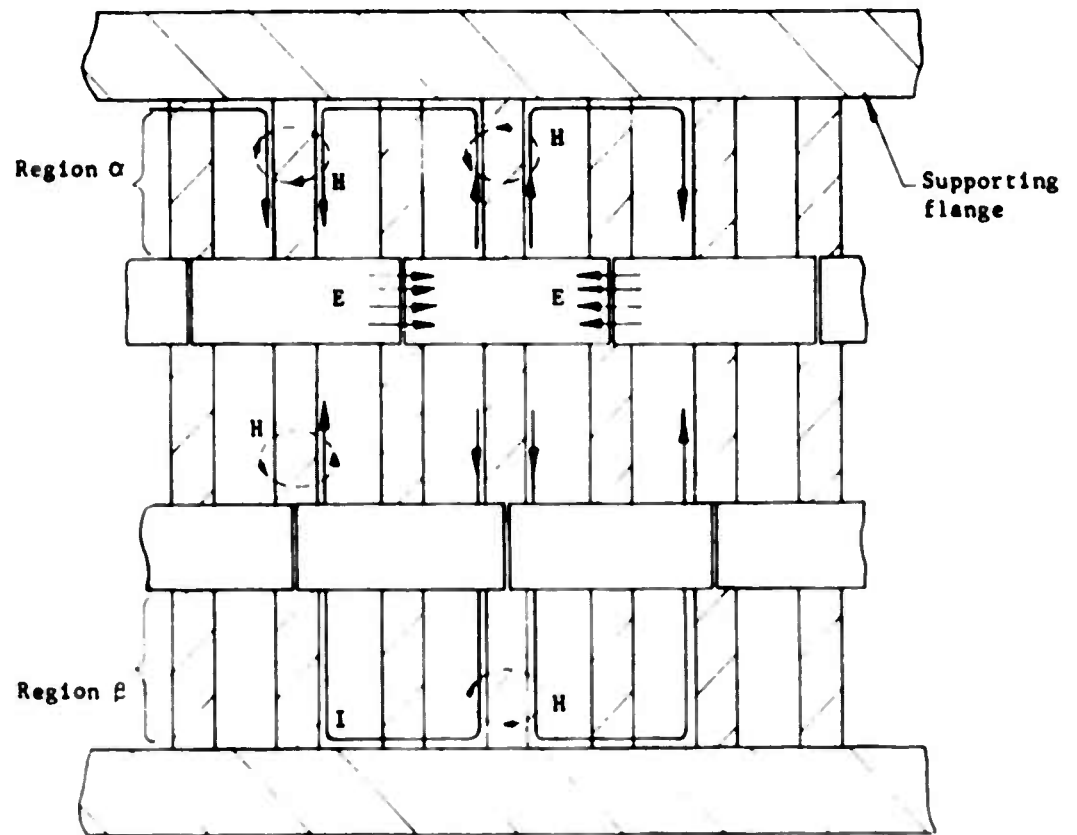


FIGURE 46 FIELD PATTERNS ASSOCIATED WITH THE SFD-209 STRUCTURE

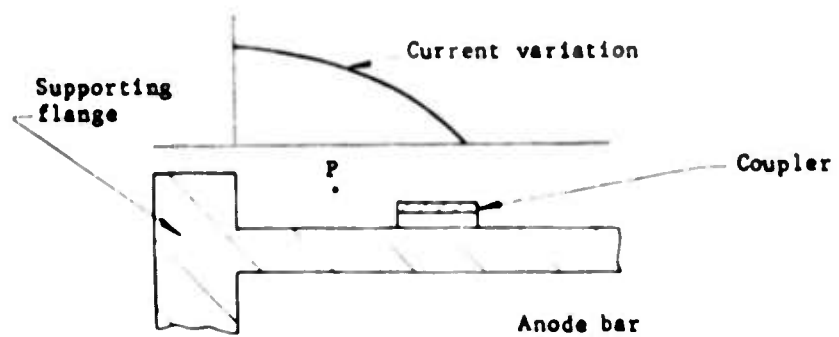


FIGURE 47 ASSOCIATED WITH THE DESCRIPTION OF FIELD PATTERNS

Now, since the H lines curl about the I lines, they will loop around the circular bars. The  $h_{RF}$  intensity, at a given radial displacement from the anode bar, will vary cosinusoidally as shown in Figure 47 having a maximum at the short-circuited end (highly inductive region) and a null at the coupler (highly capacitive region).

It appears plausible that circular polarization will exist for the  $h_{RF}$  fields in the region between the supporting flange and the coupler row from the following argument.

Consider a point P as shown in Figure 47. The configuration shown in Figure 48 assumes  $90^\circ$  phase shift between alternate bars (to be consistent with Figure 46; this choice is arbitrary). (In this case,  $h_{RF}$  fields reverse polarity on alternate bars.)

If for a stationary observer at point P of Figure 48, the  $h_{RF}$  fields are passing by at constant amplitude while completing a  $2\pi$  rotation per wavelength of wave traveling by point P, then we may conclude that the  $h_{RF}$  field is circularly polarized. From the assumed  $h_{RF}$  pattern in Figure 48, it appears that at a given position, point P, the  $h_{RF}$  field display versus time will be as shown in Figure 49.

NOTE: A study of Figure 46 will show that point P could be located either in region  $\alpha$  or  $\beta$ ; i.e., the same polarization exists in each.

However we are dealing here with a slow wave structure; i.e., there is an infinite number of  $h_{RF}$  loops each corresponding to a particular space harmonic of the structure. This slow wave behaves fundamentally as a forward wave. Associated with each space harmonic there is a phase shift per section  $\beta_m = \beta_0 + m\pi/L$ . Let us consider the fundamental and the first backward space harmonic. As will be shown later, they are waves of importance in the discussion that follows. Note that (Figure 50 explains notation)

$$\frac{\beta_{-1}}{\beta_f} = \frac{2\pi - \beta_f}{\beta_f} \quad (1)$$

This relation will be used later.

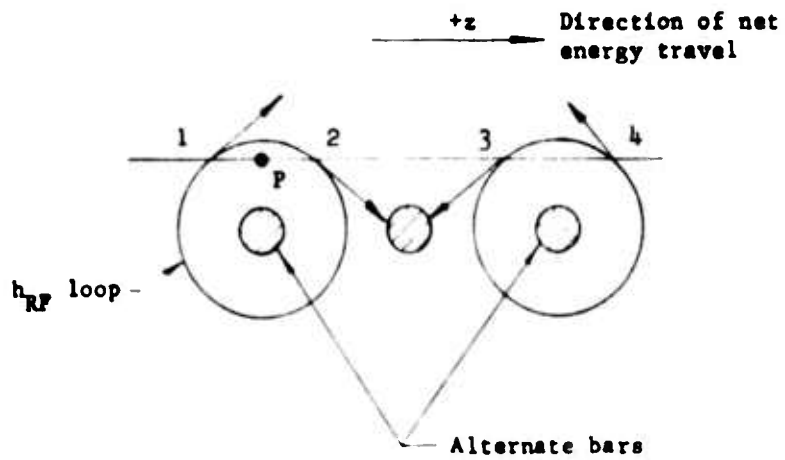


FIGURE 48 RELATING TO THE ROTATION OF THE  $h_{RF}$  MAGNETIC FIELDS IN THE VICINITY OF THE SFD-209 STRUCTURE

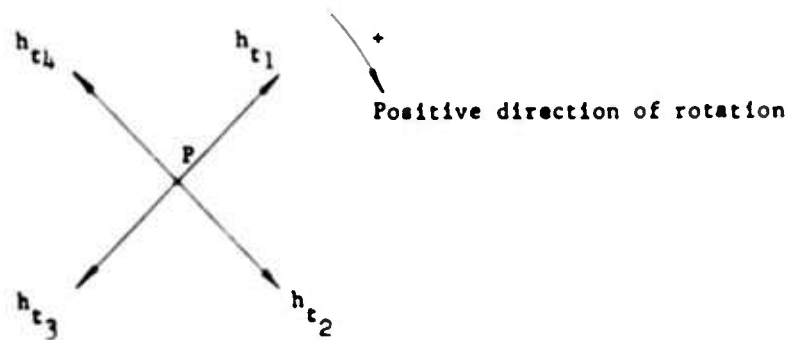
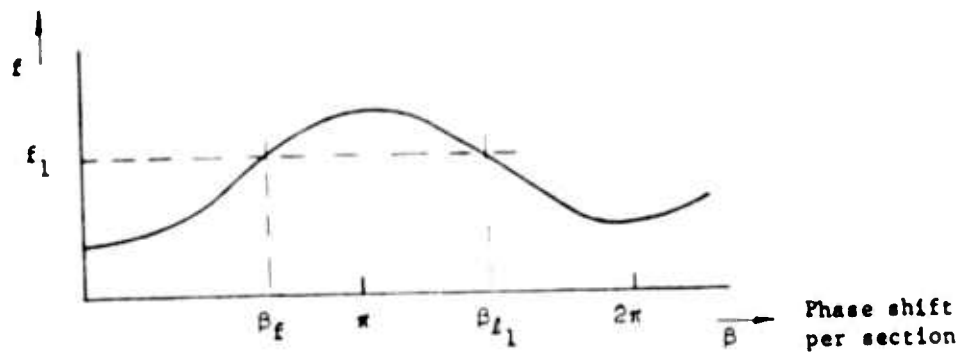


FIGURE 49 RELATING TO THE STATE OF POLARIZATION OF THE MAGNETIC FIELDS IN THE REGION CONSIDERED IN FIGURE 48

FIGURE 50  $\omega$ - $\beta$  CHARACTERISTIC OF A SLOW WAVE STRUCTURE



We also know that the slope of the  $\omega$ - $\beta$  curve equals the group velocity of the particular wave under consideration. If we consider the fundamental and the first backward wave space harmonic, we see that the former has a positive group velocity whereas the latter has a negative group velocity. Hence the energy associated with these waves travels in opposite directions.

As a result, if we assume that Figures 48 and 49 describe the polarization of the fundamental and its direction of propagation, we conclude that the direction of rotation of the first backward wave space harmonic  $h_{RF}$  field and its direction of propagation will be reversed. Thus if we have a device that absorbs waves circularly polarized in a given direction, one of the above waves will be absorbed.

Now for a slow wave structure

$$\hat{H}(x, y, z)e^{-\gamma z} = \sum_{\text{all } n} \bar{H}_n(x, y)e^{-j(\frac{2\pi}{L})z}e^{-\gamma z} \quad (\text{Ref. 1})$$

where

$$\bar{H}_n(x, y) = \frac{1}{L} \int_{z_1}^{z_1+L} \left\{ \hat{H}(x, y, z)e^{-\gamma z} \right\} e^{(\gamma + j\frac{2\pi}{L})z} dz \quad (\text{Ref. 2})$$

The above equations apply in the direction of propagation. However, in a direction normal to the direction of propagation for a slow wave, the fields vary as  $e^{j(\beta_n y)}$  if there are no losses in the system; for then  $j\beta_n = \gamma + j(2\pi/L)$ , where  $\gamma = j\beta_0$ , which yields  $\beta_n = \beta_0 + 2\pi/L$ . Then the decay rate away from the circuit (in a normal direction) is  $e^{-\beta_n y}$ .

- 
1. Dean A. Watkins, TOPICS IN ELECTROMAGNETIC THEORY, John Wiley & Sons, Inc. (1958), p. 3, Eq. 1.6
  2. Ibid., Eq. 1.9

If we write the total field expression as a summation of forward and backward waves, we get

$$H_{\text{forward}} = K_0 e^{-j\beta_0 y} + K_2 e^{-j(\beta_0 + \frac{4\pi}{L})y} + K_4 e^{-j(\beta_0 + \frac{8\pi}{L})y} + \dots \quad (2)$$

$$H_{\text{backward}} = K_1 e^{-j(\beta_0 + \frac{2\pi}{L})y} + K_3 e^{-j(\beta_0 + \frac{6\pi}{L})y} + \dots \quad (3)$$

The largest terms by far are the first term in each of the above expressions, for  $y$  "large enough". (Note that at the surface of the circuit,  $y = 0$  so that no decay has taken place.) All the terms associated with the forward wave will have, say positive polarization; all the terms associated with the backward wave will be polarized in the opposite direction.

#### 6.2.2 Ferrite Interaction with the RF Fields

From the theory of ferrites, it is known that if a ferrite sample is introduced into a region of circularly polarized magnetic field and if a dc magnetic field is applied in a direction orthogonal to the plane of  $h_{\text{RF}}$  polarization, the electromagnetic energy will be absorbed by the ferrite sample for one direction of polarization.

The  $h_{\text{RF}}$  fields corresponding to forward and backward waves are associated with positive and negative circular polarization respectively. Furthermore, for  $y$  large enough, the first term in the component fields (Eq. 2 and 3) is by far predominant. We can say that the ferrite interacts primarily with that term, either forward or backward, depending on the direction of application of the dc magnetic field, the direction of rotation of the circularly polarized field, and the direction of propagation of the wave.

For example, if the wave propagates in the  $z$ -direction while its polarization is in the  $z$ - $y$  plane, then depending on whether the dc magnetic field is applied in the  $+x$  or  $-x$  direction the ferrite



will interact with one or the other component of the wave. The energy absorbed will be proportional to

$$e^{-c_0 K_0} e^{-2\beta_0 y}$$

if we consider the absorption of the forward wave and

$$e^{-c_1 K_1} e^{-2(\beta_0 + 2\pi/L)y}$$

if we consider the absorption of the backward wave.

Consider the first component of the forward wave. The energy present in it is proportional to

$$E_f \times H_f^* \sim (e^{-\beta_0 y})(e^{-\beta_0 y}) = e^{-2\beta_0 y}$$

The attenuation introduced by the ferrite is exponential  $\alpha$  db/meter. As a result the net absorption is one of double exponential nature. A similar argument applies to the backward wave.

### 6.2.3 Quantitative Verification

An experiment was conducted which verified our interpretation of the circuit and ferrite behavior discussed above. It was found that a logarithmic plot of the attenuation, in db, introduced by the ferrite versus radial excursion from the circuit yielded a straight line for the attenuation for both directions of applied dc magnetic field. Note that the variation is linear, "far enough" away from the surface of the circuit - say above 1 mm; otherwise, the other terms in the summation of the wave become important as discussed above. This can also be seen from the plot being discussed.

We can conclude that the  $h_{RF}$  fields are uniformly circularly polarized from the following reasoning.

(a) Uniformity

The plot shows that variation of attenuation with distance is uniform; hence the same polarization exists in the whole region that was investigated. (The fields are decaying exponentially away from the circuit.)

(b) Circular polarization

Since absorption was unequal for different directions of applied magnetic field, we conclude that the field could not have been linearly polarized. Furthermore if any component of linear polarization had been present, it would have offset the two attenuation curves since the absorption would then have been a hybrid between forward wave and backward wave for each direction of applied dc magnetic field. Note that a linearly polarized wave can be broken up into two oppositely rotating circularly polarized waves.

From the slopes of the curves in Figure 51, we can calculate  $\beta$  for the circuit at a given  $\omega$ .

Example: from the graph,  $M(\text{forward}) = -2\beta_0(\text{forward})$ ;  
 $M(\text{backward}) = -2\beta_1(\text{backward})$  where  $M$  is the slope. Therefore

$$\frac{M(\text{forward})}{M(\text{backward})} = \frac{\beta(\text{forward})}{\beta(\text{backward})}$$

But from Eq. (1) in the previous discussion,

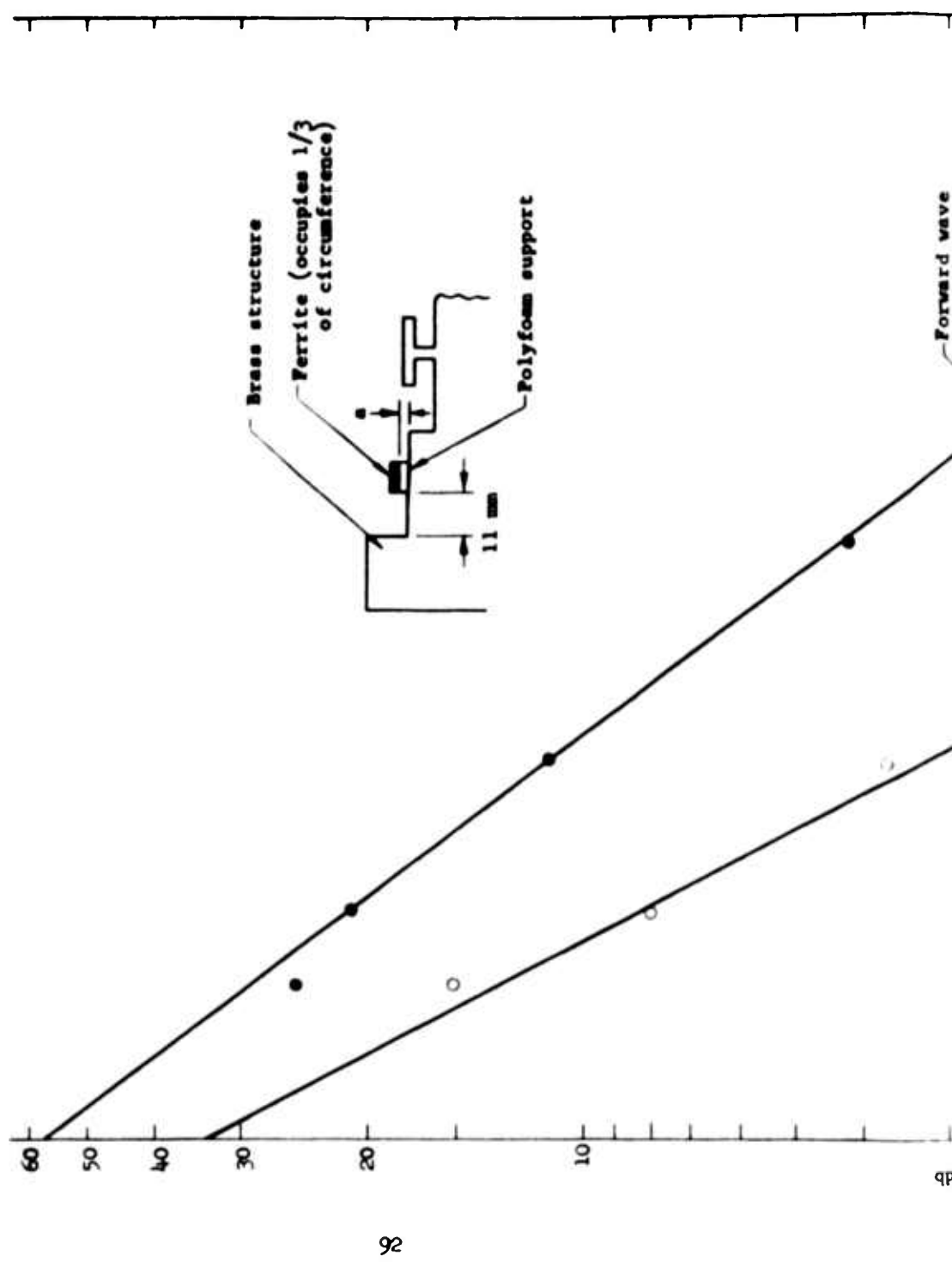
$$\frac{\beta(\text{backward})}{\beta(\text{forward})} = \frac{2\pi - \beta(\text{forward})}{\beta(\text{forward})}$$

$$\begin{aligned} M(\text{forward}) &= -1.4 \\ M(\text{backward}) &= -1.97 \end{aligned} \quad \text{from the graph}$$

then solving for  $\beta(\text{forward})$  we get  $\beta(\text{forward}) = 147^\circ/\text{section}$ . This value is close to the value of  $\beta$  obtained by standard methods at  $f = 1250 \text{ Mc}$  ( $\beta \approx 140^\circ$ ).

Thus this method might be an alternate way of finding the  $\omega$ - $\beta$  diagram of our structure. Even more important, the intercept of the attenuation curve with the axis corresponding to zero radial displacement from the circuit yields information about the relative impedances of the various wave components.

1



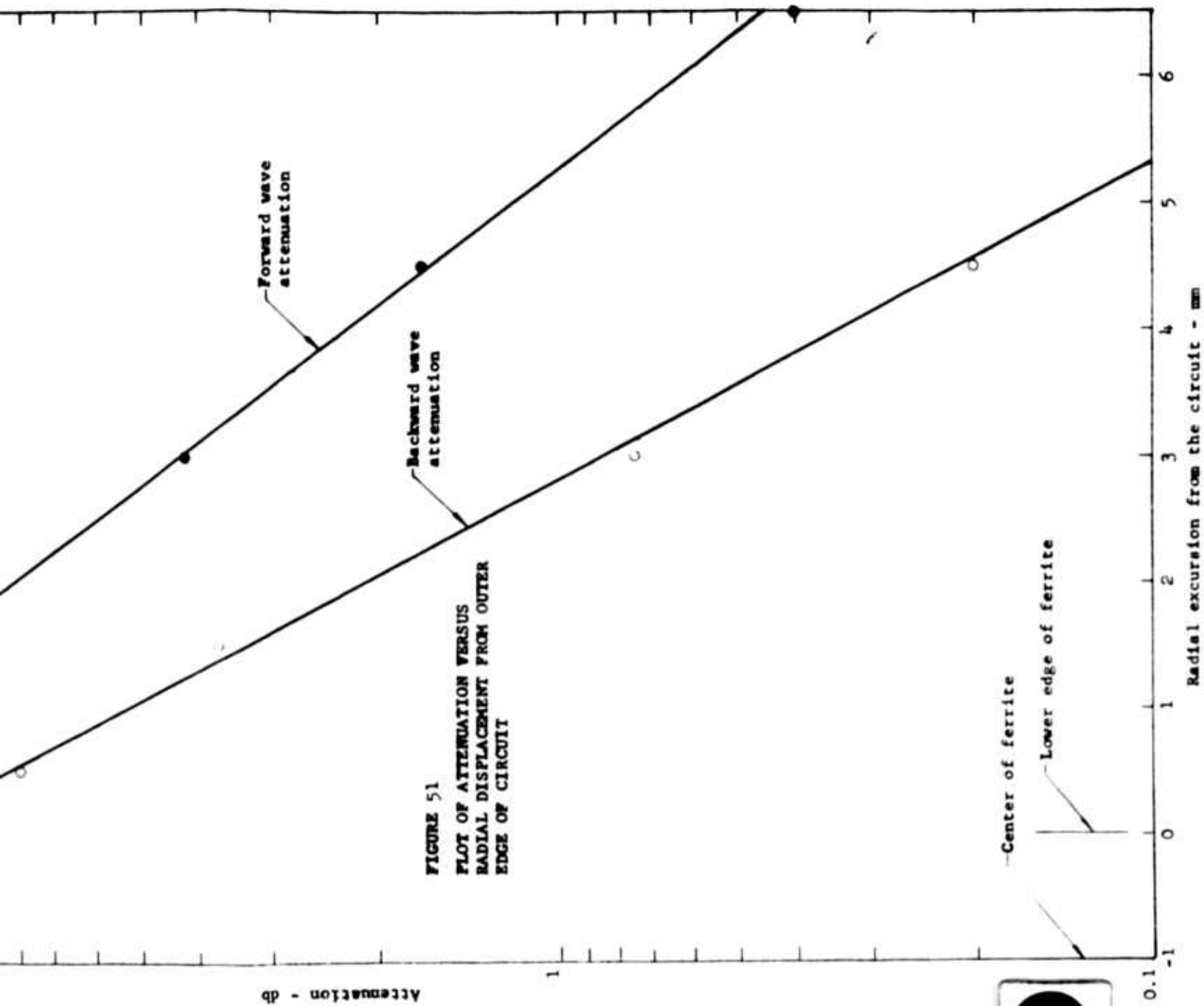


FIGURE 51  
 PLOT OF ATTENUATION VERSUS  
 RADIAL DISPLACEMENT FROM OUTER  
 EDGE OF CIRCUIT

### 6.3 Experimental Results and Their Comparison with Theory

The isolating quality of the AN50MW ferrite sample under consideration is determined by measuring the transmission loss of the circuit as the ferrite is brought into close proximity with it. With the ferrite in place, the circuit is immersed into a uniform magnetic field. A measurement is taken of the transmission loss of the incident power as a function of the dc magnetic field applied as shown in Figure 52.

If conditions are such that  $\vec{h}_{RF} \times \vec{H}_{dc}$  (applied) exists, then absorption will take place in accordance with Kittel's equation.

#### 6.3.1 Kittel's Equation

The frequency at which ferromagnetic resonance occurs is related to the applied dc magnetic field and other parameters as follows (Ref. 3)

$$\omega_r = \gamma \left[ \left( H_0 + (N_x + N_x^a - N_z)4\pi M_s \right) \left( H_0 + (N_y + N_y^a - N_z)4\pi M_s \right) \right]^{\frac{1}{2}}$$

where the  $N_x, N_y, N_z$  are demagnetizing factors, such that  $N_x + N_y + N_z = 1$  in the cgs system of units. Here it is understood that we are using dc equivalent demagnetizing factors, meaning that we assume that the ferrite specimen is small compared to a wavelength in the specimen. The  $N^a$  terms take into account the demagnetization due to magnetic anisotropy; they are defined in such a way that  $H_x^a = -N_x^a M$  and  $H_y^a = -N_y^a M$ .  $\gamma$  is the gyromagnetic ratio for the electron = 2.8 Mc/oerstead = 1.4 g where "g" is the Landé splitting factor (usually equal to 2).

- 
3. Benjamin Lax and Kenneth J. Button, MICROWAVE FERRITES AND FERRIMAGNETICS, McGraw-Hill Book Company, Inc. (1962) p. 159, Eq. 4-30 (in a modified form)

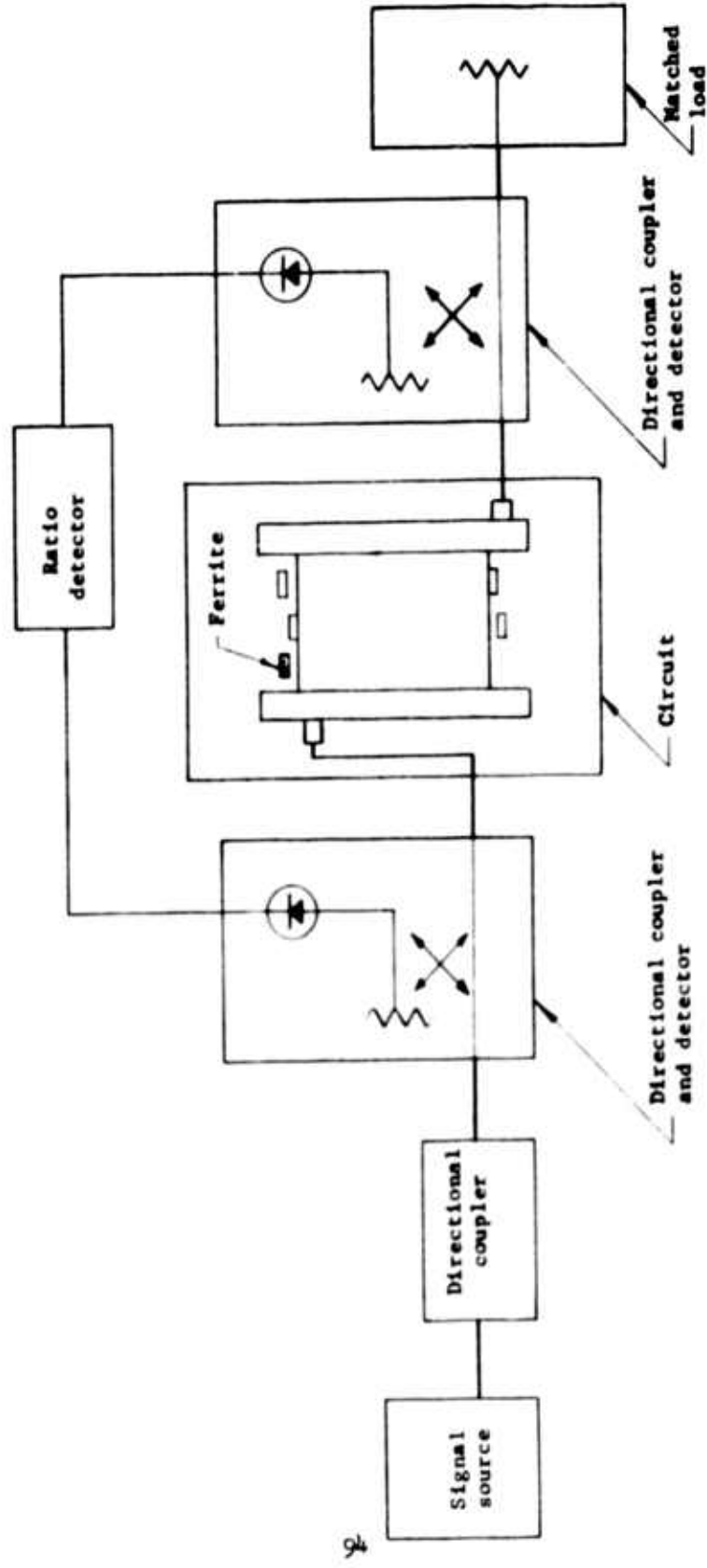


FIGURE 52 MEASUREMENT OF TRANSMISSION LOSS OF THE CIRCUIT WITH FERRITE ELEMENT PRESENT

$H_0$  is the applied dc field, assumed above in the z-direction; i.e., the form of Kittel's equation is such that it applies for a z-directed dc field.

$4\pi M_s$  is the saturation magnetization of the ferrite sample measured in gauss.

$\omega_r$  is the resonant frequency in megacycles.

### 6.3.2 Discussion of the Demagnetizing Factors and their Applicability in this Case

As mentioned above, the demagnetizing factors strictly apply for the ferrite dimensions, for which demagnetization may be effective, smaller than a wavelength in the specimen.

For a slow wave the propagation constant is much larger than the free space propagation constant. As a result, since  $\beta = 2\pi/\lambda$ , the effective wavelength of such a wave is much smaller than the corresponding length in free space. Comparing the relative lengths, we get

$$\frac{\lambda_g}{2} \text{ for } \beta(\text{slow wave}) \ll \frac{\lambda_g}{2} \text{ for } \beta(\text{fast wave}), \beta_0 = \omega\sqrt{\mu\epsilon}$$

where  $\beta = \sqrt{\beta_0^2 - \beta_c^2}$

at high enough phase shift per section; i.e., the region in which we operate, we can neglect  $\beta_c$  in comparison to  $\beta_0$ . As a result we can obtain a direct relationship between  $\mu$  and the dielectric loading - i.e.,  $\beta$  will vary as  $\sqrt{(\mu/\mu_0)(\epsilon/\epsilon_0)}$ . For our operating condition,  $\beta(\text{slow wave}) = 480$  radians/meter.

Therefore for  $\pi$  radian variation we need  $\pi/480 \simeq 6.5$  mm (without dielectric loading). However, we must remember that the ferrite behaves as a dielectric and that its permeability is also variable. Figure 53 illustrates the relationship between ferrite geometry and extent of  $h_{RF}$  field loops.

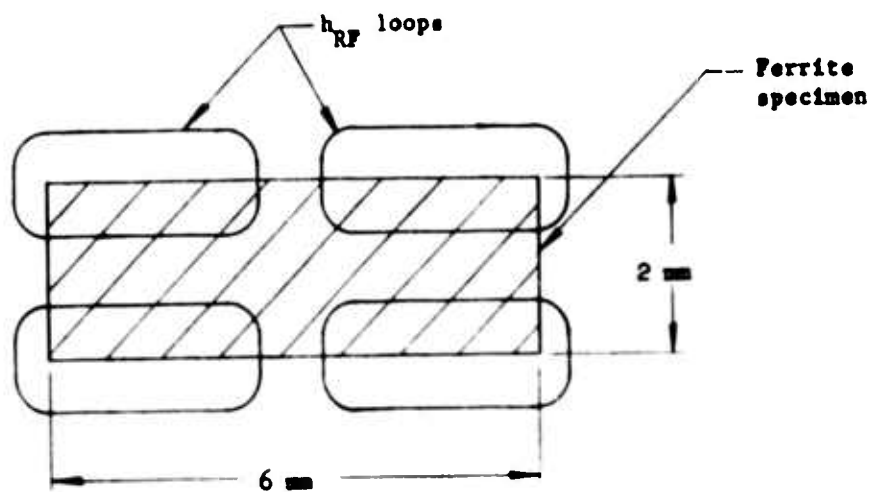


FIGURE 53 RELATIONSHIP BETWEEN FERRITE GEOMETRY AND EXTENT OF  $h_{RF}$  FIELD LOOPS

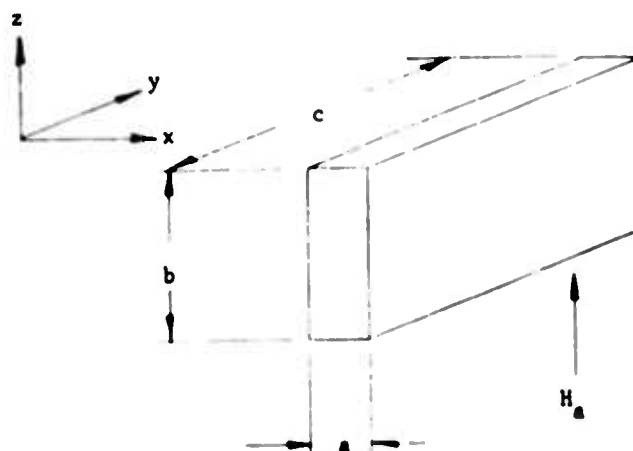
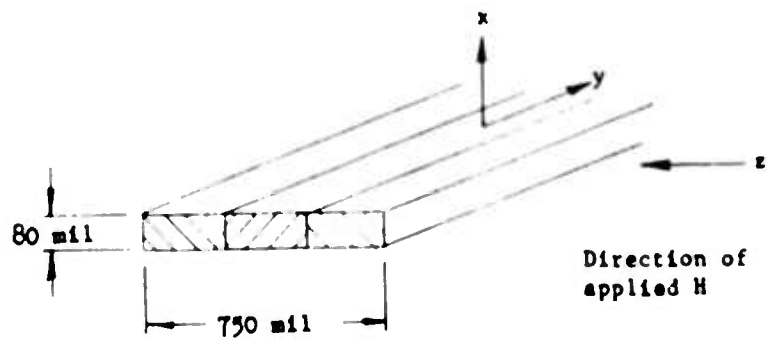


FIGURE 54 DESCRIPTION OF DEMAGNETIZING FACTORS IN A SLAB

FIGURE 55 RELATING TO THE FERRITE GEOMETRY UNDER CONSIDERATION





A typical value of  $\epsilon/\epsilon_0$  for ferrites is 13. Now (Ref. 4)

$$\mu^+ = \mu_0 \left[ 1 + \frac{\gamma^2 M_0^2}{\omega_0 \mp \omega + jT} \right]$$

where  $2/T = \gamma \Delta H$ ,  $\omega_0 = \gamma 4\pi M_0$

Then, at resonance,  $\omega_0 = \omega$ , then

$$\mu^+ = \mu_0 \left[ 1 + \frac{\gamma^2 M_0^2}{j \frac{2}{\gamma \Delta H}} \right]$$

Note that the first term in the bracket is real - it contributes to the propagation term; the second term is imaginary - it contributes to the loss term. Therefore, at resonance,  $\mu^+ = \mu_0$ . As a result,  $\beta_x$  increases in the ferrite by a factor of  $\sqrt{\epsilon/\epsilon_0} \simeq \sqrt{13}$ . Therefore  $\pi$  phase shift will occur over a slab thickness of  $6.5 \text{ mm}/\sqrt{13} \simeq 1.8 \text{ mm}$ . This dimension is of the order of magnitude of the smallest dimension of the cross-section of the ferrite. Thus the demagnetizing effect will be reduced for the largest dimension. It is the smallest dimension which has by far the largest influence on demagnetization.

Demagnetization effects are taken into account as follows (Figure 54, Ref. 5)

$$\begin{aligned} N_x &= \frac{b}{a+b} \\ N_y &= 0 \\ N_z &= \frac{a}{a+b} \end{aligned}$$

---

4. Op.cit., p. 554, Eq. 12-3

5. J. Roberts, HIGH FREQUENCY APPLICATIONS OF FERRITES, D. Van Nostrand Company, Inc. (1960), Fig. 3.15, p. 90

It is implicitly assumed that a and b are the minor and major axes, respectively, of an ellipse whose boundaries introduce demagnetizing effects.

Thus since the order of magnitude of the ferrite thickness is comparable to a half wavelength in the ferrite, no conclusion can be reached about the effective demagnetizing factors, except perhaps that their effect should be smaller than under fast wave conditions.

### 6.3.3 Correlation between Experimental Results and Kittel's Equation

In the experiments with the AN50MW samples, resonance was obtained for (refer to Figure 54)

$$(A) \quad N_x = 3/4, \quad N_y = 0, \quad N_z = 1/4 \quad \text{with } a = 2 \text{ mm}, \quad b = 6 \text{ mm}$$

$c \gg a, b$  and using equations for Figure 54  
resonance occurred for  $H(\text{applied}) = 560$  oersteds.  
Check in Kittel's equation, assuming  $N^a = 0$ , then

$$\frac{\omega}{\gamma} = \left[ \left( 560 - \frac{350}{4} \right) \left( 560 + 175 \right) \right]^{\frac{1}{2}} = 591$$

for AN50MW,  $\gamma = 1.4 \text{ g} \approx (1.4)(1.5) = 2.1 \text{ Mc/oersted}$   
 $g(\text{effective}) = 1.5; \quad 4\pi M_s = 350 \text{ gauss}$

$$\therefore f(\text{resonant, Kittel}) = 1238 \text{ Mc}$$

In the experiment,  $f(\text{resonant})$  was  $\approx 1250 \text{ Mc}$

Thus there is correspondence within  $\frac{1250 - 1238}{1250} = 1\%$

(B) Changing the demagnetizing factors by tripling the width of the ferrite slab (as shown in Figure 55) we get

$$N_x = \frac{b}{a + b} = \frac{80 \text{ mil}}{830 \text{ mil}} = 0.096$$

$$N_y = 0$$

$$N_z = \frac{a}{a + b} = \frac{750 \text{ mil}}{830 \text{ mil}} = 0.904$$

In this experiment,  $H(\text{applied}) = 480$  oersted.

Then substituting in Kittel's equation we get, with  $N^A = 0$

$$\frac{\omega}{\gamma} = \left[ (480 - (0.096)(350)) (480 + (0.808)(350)) \right]^{\frac{1}{2}}$$

$$\gamma = 1.4 \text{ g} = 2.1 \text{ Mc/oersted}$$

$\therefore \omega_r = 1230 \text{ Mc}$ , where  $\omega_r$  is the resonant frequency  
obtained from Kittel's equation

The experimental frequency was  $f = 1240 \text{ Mc}$

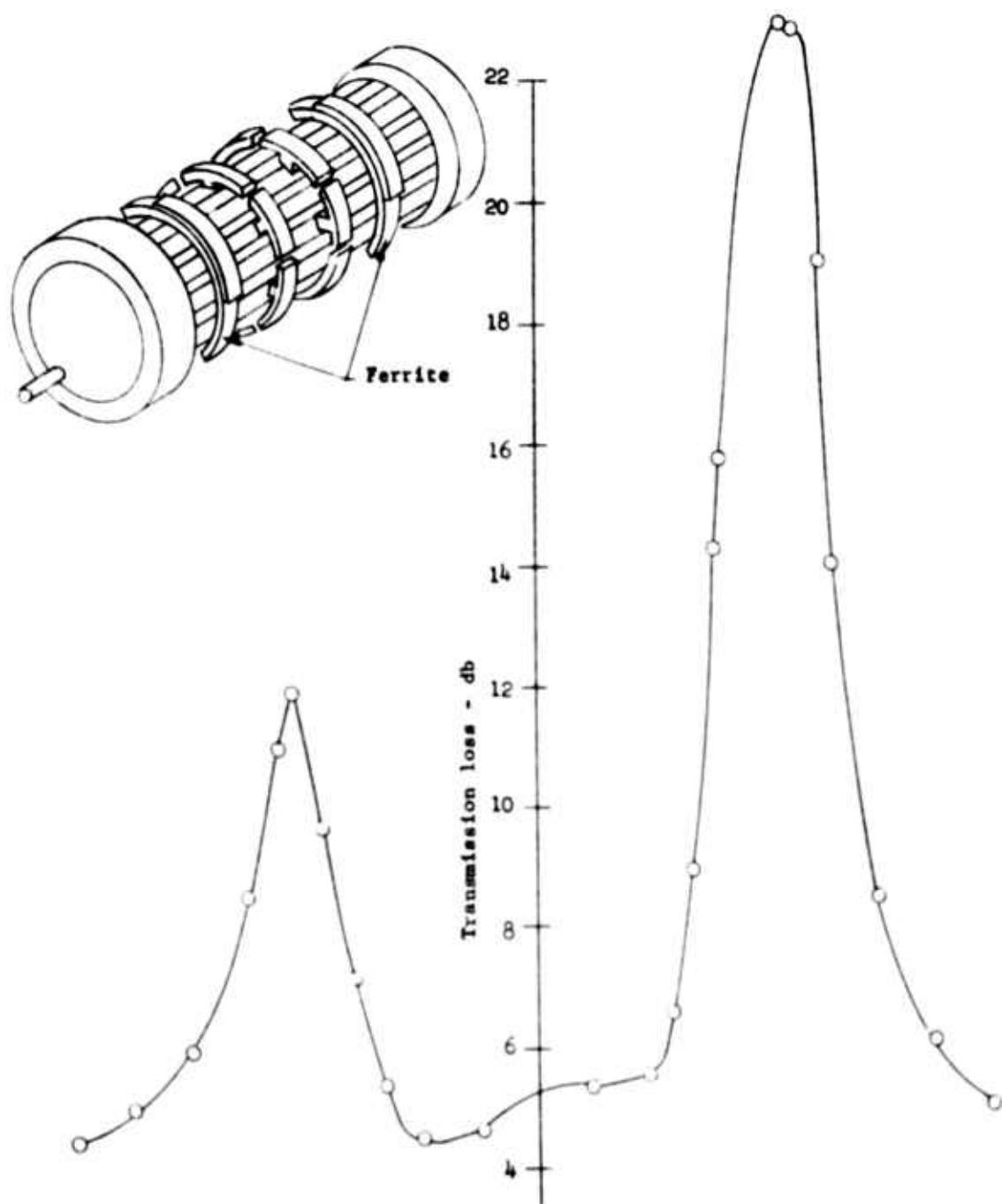
$\therefore$  correspondence within  $\frac{1240 - 1230}{1240} < 1\%$

We conclude from two independent experiments that the assumption of dc demagnetizing factors properly describes the behavior of the ferrite (under the assumption that effects due to anisotropy can be neglected).

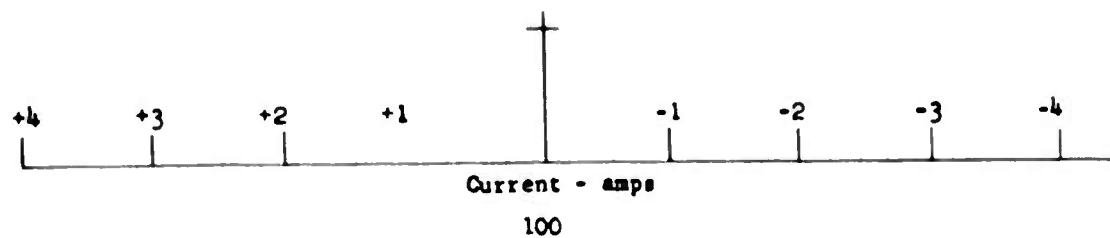
#### 6.3.4 Discussion of Experimental Results

The bell shaped attenuation versus magnetic field plots which are obtained, as shown in Figures 56 and 57, correspond to expectations. The ferromagnetic resonance phenomenon causes the imaginary part of the susceptibility  $\chi''$  to vary approximately as  $1/(\omega^2 - \omega_0^2)$  where  $\omega$  is the frequency of the applied signal and  $\omega_0$  is the ferromagnetic resonance frequency satisfying Kittel's equation. In the denominator of the abovementioned expression, there should be a loss component which keeps  $\chi''$  finite at resonance.

A study of the plots of transmission loss versus applied dc magnetic field shows that the peaks of both bumps occur at the same magnitude of dc magnetic field. This can be explained as follows. Both "bumps" are due to ferromagnetic resonance - the larger loss due to interaction with the forward waves, the smaller loss due to interaction with the backward waves. Since the abovementioned waves are



**FIGURE 56 TRANSMISSION LOSS VERSUS MAGNETIC FIELD APPLIED TO CIRCUIT**



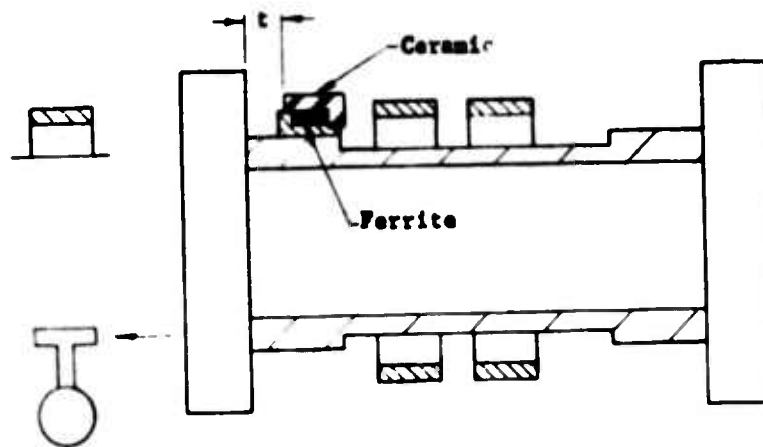
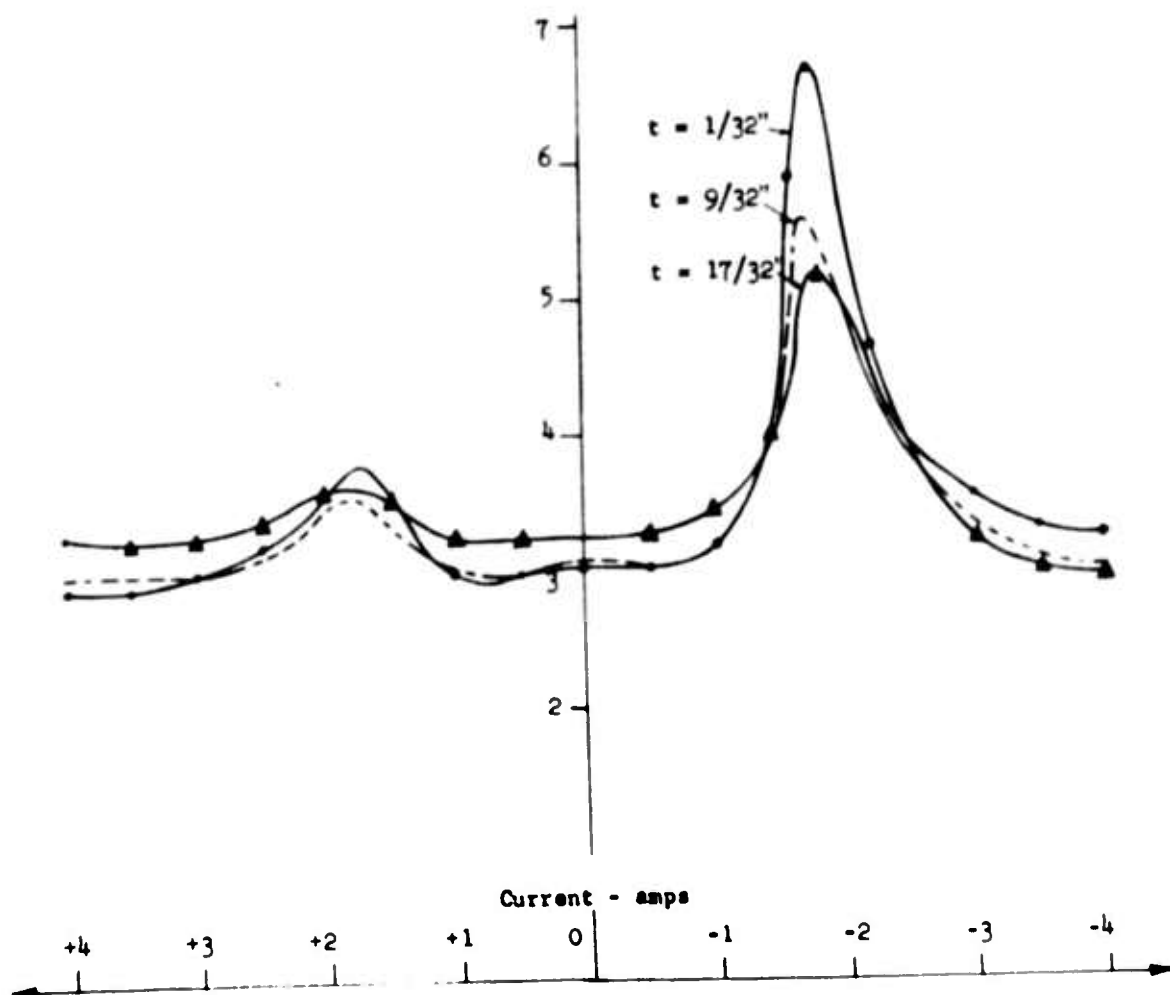


FIGURE 57 TRANSMISSION LOSS VERSUS MAGNETIC FIELD APPLIED TO CIRCUIT WITH LATERAL DISPLACEMENT AS A PARAMETER



components of the same wave, the interaction should occur at the same amplitude of magnetic field. This can be demonstrated from an analysis of Figure 51 - plot of the attenuation introduced at ferromagnetic resonance by the ferrite versus radial displacement from the surface of the circuit.

Another observation from the plots of transmission loss versus applied dc magnetic field leads to a puzzling conclusion. In the vicinity of the zero field region, there appears to be a slight bump. This can be attributed to zero field loss by the following reasoning.

From theory of zero field loss, the maximum frequency at which it can occur is given by

$$f = \gamma [H(\text{anisotropy}) + 4\pi M]$$

For our ferrite sample (a nickel ferrite) AN50MW,  $4\pi M_s = 350$  gauss,  $\gamma = 1.4 \text{ g} = (1.4)(1.5) = 2.1 \text{ Mc/oersted}$ . Since the experimental frequency is about 1200 Mc, the minimum anisotropy field that will cause loss at this frequency is

$$H(\text{anisotropy}) = \frac{1200}{2.1} - 350 = 220 \text{ oersted}$$

Therefore zero field loss will occur for  $H(\text{anisotropy}) \geq 220$  oersted. This value seems to agree with the order of magnitude of anisotropy field in nickel ferrite from Lax and Button (Ref. 6) given as 260 oersted, as well as the value given by Smit and Wijn (Ref. 7), about 280 oersted. Since the frequency at which we are operating is close to the maximum

---

6. Op.cit., p. 942, Table 12-I

7. J. Smit and H. P. Wijn, FERRITES - PHYSICAL PROPERTIES OF FERROMAGNETIC OXIDES IN RELATION TO THEIR TECHNICAL APPLICATIONS, John Wiley & Sons, Inc. (1959), p. 163, Table 34 II

frequency at which zero field loss can occur for this material, it is reasonable to conclude that the zero field losses should be low. Note that for  $H^a = 260$  oersted,  $f_{\max}(\text{zero field loss}) = (2.1)(260 + 350) = 1280$  Mc. It can be seen from the graphs that this loss does not exceed 1 db. According to the above argument, it appears plausible that anisotropy fields are present in the ferrite specimen and that they are large - of the order of 200 oersted, a value which certainly is not negligible in comparison with the applied dc field or the magnetization saturation.

However, if we substitute this value in Kittel's equation, we no longer get a correspondence between the latter and experiment (although excellent agreement is obtained when we assume  $H(\text{anisotropy}) \rightarrow 0$ ). One possibility remains - the reduced demagnetizing effects due to the presence of a slow wave cancel the anisotropy fields. This coincidence, although possible for one set of demagnetizing factors, appears highly unlikely in two independent experiments.

Consequently, since the behavior of the ferrite was well described by the assumption of dc ellipsoidal demagnetizing factors and no anisotropy fields in Kittel's equation, we shall use that relation in the determination of the ferrite geometry proper in avoiding low field loss.

### 6.3.5 Low Field Loss

#### 6.3.5.1 Zero Field Loss

As previously discussed, the expression relating the maximum frequency at which these losses occur at zero applied field is

$$\omega_r(\max) = \gamma [H(\text{anisotropy}) + 4\pi M_0]$$

### 6.3.5.2 Low Field Loss

The above relationship applies for a non-saturated ferrite sample. If, however, we assume that the ferrite will always be saturated under operating conditions, then the following relation will hold because low field loss occurs as long as the ferrite specimen is not fully magnetized

$$\omega_{res} = \gamma [H_{za} + (N_x - N_z)4\pi M_s] = \gamma [H_{za} + (N_y - N_z)4\pi M_s] \quad (1)$$

where  $H_{za}$  is the applied dc magnetic field

Now

$$H_z(\text{internal}) = H_{za} - N_z 4\pi M_s \quad (2)$$

Hence to avoid low field loss,  $H_z(\text{internal})$  must be such as to saturate the material; i.e.,

$$H_{za} = H(\text{saturated}) + N_z 4\pi M_s \quad (3)$$

To find maximum  $4\pi M_s$  allowed for a given geometry (hence  $N_z$  in eq. (3)), assume that proper value of  $H_{za}$  is applied in eq. (1) and that ferrite is resonant at frequency  $\omega_{res}$ . Since from eq. (3) we know  $H_z$  and since  $N_z + N_x = 1$ ,  $N_y = 0$ , we can solve for  $4\pi M_s$  in eq. (1). This is the maximum allowable  $4\pi M_s$  in order for no low field loss to occur. Again, here, we have neglected any anisotropy field, in accordance with the argument that Kittel's equation is well obeyed using dc demagnetizing factors and neglecting anisotropy fields. It is instructive to plot  $4\pi M_s$  allowable versus demagnetizing factor, with  $H(\text{saturated})$  as a parameter (Figure 58) and to superimpose on this series of plots the graphical relationship between the demagnetizing factor and  $4\pi M_s$  necessary to avoid the first order non-linear effect. (See discussion of non-linear effects in ferrite, Section 6.5)



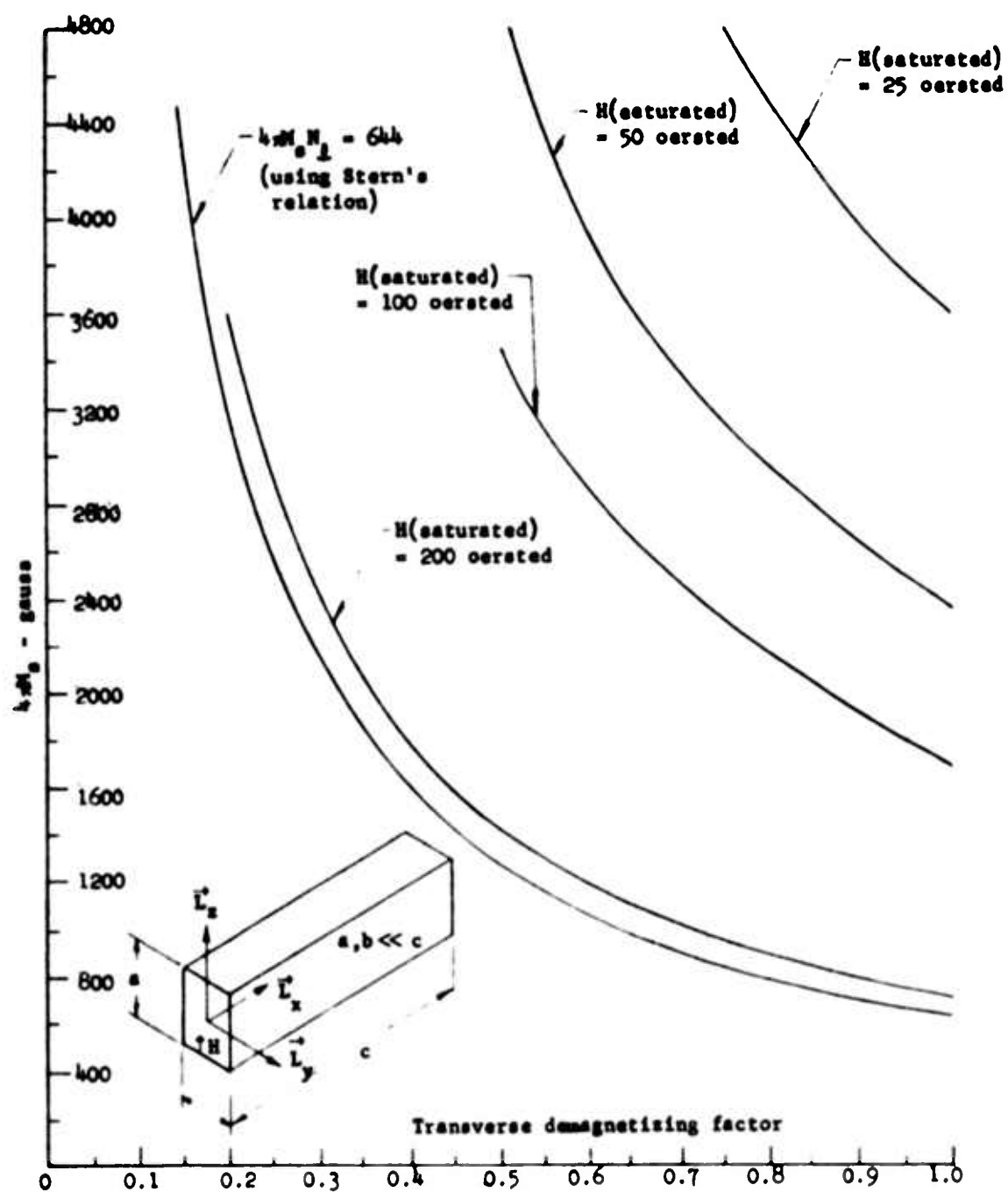


FIGURE 58 DETERMINATION OF MAXIMUM ALLOWABLE  $4\pi M_0$  AS A FUNCTION OF TRANSVERSE DEMAGNETIZING FACTOR

Note further that complete eradication of low field loss is not imperative in our application. We can tolerate some, associated with the ferrite per se (say of the order of, but less than, 1 db) because the nature of our circuit is such that forward loss must occur due to the existence of backward wave components in the slow wave. Thus a behavior, as shown in Figure 59, is permissible.

### 6.3.5.3 Isolation and Attenuation Ratio

It is our goal to obtain between 15 db and 20 db of isolation between transmission in the forward direction and transmission in the backward direction and a front to back ratio of at least 10 db/1 db. This appears to be realizable in light of the following reasoning.

In the experiments with the AN50MW ferrite rings, we observed that under proper conditions a 10:1 front to back ratio was obtainable with the ferrite placed sufficiently far away from the surface of the circuit (Figure 51). Due to the effects of the backward wave which causes an attenuation in the forward direction, we are required to move the ferrite back far enough - i.e., until this effect becomes negligible. However the maximum attenuation in the reverse direction was only 1 db.

(a) Since the attenuation  $\alpha$  of the ferrite is proportional to  $\chi''$  which is in turn proportional to  $\frac{4\pi M_s}{\Delta H}$ , we need to choose a material such that

$$\left[ \frac{4\pi M_s}{\Delta H} \right]_{\text{material}} > \left[ \frac{4\pi M_s}{\Delta H} \right]_{\text{AN50MW}}$$

Now since the attenuation is of exponential character  $\alpha$  db/meter and since we were using only 1/3 of the circumference for attenuation by the ferrite, we should be able to increase the attenuation by a factor of

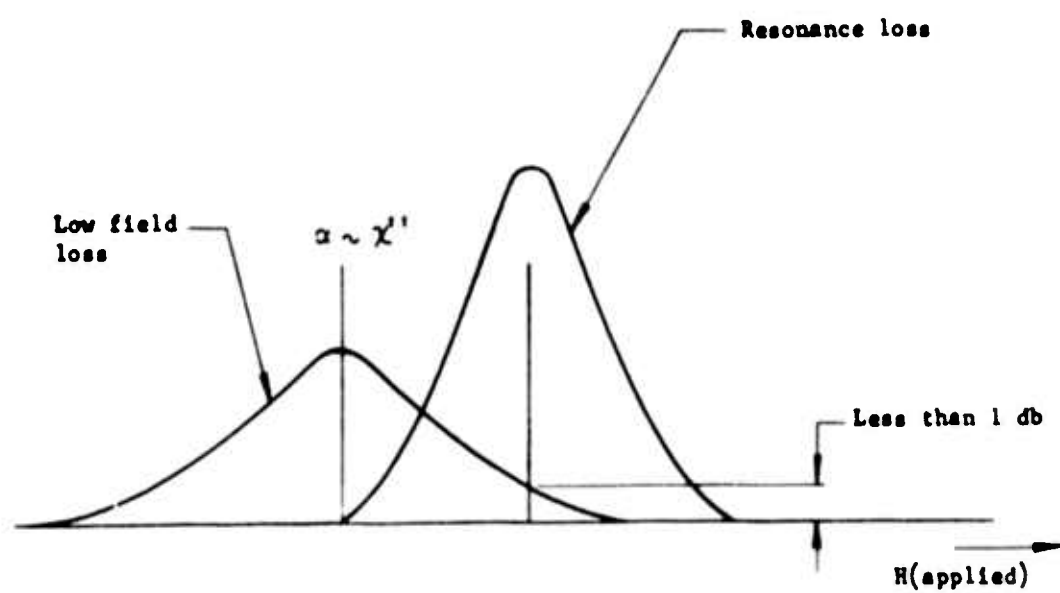


FIGURE 59 RELATING TO THE DESCRIPTION OF LOW FIELD LOSS  
IN RELATION TO RESONANCE LOSS

$$(2.5) \left[ \frac{4\pi M_s}{\Delta H} \right]_{\text{material}} \cdot \left[ \frac{1}{\left( \frac{4\pi M_s}{\Delta H} \right)_{\text{AN50MW}}} \right]$$

Factor of 2.5 because we cannot "wrap" the ferrite around the circuit over more than  $2.5/3 \times 360^\circ = 300^\circ$ . It appears likely that we shall be able to use a material having

$$\frac{4\pi M_s}{\Delta H} \geq (4) \left[ \frac{4\pi M_s}{\Delta H} \right]_{\text{AN50MW}}$$

(b) If we use a ferrite ring on either side of the ferrite coupler region, since both sides have the same polarization, we should be able to get an improvement in isolation of 3 db.

(c)  $4\pi M_s/\Delta H \sim \alpha$  db/meter is temperature sensitive since  $\Delta H$  decreases for increasing temperature while  $4\pi M_s$  remains constant. (We will choose the material such that this condition is maintained.) As a result, at higher temperatures (under operating conditions for the tube), the attenuation should be better than for cold test.

(d) By using ferrite sample having the axial dimension larger than that of the AN50MW sample, we should be able to increase the attenuation. Note that the region of circular polarization is quite extensive and apparently uniform axially along the circuit (Figures 60 and 61).

#### 6.3.6 Linewidth Requirements for 10% Bandwidth

According to Suhl (Ref. 8), the imaginary component of the susceptibility of the ferrite is equal to

$$\chi'' = \frac{\gamma M_s \Delta H}{(\omega - \omega_{res})^2 + \gamma^2 \Delta H^2}$$

- 
8. H. Suhl, "The Nonlinear Behavior of Ferrites at High Microwave Signal Levels," Proc. Inst. Radio Engrs., Vol. 44, No. 10 October 1956, pp 1270-1284

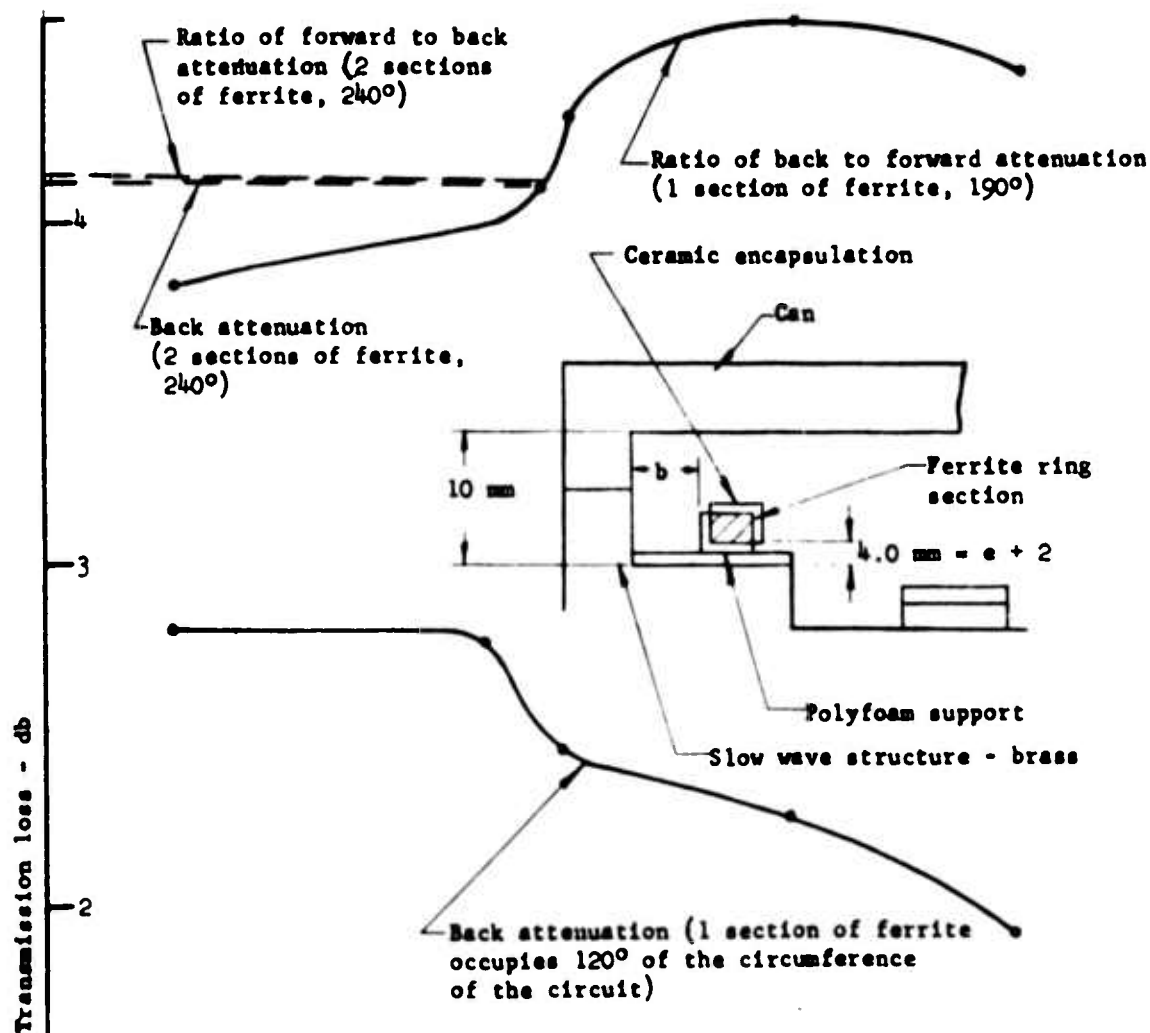
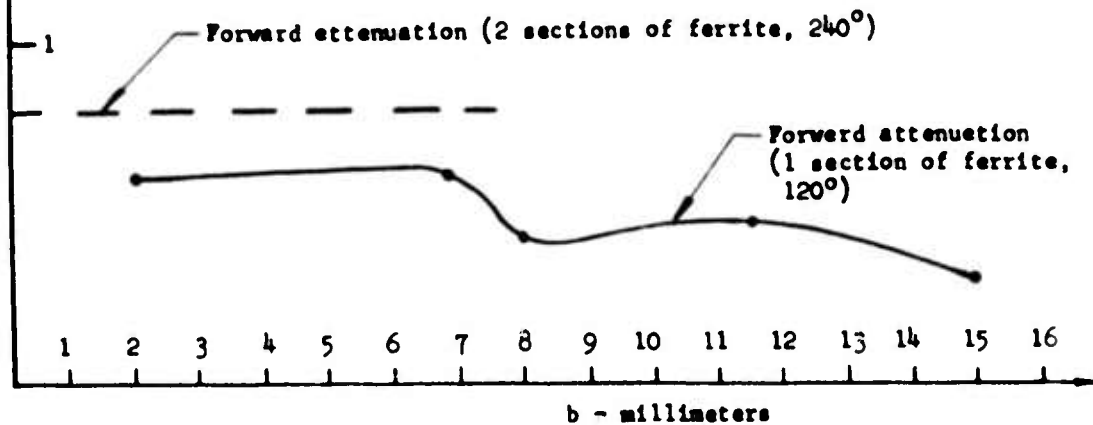


FIGURE 60 MEASUREMENT OF TRANSMISSION LOSS OF BRASS STRUCTURE LOADED ON ONE SIDE WITH FERRITE RING SECTION



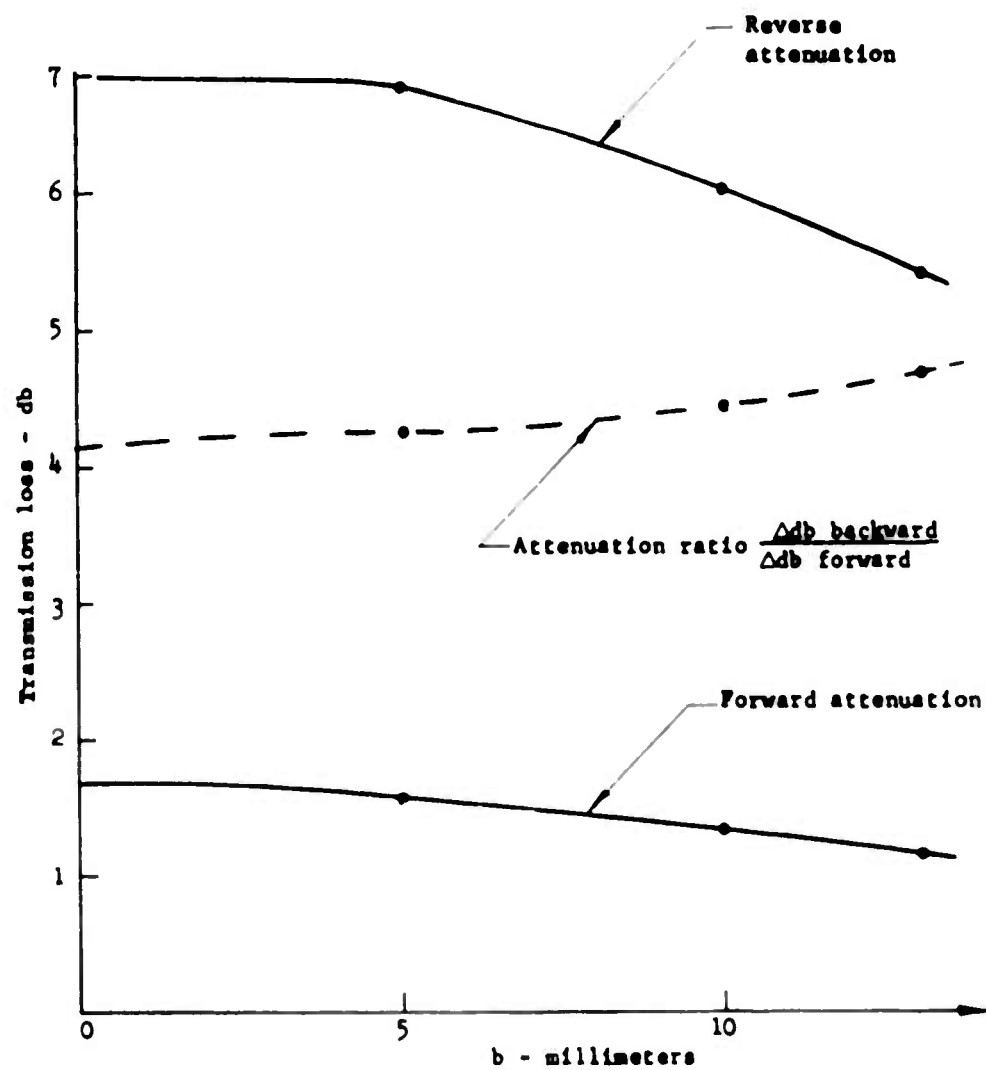


FIGURE 61 MEASUREMENT OF TRANSMISSION LOSS OF BRASS STRUCTURE LOADED ON ONE SIDE WITH FERRITE RING SECTION,  $a = 1$  mm

where  $\gamma = 2.8 \text{ Mc/oersted}$   
 $M = 1/4\pi$  (saturation magnetization)  
 $\Delta H$  = linewidth in oersteds  
 $\omega_{\text{res}}$  = resonant frequency

Now at resonance,  $\omega = \omega_{\text{res}}$  or

$$\chi''_{\text{max}} = \frac{\gamma M \gamma \Delta H}{\gamma^2 \Delta H^2} = \frac{M}{\Delta H}$$

Since the linewidth is measured at the front where  $\chi''$  falls to half the value of the maximum, then

$$\chi''_{\frac{1}{2}\text{max}} = \frac{\gamma M \gamma \Delta H}{(\Delta \omega)^2 + \gamma^2 \Delta H^2} = \frac{1}{2} \chi''_{\text{max}}$$

Therefore

$$\frac{\chi''_{\text{max}}}{\chi''_{\frac{1}{2}\text{max}}} = 2 = \frac{\Delta \omega^2 + \gamma^2 \Delta H^2}{\gamma^2 \Delta H^2} \text{ or } \Delta \omega^2 = \gamma^2 \Delta H^2 \text{ or } \Delta \omega = \gamma \Delta H$$

Therefore the bandwidth is  $\gamma \Delta H$ .

Since we require 10% bandwidth - 120 Mc - the minimum  $\Delta H$  allowable is  $\Delta H = \Delta \omega / \gamma = 120 / 2.8 = 42.9$  oersted.

The above value should be increased by at least a factor of 2 because it presently corresponds to a drop in  $\chi''_{\text{max}}$  by a factor of 2. But  $\chi''$  is proportional to the attenuation  $\alpha$  db of the ferrite. If we assume  $\alpha(\text{total}) = 15$  db then  $\alpha/2 \approx 7.5$  db; hence for a 3 db drop in attenuation (across the bandwidth) we can reasonably assume a necessary  $\Delta H$  of  $(42.9 \times 7.5 \text{ db}) / 3 \text{ db} \approx 100$  oersted. Therefore we should choose a material such that under operating conditions it exhibits  $\Delta H \geq 100$  oersted.

### 6.3.7 Effect of Temperature on Linewidth

There is a rapid decrease of linewidth with temperature for yttrium-gadolinium-iron garnet (Ref. 9). A similar behavior is seen for yttrium-samarium-iron garnet (Ref. 10). For nickel ferrites,  $\Delta H$  drops to half its room temperature value at 100°C.

Therefore, we must choose a material with  $\Delta H$  as high as possible to get reasonable bandwidth under operating conditions. However, we do not know the temperature at which the ferrite will operate under steady state conditions. Thus we guess that this temperature will be 100°C and on this basis proceed to choose the proper material for our application.

### 6.3.8 Experimental Results

#### 6.3.8.1 Linewidth

According to Soohoo (Ref. 11) the linewidth of polycrystalline ferrite is a function, among other factors, of geometrical demagnetizing effects. These act in a direction to increase broadening.

For a slow wave, these demagnetizing factors with respect to RF may be even more reduced so that the specified  $\Delta H$  may be closed to the observed  $\Delta H$ . From our experiments, this can be verified from the plots of attenuation versus applied magnetic field (Figures 56 and 57).  $\Delta H$  has been defined as the linewidth at the "half db" absorption points of the sample.

On Figure 56, the half absorption points occur at  $23 + (23-5.4)/2 = 14.2$  db level which yields  $\Delta H = 290$  oersted. In Figure 57 for  $t = 1/32$ ", the half absorption points occur at

- 
9. G. Harrison and L. R. Hedges, "Microwave Properties of Polycrystalline Hybrid Garnets," Microwave Journal, Vol. 4, No. 6, June 1961, Fig. 4, p. 55
  10. Op.cit., Fig. 8, p. 56
  11. Ronald F. Soohoo, THEORY AND APPLICATION OF FERRITES, Prentice-Hall, Inc., (1960), pp. 74-76



$6.65 - (6.65 - 3.0)/2 = 4.82$  db level at which point the line width is  $\approx 210$  oersteds. The specified linewidth of the ferrite sample is 225 oersteds(average); i.e., each sample may show some variation. There is reasonable correspondence between the observed value and the specified value of  $\Delta H$  so that in our choice of a ferrite material we can use the specified  $\Delta H$  as a basis for required  $\Delta H$ .

#### 6.3.8.2 Further Discussion of Experimental Results

##### 6.3.8.2.1 Effect of the can surrounding the structure

A comparison between Figures 51 and 62 indicates that the can seems to disturb the field pattern in the region between the can and the surface of the circuit. This is deduced from the fact the log of attenuation versus distance is no longer linear in the presence of the can. Therefore the circular polarization of the  $h_{RF}$  fields which allowed such a variation to occur has been disturbed, probably due to reflections by the can of the evanescent waves. If the can is placed "far enough" away from the surface of the circuit, this effect should disappear.

This effect is again visible from a comparison between Figures 63 and 64 although the can has been moved back to 10 mm from the circuit. This effect is probably enhanced by the ceramic encapsulation of the ferrite which increases the intensity of the fields in that vicinity.

From Figures 63 and 64 it is furthermore seen that the introduction of the can causes a deterioration of back attenuation to front attenuation.

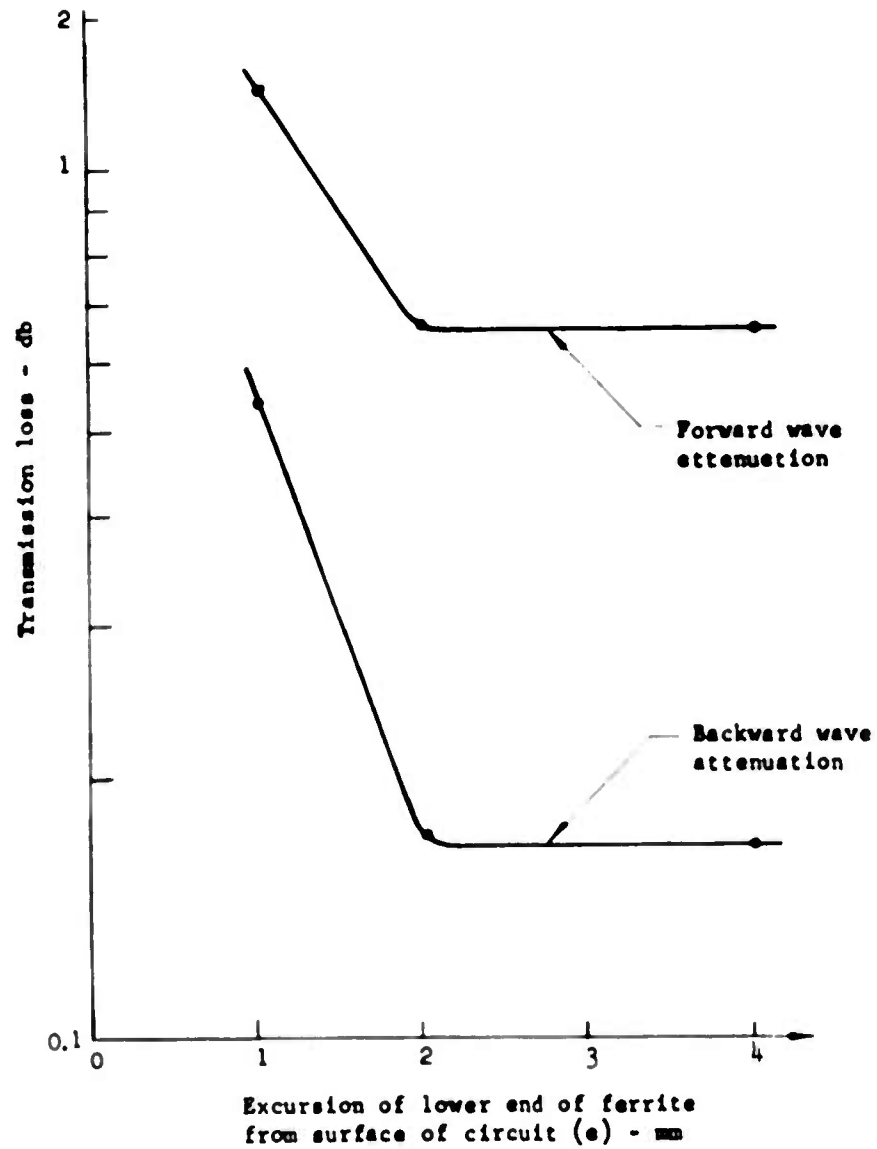
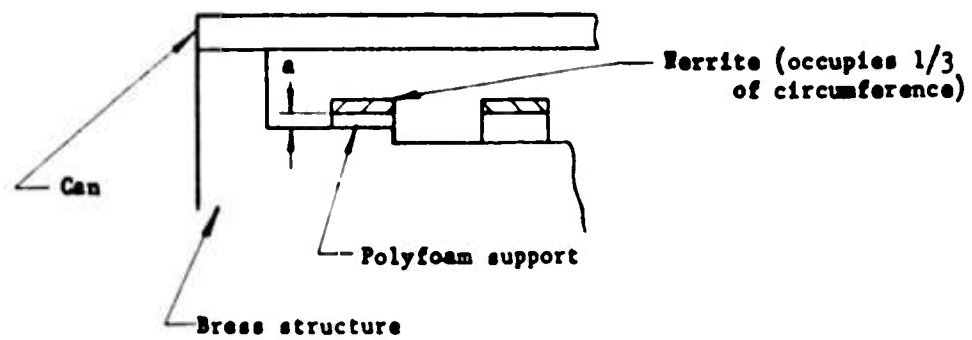


FIGURE 62 PLOT OF ATTENUATION BY THE FERRITE VERSUS RADIAL EXCURSION FROM THE SURFACE OF THE CIRCUIT IN PRESENCE OF CAN

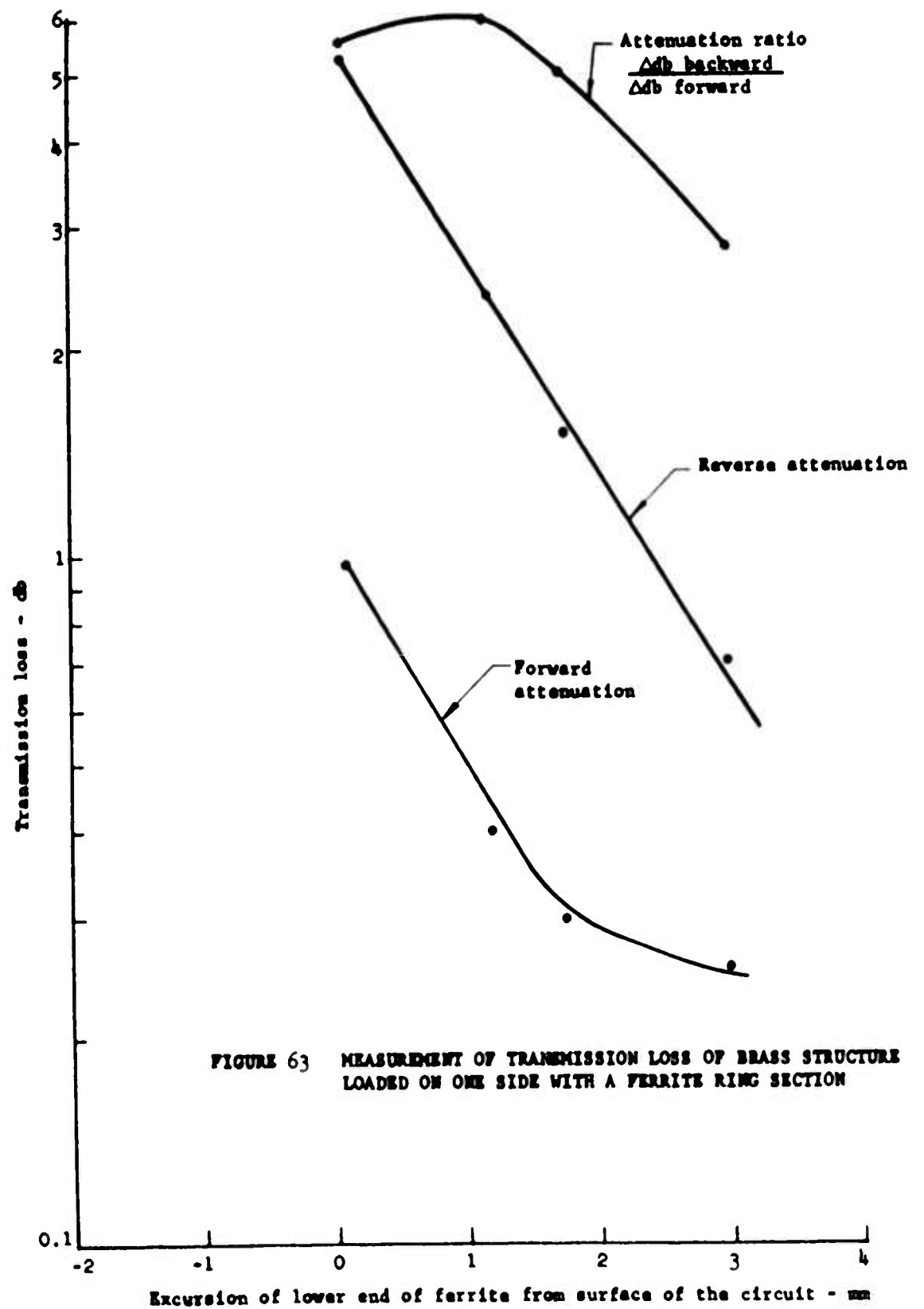


FIGURE 63 MEASUREMENT OF TRANSMISSION LOSS OF BRASS STRUCTURE LOADED ON ONE SIDE WITH A FERRITE RING SECTION

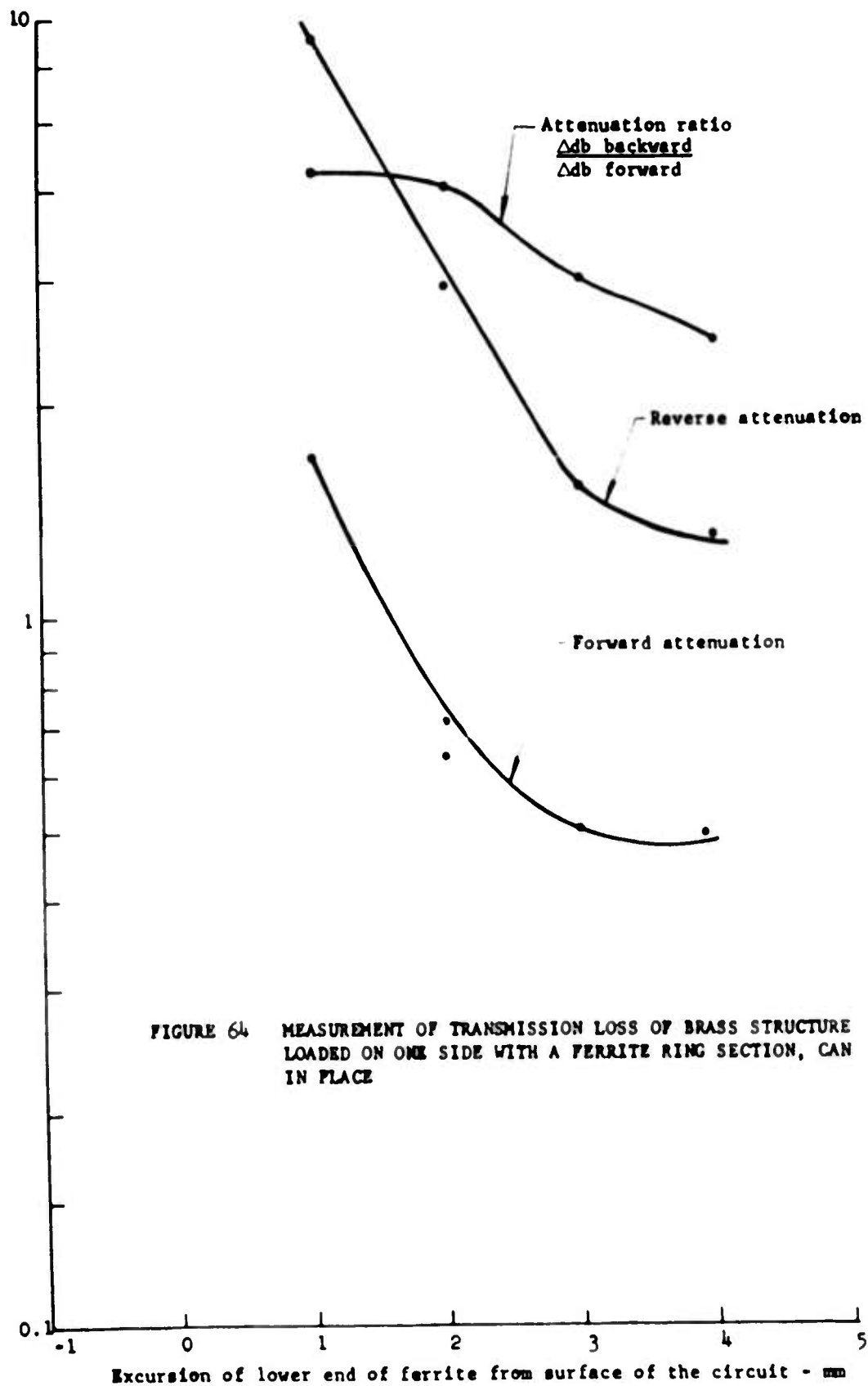


FIGURE 64 MEASUREMENT OF TRANSMISSION LOSS OF BRASS STRUCTURE LOADED ON ONE SIDE WITH A FERRITE RING SECTION, CAN IN PLACE

#### 6.3.8.2.2 Effect of lateral motion of the ferrite

Observing the transmission loss due to the ferrite at a given radial displacement from the circuit in Figures 60 and 61, one concludes that it is but slightly dependent on position. It appears, however, as the ferrite approaches the coupler region, that the ratio of forward attenuation to backward attenuation increases. A similar experiment, conducted in January showed that although the back attenuation decreases as the ferrite approaches, the back to front ratio remains practically unchanged. Therefore, further and more precise experimentation is necessary.

It appears that the ceramic encapsulation somewhat improves the backward attenuation as well as the back to forward attenuation ratio. For example, in data recorded for a given physical configuration without ceramic - attenuation forward = 0.4 db, attenuation back = 1.6 db; whereas with the ceramic in place - attenuation forward = 0.45 db, attenuation backward = 2.45 db.

As can be seen from Figure 60, doubling the length of ferrite did not double the attenuation (as it should, due to the exponential mechanism of absorption,  $\alpha$  db/meter). This may be due to the fact that the rings were broken up into segments.

#### 6.4 Determination of the Geometry and Location of New Ferrite Rings of various Compositions from the Results of Experiments conducted with the AMSCMW Ferrite Rings

From a knowledge of the properties of the materials under consideration, we will find a relationship between the attenuation ratio of these materials and the attenuation ratio of those already tested. From this, we will find the attenuation these materials introduce at a given radial excursion from the circuit. As a result, we will determine the geometry and location of the new ferrite rings.

In order to determine the location of the ferrite, refer to the associated plot, Figure 65. The attenuation per unit length  $\alpha$  db is proportional to  $4\pi M_s/\Delta H$ . Therefore for a material with

$$\frac{4\pi M_s}{\Delta H} = k \left[ \frac{4\pi M_s}{\Delta H} \right]_{\text{AN50MW}}$$

the attenuation at the same radial excursion is k-times as great (in db). In the measurements on the Kearsfott AN50MW sample, we need an arc of  $120^\circ$ , 80 mils thick and 250 mils wide. The absorption that it introduced was extrapolated to be about 1 db at 5.3 mm from the circuit surface (Figure 51). In order to increase attenuation, the circumferential length can be increased by a factor of 2.5, the width can be increased by a factor of 2. Thus, conservatively, we should be able to increase the attenuation of the same material by a factor of  $(1)(2.5) + 3 \text{ db} > 5 \text{ db}$ . Now the energy absorbed by the ferrite is proportional to

$$\int_{\text{ferrite bottom}}^{\text{ferrite top}} K e^{-2\beta y} dy$$

and in the above plot of db attenuation versus radial excursion for various materials at a given attenuation level, K is fixed. Therefore, for a given thickness of material, all the materials will absorb the same energy when the excursion of the bottom of the ferrite ( $\chi$  in the above plot) satisfies the requirement specified by the graph.

Note that we know  $\beta$  from the measurements performed with the AN50MW sample,  $\beta = 466 \text{ rad/meter}$  - in the above plot (and in Figure 66) the slope of the lines corresponding to different materials is the same so that a graphical solution for  $\chi$  is straightforward.

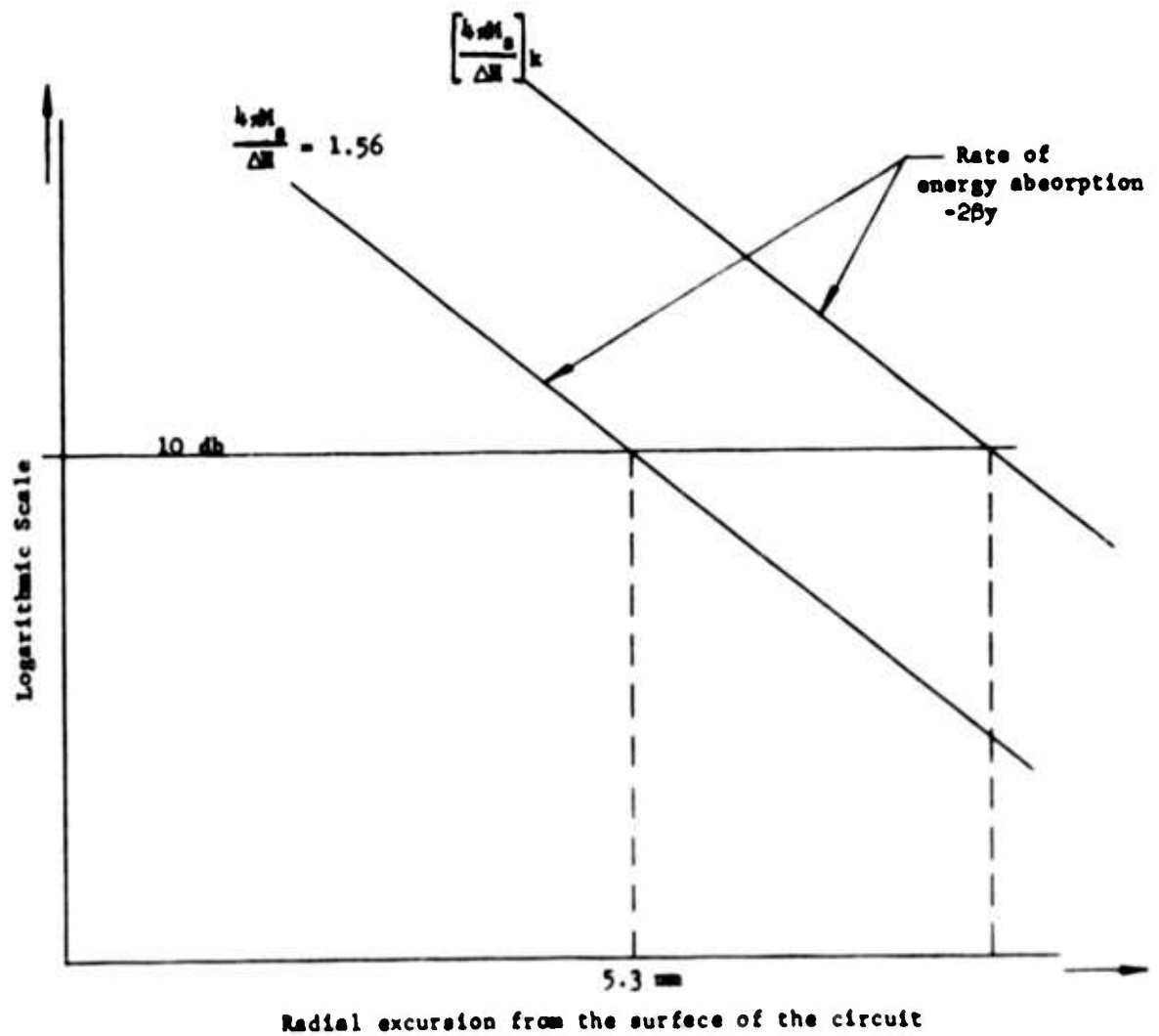
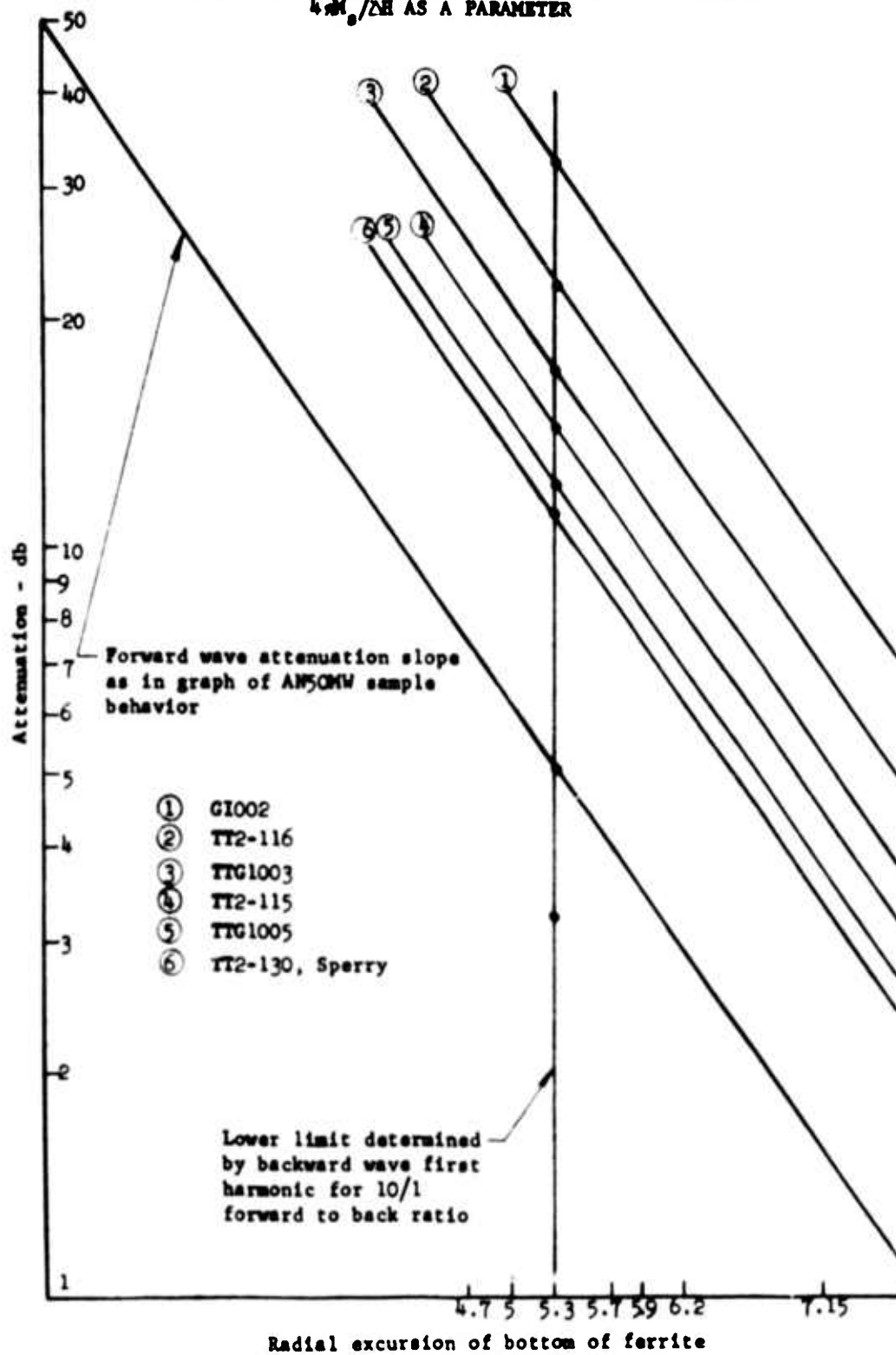


FIGURE 65 GRAPHICAL METHOD FOR DETERMINING THE LOCATION OF THE FERRITE RING WITH RESPECT TO THE SURFACE OF THE CIRCUIT

FIGURE 66 DETERMINATION OF ID OF FERRITE RINGS WITH  $4\pi M_s/2H$  AS A PARAMETER





#### 6.4.1 Effect of increasing the Thickness of the Ferrite on Attenuation

By doubling the thickness to 160 mils or 4 mm, we get

$$\frac{\int_{5.3 \text{ mm}}^{9.3 \text{ mm}} K e^{-2\beta y} dy}{\int_{5.3 \text{ mm}}^{7.3 \text{ mm}} K e^{-2\beta y} dy} = 1.15$$

so that we only attain an increase in absorption energy of 15%.

#### 6.5 Non-linear Effects - First and Second Order

The fields associated with slow wave structures are such that their amplitude is magnified (with respect to the amplitude in a waveguide) by the slowing factor of the structure,  $c/v_g$ , at the operating frequency. As a result, the behavior of the ferrite element will be controlled by its "high power" limitations (resulting from high field intensity) at powers well below those necessary to excite non-linear phenomena of ferrites in conventional waveguide.

According to Suhl's theory (Ref. 12), non-linear effects are due to the fact that certain spin waves become excited as soon as the amplitude of the uniform mode (driven by the applied microwave field) exceeds a certain critical value. These effects are undesirable since they sharply reduce the amplitude of the imaginary part of the susceptibility  $\chi''$ , hence the attenuation  $\alpha$  - especially if coincidence of the first and second order non-linear effects are allowed to occur.

For the first order non-linear effect the frequency of the unstable spin waves corresponds to half the frequency of the applied signal; the second order non-linear effect occurs at the frequency of the applied signal.

---

11. Ibid.

Suhl has shown that the first order effect has an inherently lower threshold than the second order effect (as it sets in at a lower amplitude of  $h_{RF}$ ). It has also been shown by Suhl that the first order effect can be suppressed if the experimental conditions are such that all spin wave frequencies are higher than half the signal frequency (by proper choice of the ferrite geometry in reference to direction of applied dc magnetic field).

This can be accomplished provided that (Ref. 13)

$$\frac{\omega}{\gamma} > \left[ N_x + N_y + \sqrt{N_x^2 + N_y^2 + 4N_x N_y} \right] \frac{4\pi M_s}{3}$$

This relation is obtained by writing Kittel's equation explicitly in terms of  $H_{res}$  (assuming the anisotropy fields are negligible) and assuming that the subsidiary resonance occurs at half the signal frequency or

$$H(\text{subsidiary}) = \frac{\omega}{2\gamma} + N_z 4\pi M_s$$

Since we need  $H(\text{resonant}) \geq H(\text{subsidiary})$ , the above relation is obtained; namely

$$\frac{\omega}{\gamma} > \left[ N_x + N_y + \sqrt{N_x^2 + N_y^2 + 4N_x N_y} \right] \frac{4\pi M_s}{3}$$

However, since  $N_x = 0$  (geometry from Figure 58) the condition becomes

$$\omega > 2\gamma \left[ \frac{4\pi M_s}{3} \right] \quad \text{which appears in Figure 58.}$$

- 
13. E. Stern, "Ferrite Shape Considerations for UHF High-Power Isolators," Trans. Inst. Radio Engrs., PGMTT, Vol. Mtt-8, No. 5, September 1960, p. 565

(Note: In the literature, the  $[ \quad ]$  term above is sometimes referred to as  $2N_{\perp}$  where  $N_{\perp}$  is the transverse demagnetizing factor of the sample.)

Again according to Suhl, the critical  $h_{RF}$  field strength at which the non-linear effect sets in is

$$h(\text{critical}) = (\Delta H) \frac{(\Delta H_K)}{4\pi M_s} F \quad \text{for } \omega < \omega_c \quad (1)$$

$$\text{where } \omega_c = \gamma \left[ N_x + N_y + \sqrt{N_x^2 + N_y^2 + 4N_x N_y} \right] \frac{4\pi M_s}{3}$$

$\Delta H_K$  = linewidth characteristic of the unstable spin waves

$\Delta H$  = observed linewidth of the resonant curve at half maximum height

$F \simeq 1$  for  $\omega \ll \omega_c$ , becoming large as  $\omega$  approaches  $\omega_c$

$$h(\text{critical}) = \Delta H \sqrt{\frac{\Delta H_K}{4\pi M_s}} \quad \text{for } \omega > \omega_c \quad (2)$$

The above relations may need to be modified by a factor of  $\sqrt{2}$ . Note that  $h_{RF}$  is assumed linearly polarized (Ref. 14). This reference discusses both relations. Note also that the  $h(\text{critical})$  refers to the critical field in the structure in the absence of the sample of ferrite.

- 
14. E. Schlömann, J. H. Saunders and M. H. Sirvetz, "L-Band Ferromagnetic Resonance Experiments at High Peak Power Levels," Trans. Inst. Radio Engrs., PGMTT, Vol. MTT-8, No. 1, January 1960, p. 96-100

6.5.1 Calculation of the Magnitude of the  $h_{RF}$  Fields present in our Tube in the Region in which we wish to position the Ferrite

I. Let  $E^2/2\beta^2P = 70$  ohms at the surface of the circuit for the fundamental and let  $v(\text{synchronous})$  be 750 volts. Then

$$v(\text{phase}) = \sqrt{2\eta V} = \sqrt{2 \times 1.759 \times 10^{11} \times 750} = 1.62 \times 10^7 \text{ m/sec}$$

$$\omega = (2\pi)(1250 \times 10^6) = 7.85 \times 10^9 \text{ rad/sec}$$

$$\beta = \omega/v = 485 \text{ rad/meter}$$

Let the peak power be 100 kw; then

$$\begin{aligned} E &= \beta \sqrt{2PK} = (485) \sqrt{(2 \times 10^5)(70)} \\ &= (485)(2.74 \times 10^3) = 1.81 \times 10^6 \text{ volts/meter} \end{aligned}$$

$$H = \frac{1.81 \times 10^6}{377} = 0.48 \times 10^3 \text{ ampere-turns/meter}$$

The decay factor is  $e^{-\beta y}$ ; let  $y = 5 \text{ mm}$  where we intend to place ferrite;  $\beta y = 485 \times 5 \times 10^{-3} = 242$ ;  $e^{-\beta y} = 0.0894$

$$\begin{aligned} \therefore H &= 0.48 \times 10^3 \times 0.0894 = 429 \text{ ampere-turns/meter} \\ &= 429 \text{ a-t/m} \times \frac{1 \text{ oersted}}{79.5 \text{ a-t/m}} = 5.4 \text{ oersted} \end{aligned}$$

II. Instead of assuming the synchronous voltage at 750 volts and calculating  $\beta$ , we can obtain from Figure 51 that at  $f = 1250 \text{ Mc}$ ,  $\beta = 147^\circ/\text{section}$ ; since the distance between sections is about 5.5 mm, then

$$\beta = 147^\circ/\text{sec} \times \frac{1}{5.5 \times 10^{-3} \text{ m/sec}} \times \frac{\pi \text{ radians}}{180^\circ} = 466 \text{ rad/meter}$$

then at 5 mm from the circuit, the field will have decayed to  $\exp[-(466)(5 \times 10^{-3})] = 0.097$ . From this we obtain

$$h = 0.48 \times 10^3 \text{ a-t/m} \times \frac{1 \text{ oersted}}{79.5 \text{ a-t/m}} \times 0.097 = 5.85 \text{ oersted}$$

In our experiment, it was found that one possible location of the ferrite would be at  $y = 5.3 \text{ mm}$  from the surface. Now considering the more pessimistic of the above two calculations, the one that yields the largest RF field, we modify the result by a factor of

$$\frac{\exp[-(466)(5.3 \times 10^{-3})]}{\exp[-(466)(5.0 \times 10^{-3})]} = \frac{0.084}{0.089}$$

then

$$\left[ h_y \right]_{5.3 \text{ mm}} = 5.1 \text{ oersted}$$

Note furthermore that this calculation was made on the assumption of maximum field present in the interaction space, although the field varies cosinusoidally in the space between the coupler row and the supporting flange. Therefore in the region of interest,  $h_{RF}$  is probably less than 5.1 oersted.

From experiments described in the literature (Ref. 15), in particular Table II of the reference,  $\Delta H_k$  is of the order of 0.2 oersted for practically all ferrites (ranging from magnesium ferrites to nickel ferrites to garnets - polycrystalline).

If in relation (1) (Section 6.5) we were to assume  $h(\text{critical}) = 4 \text{ oersted}$  and  $F = 1$ , it would require

- 
15. J. Carter, S. Dixon, and I. Reingold, "Dependence of the Resonance Linewidth of Microwave Ferromagnetic Materials on Incident RF Power," Trans. Inst. Radio Engrs., PG/TT, Vol. MTT-9, No. 2, pp 195-197 March 1961

$$\frac{4\pi M_s}{\Delta H} = \frac{F\Delta H_K}{h(\text{critical})} = \frac{0.2}{4} = 0.05$$

This value would be utterly unusable since in the experiments conducted with AN50MW ferrite samples

$$\frac{4\pi M_s}{\Delta H} = 1.55 = \chi'$$

was felt to be too low! Therefore, we must choose a proper geometry to avoid the first order non-linear effect.

#### 6.5.2 Threshold of Second Order Effect and Ferrite Behavior beyond Threshold

According to Suhl, beyond the critical  $h_{RF}$  field, the susceptibility decreases linearly with  $1/h$  so that even if a material is chosen to operate in a region corresponding to  $h(\text{critical})$ , where  $h(\text{critical})$  is determined by  $\Delta H_K$ ,  $\Delta H$  and  $4\pi M_s$ , the deterioration of  $\chi'$  is slow enough to warrant the use of the material. From the literature (Ref. 16), it is seen that the behavior of ferrite in the vicinity of the threshold critical field is as shown in Figure 67.

#### 6.5.3 Effect of Substitutions on the Value of $h(\text{critical})$ in Yttrium Garnets

It appears (Ref. 17) that Holmium Substitutions greatly enhance the ability of yttrium garnets to absorb high  $h_{RF}$  fields - a 1% Holmium for yttrium moves the threshold from  $h = 1/0.35$  to  $h = 1/0.15$ .

16. Ibid, Schlömann, et al, (In particular Figures 3 and 5)
17. J. J. Green and E. Schlömann, "High Power Ferromagnetic Resonance at X-band in Polycrystalline Garnets and Ferrites," Trans. Inst. Radio Engng., PGMT, Vol. MTT-8, No. 1, January 1960, pp 100-103 (Figure 2)

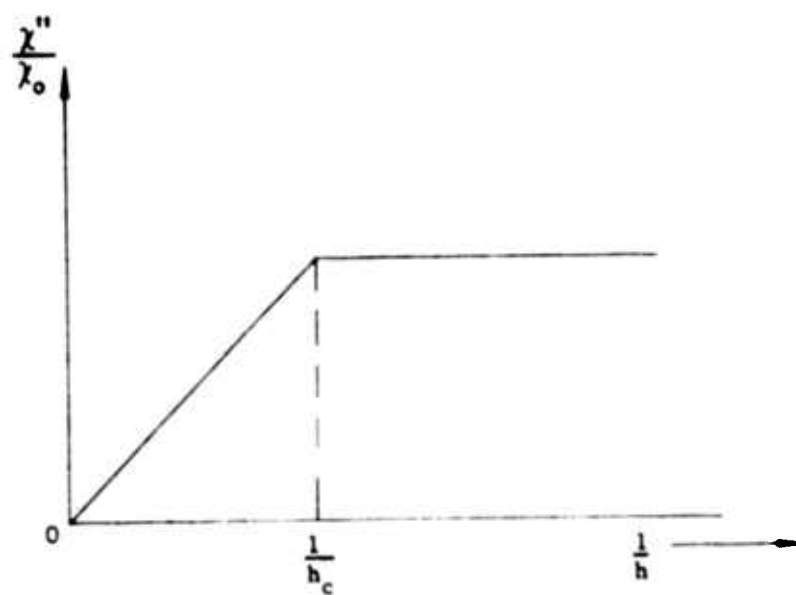


FIGURE 67 DESCRIPTION OF SECOND ORDER NON-LINEAR EFFECT:  
NORMALIZED SUSCEPTIBILITY VERSUS INVERSE OF  
 $h_{RF}$  FIELD

#### 6.5.4 Critical Field for Nickel Ferrite Aluminate

For a material having  $4\pi M_s = 475$ ,  $\gamma = 2.1$ ,  $\Delta H = 290$  oersted,  $h(\text{critical}) = 15$  oersted (Ref. 18). Since the properties of this ferrite closely resemble those we require, we should have no difficulty operating at 5 oersted.

#### 6.5.5 Critical Field for Yttrium-Gadolinium Garnet

Reference 18 also shows  $h(\text{critical}) = 10$  oersted for material with  $4\pi M_s = 710$ ,  $\Delta H = 200$ . From another source (Ref. 19) we see that for an Yttrium Garnet used in experiments,  $\Delta H_k = 0.3$  oersted. The relation used for  $h(\text{critical})$  in this case is

$$h(\text{critical}) = 2M_s \sqrt{\frac{\Delta H_k}{4\pi M_s}}$$

Since our requirements are  $\Delta H = 100$  oersted,  $4\pi M_s = 700$  gauss, then  $h(\text{critical}) = 6$  oersted.

Thus it appears that all the ferrite materials under consideration seem to obey the 5 oersted power requirement.

#### 6.6 Determining the Proper Ferrite for our Application

For our application, a ferrite should satisfy the following criteria

- (1) Sufficient linewidth,  $\Delta H$  for 10% bandwidth; this requires a  $\Delta H \geq 100$  oersted (under operating conditions; note that  $\Delta H$  is temperature dependent).

---

18. Ibid, Schlömann, et al

19. Ibid, Carter, et al



(2)  $4\pi M_s$  requirements

(a) The ratio  $4\pi M_s / \Delta H$  must be high for high attenuation since  $\alpha \text{ db} \sim 4\pi M_s / \Delta H$ . This means that for  $\Delta H$  minimum fixed by bandwidth and temperature dependence, we need  $4\pi M_s$  as high as possible.

(b-1) Avoidance of first order non-linear effect requires a low  $4\pi M_s$

(-2) The disappearance of low field loss at sufficiently high dc magnetic fields also requires a low  $4\pi M_s$

} These conditions are a function of the geometry of the ferrite

(c) The second order non-linear effect requires  $\Delta H / 4\pi M_s$  high. Therefore, for a fixed  $\Delta H$ ,  $4\pi M_s$  is to be as low as possible.

(d) Requirements for temperature independent  $4\pi M_s$  - if  $4\pi M_s$  is variable, then the resonant frequency will also be variable

i. yttrium-iron garnet ferrites can be temperature stabilized by gadolinium substitutions. These elements do not displace the iron ions from their lattice and therefore do not affect the Curie temperature

ii. nickel ferrites usually have such high Curie temperatures (typically above  $400^\circ\text{C}$ ) that over the temperature range of interest - say from room temperature to  $100^\circ\text{C}$  - the  $4\pi M_s$  value is relatively constant with  $2\%$  typically.

Table I summarizes the properties of ferrite materials which seem best suited for our requirements.

## 6.7 The Linear Version of the SFD-209 Circuit

To obtain more detailed measurements on the properties of various ferrites and ferrite geometries, we have decided to construct a linear version of the SFD-209 circuit. The reasons for use of a linear geometry instead of a circular geometry are as follows.

TABLE I  
PROPERTIES OF FERRITE MATERIALS WHICH SEEM BEST SUITED FOR OUR REQUIREMENTS

Material	$h_c$ oersted	$4\pi M_s$ gauss		$k_{eff}$	$\Delta H$ oersted		$\frac{4\pi M_s}{\Delta H}$ Rm Temp	$\left[\frac{4\pi M_s}{\Delta H}\right]_{material}$		$\frac{\epsilon}{\epsilon_0}$	Tan $\delta$	$T_{Curie}^o$
		Room Temp	100°C		Room Temp	100°C		at room temp	AN50MW			
TT 2-116	7.6	1400	1320	2.2	200	100	7	4.55	12.5	0.001	425	
TTG 1005		700	685*	2.04	190	100*	3.68	2.38	16	0.0005	280	
MCL 1118R		800			150		5.35	3.45	13.5	0.003	250	
Sp D80A2-4		750		2.06	225		3.33	2.15			280	
AN50MW		350		1.5	225		1.55	1			280	

\* Correspond to 120°C

$h_c$  is the maximum  $h_{PF}$  field allowed in the microwave cavity at the location of the ferrite before the second order non-linear effect sets in

$\epsilon/\epsilon_0$  is the dielectric ratio with respect to free space

TT - Trans Tech

MCL - Microwave Chemicals Lab

Sp - Sperry

AN50 - Kearfott

### 6.7.1 Reasons for Linear Circuit

(1) Need for accurate but variable spacing of ferrite from circuit - The ferrite must not be too near the surface of the circuit due to the presence of a strong backward wave component, nor can it be too far; if this were to happen, the field would have decayed so much that the ferrite would be ineffective.

Since the field variation in the radial direction is exponential (as  $e^{-\beta y}$ ), it is imperative that we have full control over the radial positioning to understand the behavior of the circuit.

By using ferrite rings

- (a) it is difficult to keep them concentric with the structure
- (b) every new radial excursion requires a new ring since we need effectively a new ID of ferrite.

This difficulty can be circumvented by the use of a linear version of the SFD-209 structure in which a vertical displacement will correspond to a radial displacement in the former structure. Note that the behavior of the two structures (linear versus cylindrical) will be practically the same from an electrical point of view since a linear approximation holds quite well for the cylindrical structure.

(2) Difficulty in supporting the ferrite rings - The requirement of no introduction of mismatches into the structure led to the use of polyfoam which is not very rigid. As a result, considerable difficulty was encountered in the attempt in positioning the ferrite at will with respect to the structure. In the case of a linear structure, the positioning can be controlled beyond the extent of the structure so that a metallic support can be used.

(3) Cost - Circular arcs are very costly and difficult to machine. By contrast rectangular slabs are relatively inexpensive so that a great deal of experimental flexibility can be achieved with them.

### 6.7.2 Provisions for High Power Test

In order to investigate the behavior of the ferrite under relatively high power conditions, without evacuation of the air surrounding the structure, we shall pressurize the circuit with  $\text{SF}_6$  in order to avoid breakdown. Let  $P = 100 \text{ kw}$ ,  $K = V_p^2/2P$  or

$$V_p = \sqrt{2PK} = (2)(10^5)(100) = 4.5 \text{ kv}$$

For an intercoupler spacing of 25 mils,  $E_p = V_p/25 = 4500/25 = 180$  volts/mil. Breakdown can easily be avoided by use of  $\text{SF}_6$ .

Concurrently with the cold test experiments on the linear circuit we shall perform tests on a cylindrical structure of the SFD-209 in order to solve the several technological problems still present - removal of heat from the ferrite, coexpansion of ceramic and adjacent wall, proper seal from ferrite to tube.

## 7.0 STUDY OF THE ECONOMICS INVOLVED IN VARIOUS ARRAY CONFIGURATIONS

(Submitted in satisfaction of subparagraph 3 of Item 3A of Contract)

A suggested arrangement for a phased array radar in which several array channels are operated from each output tube is shown in Figure 68. The output from each tube is divided in a power splitting network and then fed through high power phase shifters to the array element antennas. This arrangement divides the number of tubes required by a factor equal to the number of elements fed by a single tube. It makes the component problem more difficult because power splitters and phase shifters, which are located at low power levels in a one tube per channel arrangement, must be moved to the output lines and thus operate at high power levels. The question to be considered is the relative cost per channel of a single channel per tube versus multiple channels per tube.

The first step in this investigation was to consider the high power phase shifter problem. It appears that phase shifters operating at 100 kw or more and providing fast switching times are well beyond the state of the art. High power phase shifters now in existence are relatively slow operating devices capable of being modulated only at low audio frequencies. To extend present high power phase shifter techniques to fast operation might involve the expenditure of more power to operate the phase shifters than is required to operate the transmitter tubes. The present state of the art in fast switching and phase shifting devices limits them to about 5 kw of peak power. It is, however, not out of the question to imagine that higher power versions of these devices will emerge as the art progresses and that units capable of operating at 100 kw or above will eventually become available. For the purposes of this discussion it is assumed that they will be available. Since the cost of these "future components" is not known, the studies will not be complete but they will at least give a rough feel for the factors and the orders of magnitude involved.

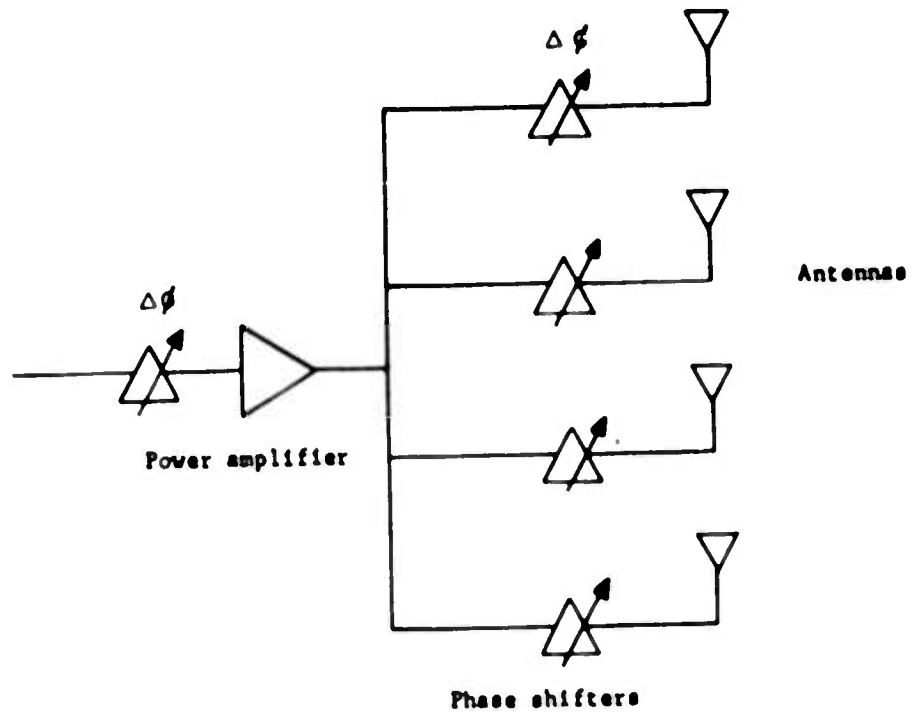


**FIGURE 68** BLOCK DIAGRAM OF AN ARRAY ARRANGEMENT IN WHICH SEVERAL ANTENNAS ARE FED FROM EACH POWER AMPLIFIER

Two L-band arrays have been considered.

- (a) Peak power per element - 100 kw  
Average power per element - 2 kw  
Duty cycle - 0.02  
RF input power - 1 kw peak

In this case the tube used when there is one transmitter tube per array element is the SFD-209

- (b) Peak power per element - 1000 kw  
Average power per element - 2 kw  
Duty cycle - 0.002  
RF input power - 1 kw peak

In this case the configuration used when there is one output transmitter tube per array element is a chain consisting of an SFD-209 and SFD-216 in tandem.

In making the cost estimates, it is assumed that tubes are used whose development cost has been separately funded to the point where a small run of final design tubes has been produced. These development costs are not included in the tube costs. It has been further assumed that when there is more than one antenna element per tube, the requirement on half wave-length spacing of the tubes is lifted. Also, it is assumed that the available input power remains at 1 kw throughout and that the gain is increased as peak power is increased - by adding extra stages where necessary. Finally, operation from a dc voltage with control electrode pulsing is assumed to be feasible up to about 50 kv operating voltage at L-band. Above 50 kv full anode pulsing would be required.

Table II shows the results of the cost study. Included in the table is an estimate of cost per tube chain and cost per antenna element for different numbers of antenna elements per tube. The costs are rough estimates, especially for the higher power tubes. These costs have been obtained by comparing the tubes required with existing tubes with a known price history. The costs in large quantities represent what is felt would be obtained with quantity production techniques now used in the tube industry. Application of new automation techniques may lower the cost further in quantities of 100,000 or more but only if a decision is

TABLE II  
ESTIMATED TUBE COST FOR VARIOUS L BAND ARRAY CONFIGURATIONS

A) 100 kw per antenna element - 0.02 duty - 1 kw input - 100,000 antenna elements

(1) Antenna Elements per Tube	(2) Peak Power Output per Tube Chain	(3) Average Power Output per Tube Chain	(4) Chain Config- uration	(5) Operating Voltage	(6) Quantity of Tubes	(7) Estimated Cost per Chain of Tubes indicated in Column 4	(8) Estimated Tube Cost per Antenna Element
1	100 kw	2 kw	One Tube	8.5 kv	100,000	\$ 250	\$ 250
10	1 Mw	20 kw	2 Tube Chain	25 kv	10,000	1300	130
50	5 Mw	100 kw	2 Tube Chain	50 kv	2,000	5000	100
250	25 Mw	500 kw	3 Tube Chain	100 kv	400	28000	112

B) 1 Mw per antenna element - 0.002 duty - 1 kw input - 100,000 antenna elements

(1) Antenna Elements per Tube	(2) Peak Power Output per Tube Chain	(3) Average Power Output per Tube Chain	(4) Chain Config- uration	(5) Operating Voltage	(6) Quantity of Tubes	(7) Estimated Cost per Chain of Tubes indicated in Column 4	(8) Estimated Tube Cost per Antenna Element
1	1 Mw	2 kw	2 Tube Chain	25 kv	100,000	\$ 550	\$ 550
10	10 Mw	20 kw	2 Tube Chain	70 kv	10,000	2500	250
50	50 Mw	100 kw	3 Tube Chain	140 kv	2,000	10000	200
100	100 Mw	200 kw	3 Tube Chain	200 kv	400	20000	200



made at the start to set up an automated facility. Reaching a 100,000 quantity through smaller repeat orders would not gain a lower cost because no individual order could justify setting up the automated facility.

The results of Table II are plotted in Figures 69 and 70. They show a broad minimum in the cost per element at from 10 to 100 elements per tube. The accuracy with which a cost study can be made at this time does not justify a conclusion as to whether the minimum would really be nearer 10 or 100 tubes.

Use of several antenna elements per tube entails a high power divider network and high power phase shifters following the power amplifier whereas with one tube per element, power division and phase shifting may be done at the low power levels existing at the inputs to the final amplifiers. Thus to find the final cost per element of the various configurations, the extra cost of high power components must be taken into account. This is difficult to do at present because some of the components are entirely speculative. Added to the component costs would also be the additional power supply costs incurred as the voltage is increased and the extra costs of adding pulse modulators when the operating voltage exceed 50 kv.

The added component and power supply cost per element would probably have a characteristic similar to that shown in Figure 71. It is zero for one tube per element and jumps to a finite value at two tubes per element. At this point there is a high power phase shifter per antenna element. The added cost per channel would then continue to grow slowly as the complexity of the divider network and power supply grows. The dotted lines in Figures 69 and 70 show the shape the composite curve of tube plus additional component cost per channel might have. The actual values are not intended to be significant. It is even conceivable that the minimum would lie at one tube per antenna element if the component costs are high enough. The conclusion that must be drawn is that further study of high power phase shifters, divider network components and power supply systems is required before it can be determined whether several antenna elements per tube would represent a saving over one

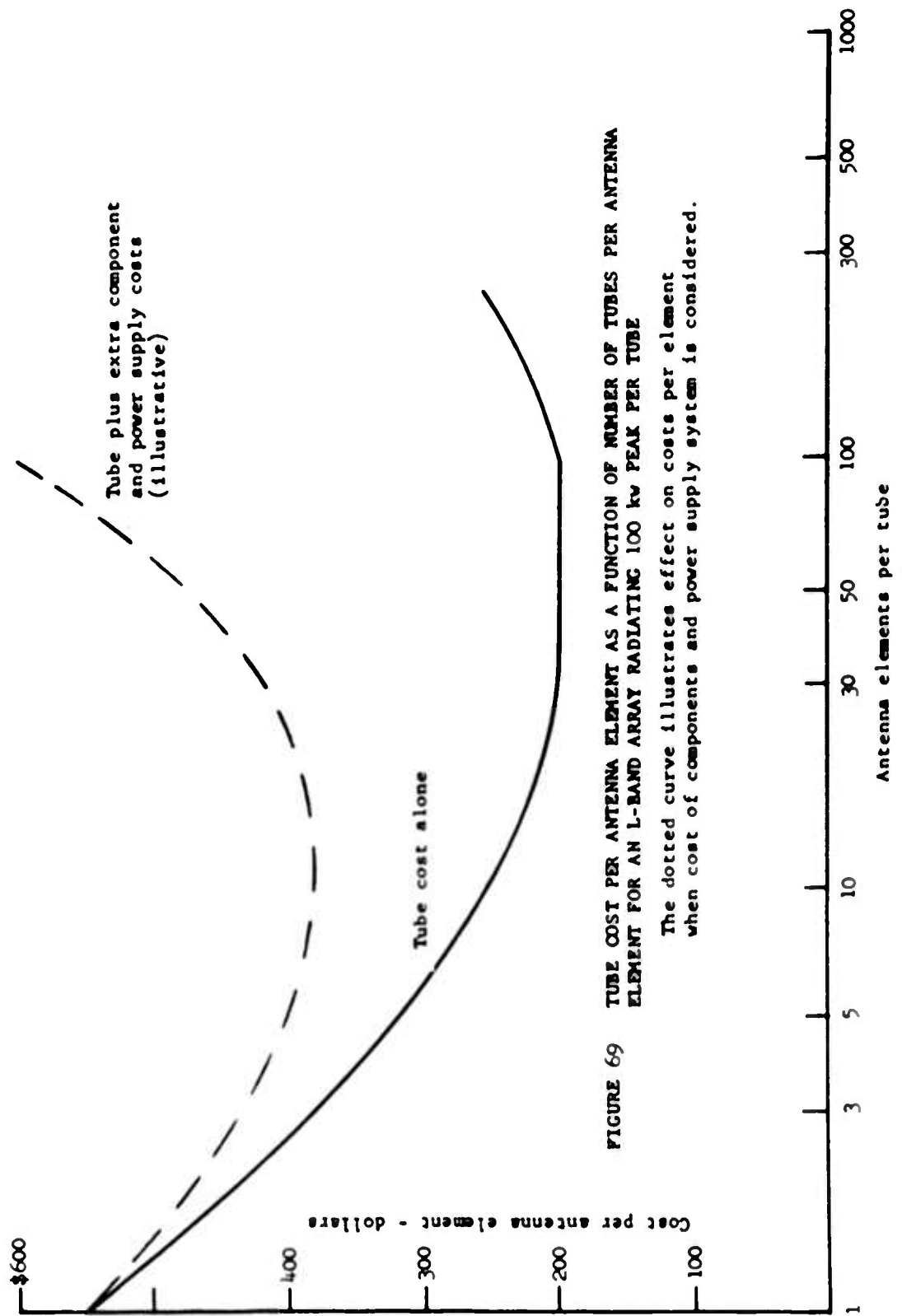


FIGURE 69 TUBE COST PER ANTENNA ELEMENT AS A FUNCTION OF NUMBER OF TUBES PER ANTENNA ELEMENT FOR AN L-BAND ARRAY RADIATING 100 kw PEAK PER TUBE

The dotted curve illustrates effect on costs per element when cost of components and power supply system is considered.

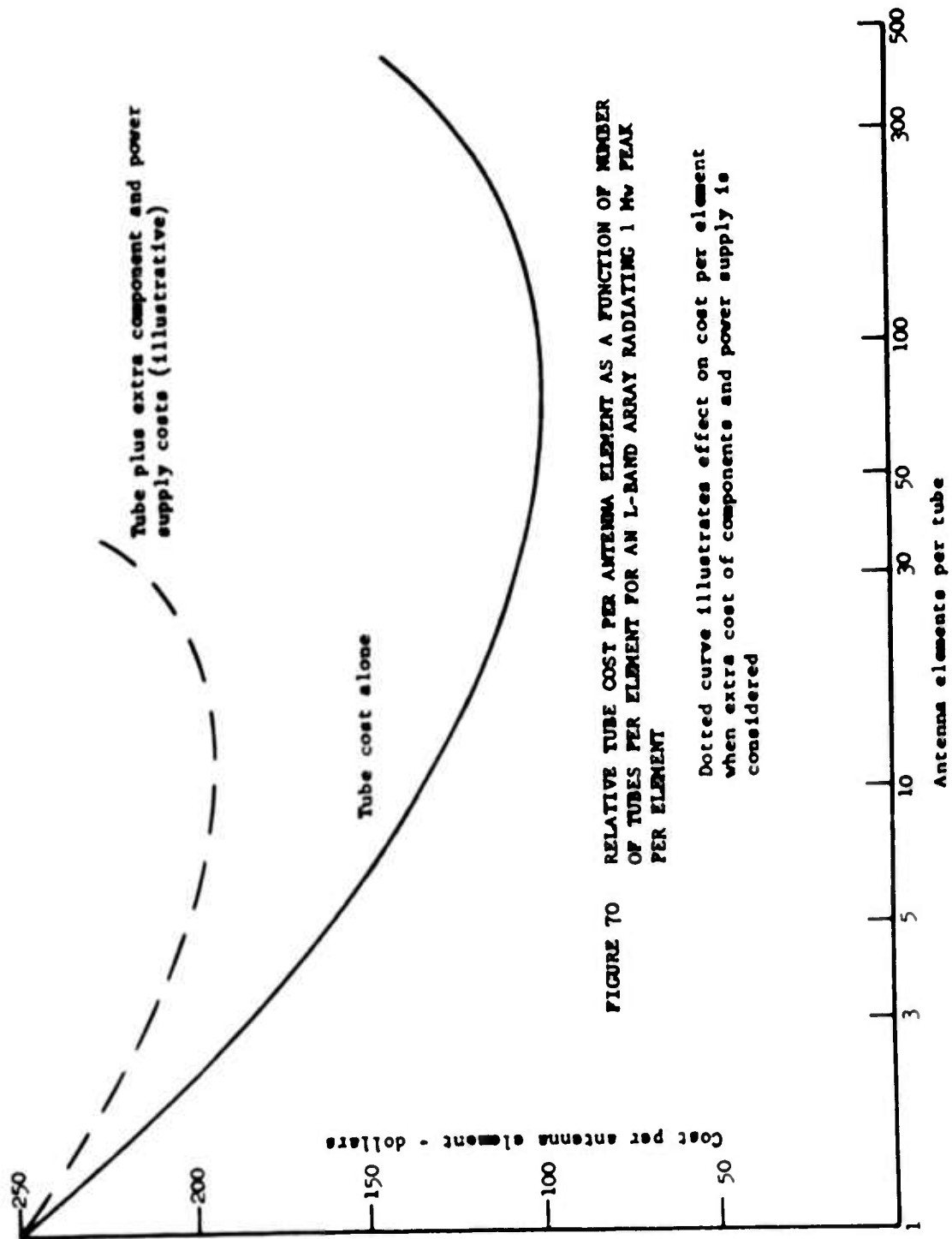


FIGURE 70 RELATIVE TUBE COST PER ANTENNA ELEMENT AS A FUNCTION OF NUMBER OF TUBES PER ELEMENT FOR AN L-BAND ARRAY RADIATING 1 Mw PEAK PER ELEMENT

Dotted curve illustrates effect on cost per element when extra cost of components and power supply is considered

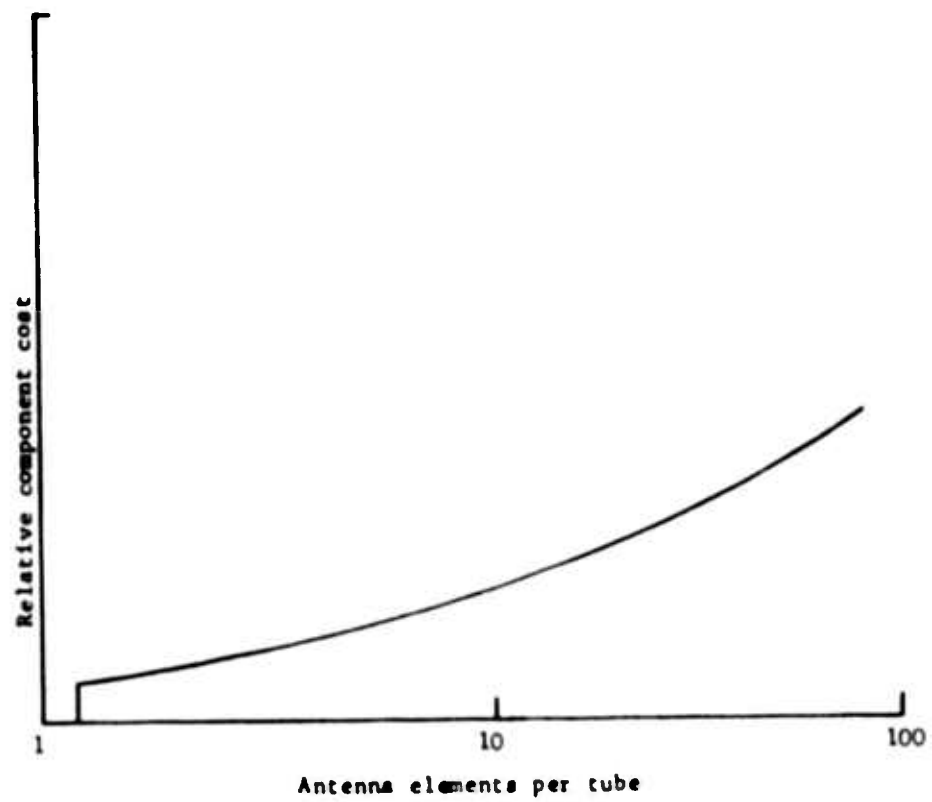


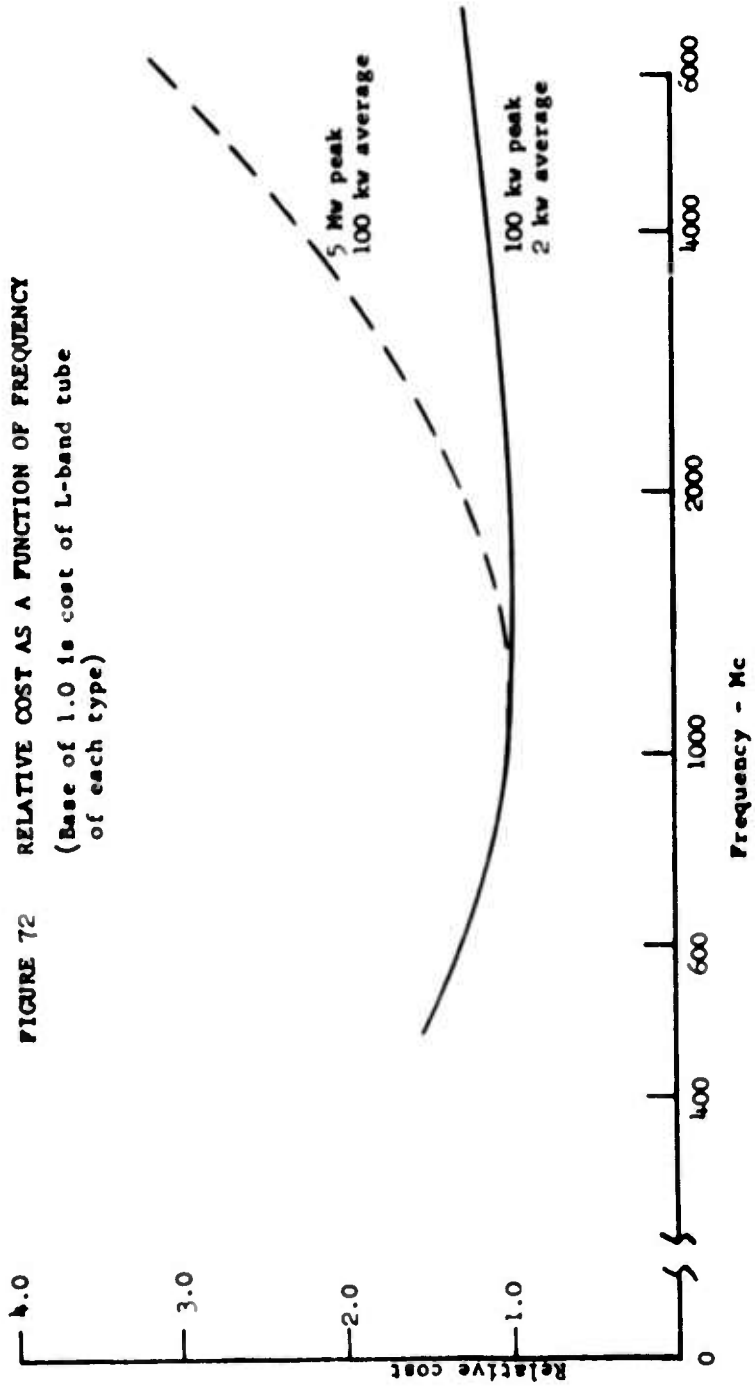
FIGURE 71 RELATIVE INCREASE IN COMPONENT COST AS A RESULT OF POWER DIVISION AND PHASE SHIFTING IN THE HIGH POWER LINE AS A FUNCTION OF THE NUMBER OF ANTENNA ELEMENTS PER TUBE

element per tube. In the near future one element per tube must be the choice because of limitations caused by the state of the art of phase shifters.

Consideration has also been given to how the tube costs would vary as a function of frequency in the range of 600 to 6000 Mc. It is believed that the costs would minimize around L-band. At lower frequencies the increasing size of the tube would increase the cost and at higher frequencies the increasing difficulty of obtaining the average power rating would increase the cost. As examples, Figure 72 shows the estimated relative cost of a 100 kw peak, 2 kw average tube and a 5 Mw peak, 100 kw average tube as functions of frequency. The cost of each tube at L-band is taken as the base of 1.0 in this figure. At the 2 kw average power level, there is a very broad cost minimum and costs would be about the same at L- and S-bands. As the power level is increased the cost minimum becomes sharper and gradually shifts toward lower frequencies. It should be noted that above L-band, it will no longer be possible to stack tubes and magnets on a half wavelength spacing. Thus system costs at S-band for a one tube per antenna element configuration would probably be considerably greater than at L-band.

The major conclusions of this study are

- (1) An array configuration in which several (ten?) antenna elements are fed from a single amplifier chain merits consideration. The feasibility of this configuration depends on progress in the development of fast, high power phase shifters. Final determination of the minimum cost configuration will require an extended study by an organization with system engineering capability.
- (2) At a radiated power of 2 kw average per antenna element, tubes costs would be about the same at L- and S-bands. As the average power per tube (not per antenna element) is increased the minimum becomes sharper and moves toward lower frequencies. At lower average powers the minima is broad and moves toward higher frequencies.



## 8.0 PROGRAM FOR NEXT INTERVAL

During the next six months of this program, we will attempt to:

- (1) evaluate the new B designs and make any necessary design changes
- (2) construct groups of identical tubes of each type
- (3) set up the phase measuring equipment
- (4) characterize the groups of tubes including measurements of output power and phase as functions of input power, operating voltage, magnetic field and frequency
- (5) set up the life testing equipment and begin life testing
- (6) construct the linear version of the SFD-209 circuit and use it to evaluate ferrite attenuator designs; incorporate ferrite attenuator into an operating tube.

**S•F•D laboratories, inc.**

DISTRIBUTION LIST

RADC-TDR-63-492, Contract AF 30(602)-2533

Copies

Rome Air Development Center, Griffiss Air Force Base  
Rome, New York 13442

Attn: RAT	1
Attn: RAALD	1
Attn: RAAPT	1
Attn: RAL	1
Attn: RALC	2
Attn: RALS	2
Attn: RALT	1
Attn: RAO	1
Attn: RAD	1
Attn: RAS	1
Attn: RASG	1
Attn: RALTE, John Schneider	3
Attn: RASH	1
Attn: RASS	1
Attn: RAU	1
Attn: RAUA	1
Attn: RAUE	1
Attn: RAUM	1
Attn: RAUO	1
Attn: RAWC	1
Attn: RAWI	1
Attn: RAY	1

ROAMA, Attn: ROAEP-1, Griffiss Air Force Base, Rome, N. Y. 4

GEEIA, Griffiss Air Force Base, Rome, N. Y. 13442

Attn: ROZMA	1
Attn: ROZMC	1
Attn: ROZME	1
Attn: ROZMN	1
Attn: ROZMCAT	1

RAOL, Griffiss Air Force Base, Rome, N. Y. 13442

Attn: Major Shields	1
Attn: S/L Tanner	2

Air Force Systems Command, Andrews Air Force Base,  
Washington 25, D. C. 20331

Attn: SCLDE	1
Attn: SCFRE	1

Air Force Liaison Office, The RAND Corp, Attn: Technical  
Library, 1700 Main Street, Santa Monica, California

1



***S•F•D laboratories, inc.***

**DISTRIBUTION LIST**

	<u><b>Copies</b></u>
RADC-TDR-63-492, Contract AF 30(602)-2533	
R & T Division, Bolling Air Force Base, Washington 25, D. C. 20332	
Attn: RTH	1
Attn: RTHC (Mr. S. Tepper)	1
AFFTC (FTOOT), Edwards Air Force Base, California 93523	1
APGC (PGAPI), Eglin Air Force Base, Florida 32542	1
ADC (ADMPL-D), Ent Air Force Base, Colorado 80912	1
ORA (RRRT) Holloman Air Force Base, New Mexico 88330	1
USAFAGOS (N-22), Keesler Air Force Base, Mississippi 39534	1
IIq TAC, Langley Air Force Base, Virginia 23365	
Attn: DORQ-S	1
Attn: OA	1
US Strike Command, Attn: STRJ6, MacDill Air Force Base, Fla 33608	1
AUL (3T), Maxwell Air Force Base, Alabama 36112	1
Electronic Systems Division, L. G. Hanscom Field, Bedford, Massachusetts 01731	
Attn: ESAT	2
Attn: ESRDE	1
Attn: ESRL	1
Attn: ESST	1
Attn: ESYT	1
AFMTC, Attn: Tech Lib MU-135, Patrick AFB, Florida 32925	1
ATC (ATTWS-W) Randolph Air Force Base, Texas 78148	3
MATS (MAOCC/C), Scott Air Force Base, Illinois 62224	1
AFSC (CSDASDC), Scott Air Force Base, Illinois 62224	1
White Sands Missile Range, New Mexico 88002	
Attn: Technical Library	1
USAFSS (ECD), San Antonio, Texas	1

**S·F·D laboratories, inc.**

**DISTRIBUTION LIST**

	<u><b>Copies</b></u>
RADC-TDR-63-492, Contract AF 30(602)-2533	
Aeronautical Systems Division, Wright-Patterson Air Force Base, Dayton, Ohio 45433	
Attn: ASNXRR	1
Attn: ASRKSC/Mr. G. L. Larr	1
Attn: ASRNET	1
Institute of Technology Library, MCLI-LIB, Bldg 125, Area "B", Wright-Patterson Air Force Base, Dayton, Ohio 45433	1
Hq USAF, Room 4D-335 Pentagon, Washington 25, D. C.	
Attn: AFRST-EL/CS	1
Attn: AFRSTE	1
Attn: AFRDPC	2
Attn: AFGOA	1
Los Angeles Air Procurement District, Attn: Administrative Contracting Officer (The RAND Corporation), 1700 Main Street, Santa Monica, California	1
USAF Liaison Office (AMSNU-1A), Attn: Lt. Col Lott S. Carter, Hq Army Munitions Command, Dover, N. J.	1
AFSC STLO	
Air Force Unit Post Office, Los Angeles 45, Calif.	1
RTSAL, Attn: Lt. Col. Ardie A. Konkell, Air Force Unit Post Office, Los Angeles 45, Calif.	1
RTSAC, O'Hare International Airport, PO Box 8785, Attn: Capt. Herman M. Geisen, Chicago 66, Ill.	1
RTSAB, Waltham Federal Center, Waltham, Mass.	1
RTSAN, Attn: Mr. Morton M. Pavane, 111 E 16th Street, New York 3, N. Y.	1
RTSAO, Attn: Capt. James A. Street, 119 Ross Avenue, Ottawa, Ontario, Canada	1
RTSAS, Attn: Maj. Herman H. Teifeld, San Francisco, Bay Area, 1069 East Meadow Circle, Palo Alto, Calif.	1
RTSAT, Attn: Maj. John F. Gardner, Air Training Command (ATTRL), Randolph Air Force Base, Texas	1

***S·F·D laboratories, inc.***

**DISTRIBUTION LIST**

RADC-TDR-63-492, Contract AF 30(602)-2533

**Copies**

**AFSC STLO**

RTSIB, Attn: Maj. Reed C. Mulkey, c/o The Boeing Co., Seattle 24, Washington	1
RTSND, Attn: Lt. Col. Chester A. Hazelwood, U. S. Naval Air Development Center, Johnsville, Pa.	1
RTSNM, Attn: Lt. Col. Owen L. Koontz, Naval Missile Center, Point Mugu, Calif.	1
RTSNR, Attn: Lt. Col. Kenneth A. MacAaron, Naval Research Laboratory, Washington 25, D. C.	1
RTSNT, Attn: Lt. Col. Lester E. Clark, Naval Ordnance Test Station, China Lake, Calif.	1
RTSNW, Attn: Lt. Col. A. P. Mercier, c/o Dept of the Navy, Room 3710, Main Navy Building, Washington 25, D. C.	1
RTSRA, Attn: Capt. Alan L. Wright, Aberdeen Proving Ground, Building No. 314, Aberdeen Proving Ground, Pa. 21005	1
RTSRE, Attn: Maj. John C. Burton, Building 1, Edgewood Arsenal, Maryland 21040	1
RTSRF, Attn: Capt. A. J. Ruberg, U. S. Army Electronics R & D Laboratory, Fort Monmouth, New Jersey 07703	1
RTSSA, Attn: Lt. Col. Gilbert G. Morehouse, Ames Research Center (NASA), Moffett Field, Calif.	1
RTSSL, Attn: Maj. Cecil D. Bailey, Langley Research Center (NASA), Langley Air Force Base, Virginia 23365	1
RTSSM, NASA Manned Spacecraft Center, Houston 1, Texas	1
RTSSW, Lewis Research Center (NASA), Attn: Capt. John P. Tinlus, 21000 Brookpark Road, Cleveland 35, Ohio	1
RTSUM, Attn: Maj. Carl R. Wheaton, Massachusetts Institute of Technology, 68 Albany St., Cambridge, Mass	1

**S·F·D laboratories, inc.**

**DISTRIBUTION LIST**

	<u><b>Copies</b></u>
RADC-TDR-63-492, Contract AF 30(602)-2533	
Scientific & Technical Information Facility, Attn: NASA Representative (S-AK/DL), PO Box 5700, Bethesda, Maryland	2
National Aeronautics & Space Administration, Langley Research Center, Attn: Librarian, Langley Station, Hampton, Virginia	3
Federal Aviation Agency, Information Retrieval Branch, Hq-630, Washington 25, D. C.	1
Chief, Army Research Office, Washington 25, D. C.	1
Chief of Research and Development, OCS, Department of the Army, Washington 25, D. C.	1
Commanding Officer, U. S. Army Electronics Research Unit, Attn: 9560 TSU, PO Box 205, Mountain View California	1
Director, Research & Development Army Materiel Command, Attn: Development Division, Temporary Building T, Gravelly Point, Washington 25, D. C.	1
Redstone Scientific Information Center, U. S. Army Missile Command, Redstone Arsenal, Alabama 35808 Attn: Chief, Document Section	2
Commandant, U. S. Army War College (Lib), Carlisle Barracks, Carlisle, Pennsylvania 17013	1
Director, U. S. Army Engineer R & D Labs, Technical Documents Center, Fort Belvoir, Virginia 22060	2
NAFEC Library, Building 3, Atlantic City, New Jersey	1
Chief Signal Officer, Department of the Army, Attn: SIGRD, Washington 25, D. C.	1
U. S. Army Electronics Research and Development Laboratory, Fort Monmouth, New Jersey 07703	
Attn: SELRA/ADT	1
Attn: SR (Dir Radar Div)	1
Attn: PR (Dir Elect Tubes)	1
Attn: PE (Dir EP&M Div)	1
Attn: N (Dir Comm Dept)	1

**S·F·D laboratories, inc.**

DISTRIBUTION LIST

	<u>Copies</u>
RADC-TDR-63-492, Contract AF 30(602)-2533	
U. S. Army Materiel Command, Harry Diamond Laboratories, Attn: AMXDO-TIB, Washington 25, D. C.	1
Commanding General, U. S. Army Electronic Proving Ground, Attn: Tech Library, Fort Huachuca, Arizona 85613	2
Zeus Project Liaison Officer, Bell Telephone Laboratories, Attn: Lt. Col. Lee G. Jones, Whippany, New Jersey	1
Chief, Bureau of Ships, Department of the Navy, Washington 25, D. C.	
Attn: Code 261B	1
Attn: Code 335	1
Attn: Code 670B	1
Attn: Code 680	1
Attn: Code 681A1	2
Attn: Code 454F	1
Director, U. S. Naval Research Laboratory, Washington 25, D. C.	
Attn: Library	1
Attn: Dr. S. T. Smith, Code 5240	1
Attn: R. C. Guthrie, Code 5300	1
Attn: Code 2027	2
U. S. Naval Avionics Facility, Attn: Library, Indianapolis 18, Indiana	1
Chief of Naval Research, Department of the Navy, Attn: 461, Washington 25, D. C.	1
Commander, New York Naval Shipyard, Naval Material Laboratory, Attn: Code 920, Brooklyn 1, New York	1
Commander, Naval Missile Center, Technical Library, Code No. 3022, Point Mugu, California	1
Commanding Officer & Director, U. S. Navy Electronic Lab, Attn: Library, San Diego 52, California 92152	1
Office of Chief of Naval Operations (Op-724), Navy Department, Washington 25, D. C.	1
Office of Naval Research, Chief Scientist, (Code 427), Washington 25, D. C.	1

**S•F•D laboratories, inc.**

DISTRIBUTION LIST

	<u>Copies</u>
RADC-TDR-63-492, Contract AF 30(602)-2533	
Chief, Bureau of Naval Weapons, Department of the Navy, Washington 25, D. C.	
Attn: Technical Library DL1-3	2
Attn: RRRE	1
Attn: RAAV-4423	1
Attn: RREN-3	1
Attn: RNWC	1
Applied Physics Laboratory, Attn: Mr. William Dobbins, Howard County, Maryland	
VIA: Bureau of Naval Weapons Representative, Silver Spring, Maryland	1
Director of Defense Research & Engineering, Pentagon (Room 3E-1065), Washington 25, D. C.	
Attn: Mr. James M. Bridges	1
Attn: Technical Library	1
Central Intelligence Agency, Attn: OCR Mail Room, 2430 E Street, NW, Washington 25, D. C.	1
Director, National Security Agency, Attn: C3/TDL, Fort George G. Meade, Maryland, 20755	1
Defense Intelligence Agency, Attn: DIARD, Washington, D. C. 20301	1
Office of Technical Services (OTS), Department of Commerce, Washington 25, D. C.	5
Advanced Research Projects Agency, Office of the Secretary of Defense, Attn: Lt. Col. W. B. Lindsay, Washington 25, D. C.	2
Advisory Group on Electron Devices, 346 Broadway, 8th Floor, New York 13, New York	3
Scientific Information Officer, British Defense Research Staff, British Embassy, Attn: Mr. F. C. Bruce for CVD, 3100 Massachusetts Avenue, NW, Washington 8, D. C.	3
DDC (TISIA-2), Cameron Station, Alexandria, Va. 22314	20
American Institute of Aeronautics and Astronautics Inc., 750 Third Avenue, New York 17, New York	1

***S·F·D laboratories, inc.***

**DISTRIBUTION LIST**

	<u><b>Copies</b></u>
RADC-TDR-63-492, Contract AF 30(602)-2533	
Aerospace Corporation, Attn: Dr. I. Getting, Los Angeles 45, California	1
Applied Radiation Company, Attn: Mr. N. J. Norris, 2404 North Main Street, Walnut Creek, California	1
Battelle Memorial Institute, Attn: Defender Library, 505 King Avenue, Columbus 1, Ohio	1
Bell Telephone Laboratories, Attn: Dr. J. R. Pierce, Murray Hill Laboratory, Murray Hill, New Jersey	1
Bendix Corporation, Systems Planning Division, Attn: Technical Library, Ann Arbor, Michigan	1
Bendix Corporation Research Laboratories, Attn: Mr. A. G. Peifer, Northwestern Highway, Detroit 35, Mich.	1
The Boeing Company, Airplane Division, Library, Wichita Branch, Wichita 1, Kansas	1
University of California, Berkeley 4, California Attn: Mr. Simmons, Electronics Research Laboratory 427 Cory Hall	1
Attn: Prof. R. M. Saunders, Department of Engineering	1
University of Colorado, Attn: Prof. W. G. Worchester, Electrical Engineering Department, Boulder, Colorado	1
Columbia University, Radiation Laboratory, 538 West 120th Street, New York 27, New York	1
Cornell Aeronautical Laboratory, Attn: Mr. R. C. Beitz, 4455 Genesee Street, Buffalo 21, New York	1
Cornell University, Attn: Dr. G. C. Dalman, Department of Electrical Engineering, Ithaca, New York	1
Institute for Defense Analysis, Attn: Technical Information Office, Research and Engineering Support Division, 1825 Connecticut Ave., NW, Washington 9, D. C.	1
Eitel-McCullough, Inc., San Bruno, California Attn: Technical Library	1
Attn: Dr. B. Arfin	1
Attn: Dr. D. Preist	1

***S·F·D laboratories, inc.***

DISTRIBUTION LIST

	<u>Copies</u>
RADC-TDR-63-492, Contract AF 30(602)-2533	
Field Emission Corporation, Attn: Dr. F. Charbonnier, McMinnville, Oregon	1
University of Florida, Electrical Engineering Department, Gainesville, Florida	1
General Electric Company, Attn: Dr. E. D. McArthur, Power Tube Department, 1 River Road, Schenectady, New York	1
General Electric Company, 601 California Avenue, Palo Alto, California	
Attn: Mr. A. Ryan	1
Attn: Mr. S. E. Webber	1
Harvard University, Attn: Technical Library, Cruft Laboratory, Cambridge, Massachusetts	1
John Hopkins University, Attn: Technical Librarian, Carlyle Barton Laboratory, Baltimore 18, Maryland	1
Huggins Laboratories, 999 E. Arques Avenue, Sunnyvale, Calif.	1
Hughes Aircraft Company, Attn: L. M. Field, Microwave Tube Division, Culver City, California	1
University of Illinois, Electrical Engineering Department, Electron Tube Section, Urbana, Illinois	1
ITT Laboratories, 500 Washington Avenue, Nutley 10, N. J.	
Attn: Mr. A. K. Wing	1
Attn: Mr. T. Marchese	1
Kane Engineering Laboratories, Attn: Mr. J. F. Kane, 845 Commercial Street, Palo Alto, California	1
Lincoln Laboratory, P. O. Box 73, Lexington 73, Massachusetts	
Attn: Dr. G. Guernsey	1
Attn: Mr. R. Butman	1
Litton Industries, 690 Industrial Road, San Carlos, California	
Attn: Mr. W. Watson	1
Attn: Dr. J. Hull	1
Attn: Dr. N. Moore	1



***S•F•D laboratories, inc.***

**DISTRIBUTION LIST**

	<u>Copies</u>
RADC-TDR-63-492, Contract AF 30(602)-2533	
Massachusetts Institute of Technology, Research Laboratory of Electronics, Attn: Documents Library, Cambridge 39, Massachusetts	1
University of Michigan, Attn: Dr. Joseph E. Rowe, Electron Physics Laboratory, Ann Arbor, Michigan	1
Microwave Associates, Burlington, Massachusetts Attn: Dr. P. Chorney	1
Attn: Dr. M. Allen	1
Microwave Electronics, Attn: Dr. S. F. Kaisel, 4061 Transport Street, Palo Alto, California	1
University of Minnesota, Attn: Dr. W. G. Shepherd, Electrical Engineering Department, Minneapolis, Minnesota	1
The MITRE Corporation, Bedford, Massachusetts Attn: Dr. R. F. Naka, Building 2A-251	1
Attn: Joan E. McNaught, Supervisor Library	1
Phillips Research Laboratories, Attn: Dr. G. Espersen, Irvington, New York	1
Physical Electronics Laboratory, Attn: Dr. R. Craig, 2493 Pulgas Avenue, Palo Alto, California	1
Polytechnic Institute of Brooklyn, Attn: Documents Library, Brooklyn, New York	1
Radio Corporation of America, Electron Tube Division Attn: Mr. Hans Jenny, 415 South Fifth Street, Harrison, N. J.	1
Radio Corporation of America, Electron Tube Division, Attn: Mr. R. Raimonde, Lancaster, Pennsylvania	1
Radio Corporation of America Laboratories, Princeton, N. J. Attn: Dr. W. M. Webster	1
Attn: Mr. B. Hershenov	1
Raytheon Company, Spencer Laboratory, Burlington, Massachusetts Attn: Mr. J. Line	1
Attn: Mr. W. Teich	1
Attn: Mr. W. C. Brown	1

**S•F•D laboratories, inc.**

**DISTRIBUTION LIST**

	<u><b>Copies</b></u>
RADC-TDR-63-492, Contract AF 30(602)-2533	
Space Technology Laboratories, Attn: Dr. I. Kaufman, Canoga Park, California	1
Sperry Gyroscope Company, Great Neck, New York	
Attn: J. E. McLinden G38	1
Attn: Mr. T. Sage	1
Sperry Rand Corporation, Electron Tube Division, Gainesville, Florida	
Attn: Dr. A. D. Sutherland	1
Attn: Mr. D. Bergman	1
Stanford University, Stanford, California	
Attn: Dr. A. E. Siegman, Electronics Laboratory	1
Attn: Dr. M. Chodorow, Microwave Laboratory	1
Attn: Microwave Librarian, Microwave Laboratory	1
Sylvania Electric Products, Physics Laboratory, Bayside, N. Y.	1
Sylvania Electric Products, 500 Evelyn Avenue, Mountain View, California	
Attn: Dr. R. Hutter	1
Attn: Dr. J. Needie	1
Varian Associates, Gil Hansen Way, Palo Alto, California	
Attn: Dr. T. Moreno	1
Attn: Dr. A. Staprans	1
Attn: Dr. E. W. Herold	1
University of Washington, Attn: Mr. A. E. Harrison, Electrical Engineering Department, Seattle 5, Washington	1
Watkins-Johnson Company, 3333 Hillview Avenue, Palo Alto, Cal.	
Attn: Dr. R. Peter	1
Attn: Dr. D. A. Watkins	1
Attn: Dr. L. A. Roberts	1
Westinghouse Electric Corporation, Electron Tube Division, Attn: G. R. Kilgore, PO Box 746, Baltimore 2, Maryland	1
Westinghouse Electric Corporation, PO Box 284, Elmira, N. Y.	
Attn: Mr. S. S. King	1
Attn: Mr. G. Klein	1
Yale University, Electrical Engineering Department, 105 Wall Street, New Haven, Connecticut	1

***S·F·D laboratories, inc.***

DISTRIBUTION LIST

	<u>Copies</u>
RADC-TDR-63-492, Contract AF 30(602)-2533	
Northern Electric Company, Ltd., Research and Development Laboratories, PO Box 3511-Station C, Ottawa, Ontario, Canada	1
General Electric Company, Ltd., Attn: Dr. Willshaw, Wembley, England	1
Centre de Physique Electronique et Corpusculaire, Attn: Dr. Doehler, Domaine de Corberville, Orsay (S et O), Paris, France	1
Siemens, Company, Attn: Dr. Katz, Munich, Germany	1
Telefunken Company, Attn: Dr. Dehlike, Ulm, Germany	1
N.E.R.A. A/S Bergen, Attn: Mr. Erling Illokken, Bergen, Norway	1
Norwegian Defense Research Establishment, Attn: Fr Attn: Mr. Finn Lild, Kjeller pr Lillestrom, Norway	1
Chalmers Institute of Technology, Research Laboratory of Electronics, Attn: Dr. O. E. H. Rydbeck, Gibraltargarten S G, Gothenberg, Sweden	1
Royal Institute of Technology, Attn: Dr. Agdur, Stockholm, Sweden	1
Brown Boveri, Attn: Dr. Luedi, Baden, Switzerland	1
CERN, Attn: Mme L. Goldschmidt-Clermont, Service d'Information Scientifique, Geneva 23, Switzerland	1

**UNCLASSIFIED**

**UNCLASSIFIED**